MOLECULAR INSIGHTS INTO THE MECHANISMS OF TRANSPORT AND ENERGY COUPLING IN MEMBRANE TRANSPORT PROTEINS

BY

TAO JIANG

DISSERTATION

Submitted in partial fulfillment of the requirements
for the degree of Doctor of Philosophy in Biophysics and Computational Biology
in the Graduate College of the
University of Illinois at Urbana-Champaign, 2017

Urbana, Illinois

Doctoral Committee:

Professor Emad Tajkhorshid, Chair and Director of Research
Professor Emeritus Robert B. Gennis
Professor Claudio Grosman
Professor Hong Jin

Abstract

Membrane transport proteins are the main gatekeepers controlling the traffic of molecules in and out the cell. The mechanism by which they mediate selective and regulated transport across the membrane is of broad physiological and biophysical relevance. In this dissertation, several critical aspects of the transport process have been studied through molecular dynamics (MD) simulations, including ion binding and its coupling to chemical processes such as H^+ transport, translocation of the transported substrate and cotransported ions, dynamics of the catalytic site, coordinated motions of the remote regions, as well as other molecular events facilitating the transport of the cargo. The first part of the dissertation covers topics on a Cl^-/H^+ transporter from the CLC superfamily, which catalyzes stoichiometrically coupled exchange of Cl^- and H^+ across biological membranes. CLC transporters exchange H^+ for halides and certain polyatomic anions, but exclude cations, F^-, and larger physiological anions, such as PO_4^{3-} and SO_4^{2-}. Despite comparable transport rates of different anions, the H^+ coupling in CLC transporters varies significantly depending on the chemical nature of the transported anion. Although the molecular mechanism of exchange remains unknown, studies on bacterial ClC-ec1 transporter have revealed that Cl^- binding to the central anion-binding site is crucial for the anion-coupled H^+ transport. This study shows that Cl^-, F^-, NO_3^-, and SCN^- display distinct binding coordinations at the central site and are hydrated in different manners. Consistent with the observation of differential bindings, ClC-ec1 exhibits markedly variable ability to support the formation of the transient water wires, which are necessary to support the connection of the two H^+ transfer sites (Glu_{in} and Glu_{ex}), in the presence of different anions. These findings provide structural details of anion binding in ClC-ec1 and reveal a putative atomic-level mechanism for the decoupling of H^+ transport to the transport of anions other than Cl^-. Another important question concerning the functional mechanism of CLC transporters is that no large conformational change have been detected crystallographically, even though transporters usually undergo global conformational change to alternately expose substrate-binding sites to opposite sides of the membrane. The collaborative work here demonstrates the formation of a previously uncharacterized 'outward-facing open' state enrich by high H^+ concentration, which involves global structural changes $\sim$20 Å away from the outer gate. This long distance conformational change highlights the coupled motions as well as the relevance of global structural changes in CLC transport cycle. The second part of the dissertation focus on a phospholipid scramblase which mediates rapid transbilayer redistribution (scrambling) of phospholipids at plasma membrane. This process dissipates lipid asymmetry in response to signals for critical cellular events like apoptosis

that elevate cytoplasmic Ca^{2+} concentration. The work here shows that the hydrophilic aqueduct on the surface of the fungal scramblase nhTMEM16 serves as the path for lipid translocation, and that Ca^{2+} binding plays a key role in determining an open conformation of the path for lipid diffusion. The fully occupied lipid track connects the inner and outer leaflets and forms a proteolipidic pore, which allows ion conduction through the aqueous pathway formed between the protein and lipid headgroups under transmembrane electric potentials. Supporting this mechanism, site-specific mutagenesis experiments show that nhTMEM16 ionic currents are synergistically linked to phospholipid scrambling. To further validate the idea that ions permeate through TMEM16s via the same structural pathway taken by phospholipids, two specific residues in the pore region were pinpointed, which are able to convert TMEM16A Ca^{2+}-activated Cl^- channel (CaCC) into robust scramblase upon point mutations. This novel view of flexible pore structure explains a number of unusual features of the TMEM16 ionic currents, especially the highly variable ionic selectivity and the ability to permeate large ions, which also provides crucial information on the functional dichotomy in TMEM16s.

Acknowledgements

I would like to take this opportunity to thank all that have helped me throughout my PhD life. First, and foremost, I would like to thank my advisor Professor Emad Tajkhorshid for his support and guidance in my PhD study. I have been lucky to have a motivating advisor whose involvement and encouragements have made my experience in graduate school truly rewarding. I would also like to thank Professor Robert Gennis, Professor Claudio Grosman, and Professor Hong Jin for their dedicated service as members of my PhD prelim and dissertation committee. I appreciate the collaboration with Professor Merritt Maduke at Stanford Univeristy and Professor Criss Hartzell at Emory University. I have learned a lot from the stimulating discussions and invaluable feedbacks on the research projects. Many thanks to the entire Tajkhorshid group for making my time in UIUC really enjoyable. A special thank you to my family and friends for their continuous love, unconditional support and enormous patience.

Table of Contents

1 Membrane Transport in Biological Systems[1]

Phospholipid bilayer is the main constituent of the fluid-mosaic plasma membrane. It is only permeable to small and hydrophobic molecules. Continuous and rapid passage of a diverse set of polar molecular species, such as ions, neurotransmitters, nutrients, requires specialized membrane transport proteins [5] that are responsible for catalyzing and regulating exchange of various impermeable substances across the plasma membrane. Membrane transport proteins, including channels and transporters, facilitate the movement of specific substances by distinctive mechanisms. Channel proteins catalyze the passage of substances via facilitated diffusion, during which channels can open simultaneously to both extracellular side and intracellular side of the cellular membrane at the same time, allowing the substrates to pass through the membrane down its concentration gradient at a high rate. No energy input is required for facilitated diffusion via channels.

Transporter proteins catalyze the translocation of substrates against their chemiosmotic gradient by coupling the process to various sources of cellular energy, namely ATP hydrolysis, redox reactions, or photons absorption in *primary* transporters, and electrochemical gradient of the other

[1]The materials presented in this chapter were published in:
1) Giray Enkavi, Jing Li, Pochao Wen, Sundarapandian Thangapandian, Mahmoud Moradi, **Tao Jiang**, Wei Han and Emad Tajkhorshid,"A Microscopic View of the Mechanisms of Active Transport Across the Cellular Membrane".*Annual Reports in Computational Chemistry*, 10:77-125, 2014 [1].
2) Joshua V. Vermaas, Noah Trebesch, Christopher G. Mayne, Sundarapandian Thangapandian, Mrinal Shekhar, Paween Mahinthichaichan, Javier L. Baylon, **Tao Jiang**, Yuhang Wang, Melanie P. Muller, Eric Shinn, Zhiyu Zhao and Emad Tajkhorshid, "Microscopic Characterization of Membrane Transporter Function by in Silico Modeling and Simulation". *Methods in Enzymology*, 578:373-428, 2016 [2].
3) **Tao Jiang**, Wei Han, Merritt Maduke, and Emad Tajkhorshid. Molecular Basis for Differential Anion Binding and Proton Coupling in the Cl^-/H^+ Exchanger ClC-ec1. *Journal of the American Chemical Society*, 138 (9):3066-3075, 2016 [3].
4) Chandra M. Khantwal, Sherwin J. Abraham, Wei Han, **Tao Jiang**, Tanmay S. Chavan, Ricky C. Cheng, Shelley M. Elvington, Corey W. Liu, Irimpan I. Mathews, Richard A. Stein, Hassane S. Mchaourab, Emad Tajkhorshid, Merritt Maduke, "Revealing an outward-facing open conformational state in a CLC Cl^-/H^+ exchange transporter". *eLife*, 5:e11189, 2016 [4].
(5) **Tao Jiang**, Kuai Yu, H. Criss Hartzell, and Emad Tajkhorshid,"Lipids and Ions Traverse the Membrane by the Same Physical Pathway in the nhTMEM16 Scramblase". (submitted).

solute in *secondary* transporters [5]. Depending on the transport directions of the cotransport substrates, secondary transporters are categorized as symporters (same direction) or antiporters (opposite directions). To move the substrates across the membrane, all secondary transporters operate via the *alternating-access mechanism* [6], in which protein alternates between two major states, namely outward-facing state and inward-facing state. In this widely accepted model for membrane transporter functions, the binding site of the transporter cannot be exposed to both sides of the membrane simultaneously at any given time (Fig. 1.1), instead, it changes its accessibility from one side of the membrane to the other upon structural changes in the protein. The alternating-access mechanism ensures that channel-like structures (open to both sides of the membrane simultaneously), which may result in a leak and dissipation of substrate concentration, do not arise. The crystal structures of diverse membrane transporters in several conformations have strongly supported the alternating-access mechanism [7–10].

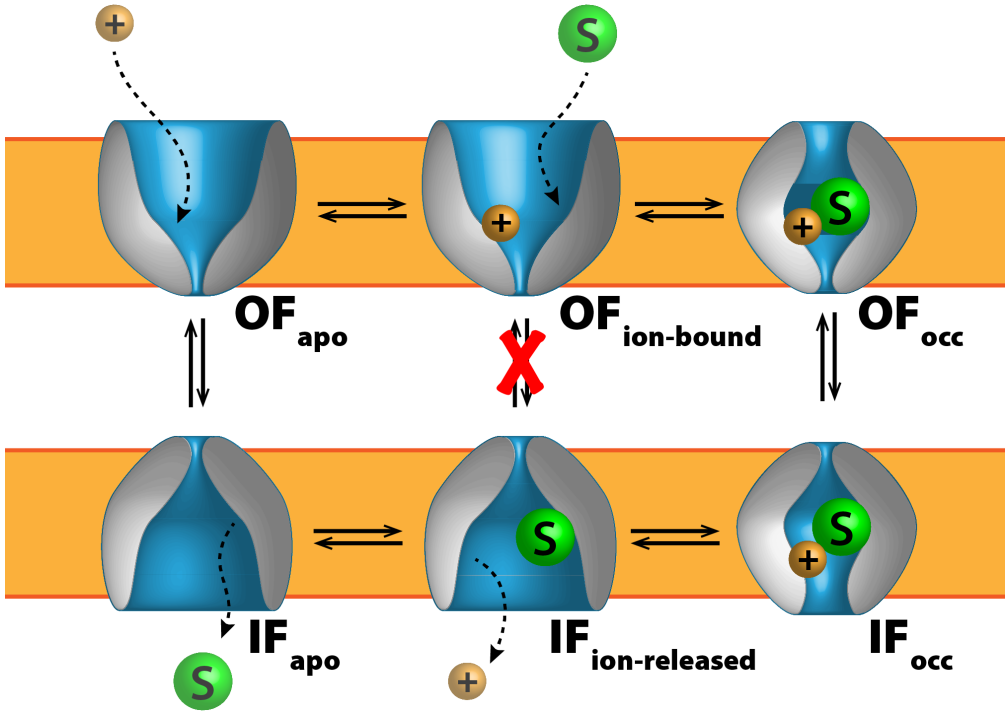

Figure 1.1: An exemplary scheme of the alternating access mechanism adopted by a cation-coupled symporter, where ions and substrate move in tandem. Here, the coupling mechanism only permits conformational transitions when the binding site is either completely vacant or bound with both chemical species, forbidding transitions of partially bound states (red X). Different types of transporters have different coupling mechanisms; however, all share this feature of certain forbidden transitions to regulate substrate transit and to prevent draining membrane potential.

The movement of substrates through transporters is relatively slow compared to that through

channels, because transporters can not open to both sides of the membrane at the same time, and a complex set of molecular processes, such as different levels of protein conformational changes, are tightly coupled with the substrate binding, translocation and releasing. Understanding these processes require fine molecular and atomic details. Given the fundamental roles in biology and the importance as drug targets [11], protein dynamics and functional mechansim of transport proteins (channels and transporters) has generated great interest for mechanistic studies of these proteins.

With the advancement of computational technologies [12,13], and availability of crystal structures across diverse families [8–10], molecular modeling and simulation have proven useful in elucidating the dynamical nature of the mechanism of membrane transport proteins [14]. Computational methods now can describe various molecular phenomena important for membrane protein function and make predictions that can be tested by experiments [15–47].

In my doctoral study, the molecular events behind the function and mechanism of two membrane transport systems were investigated mainly using molecular dynamics (MD) simulations. Each system comes with its own unique challenge in terms of simulation design and application, data analysis, and interpretation of the results. One theme of my doctoral study is to elucidate the anion/proton coupling mechanism, as well as the functionally relevant molecular motions of ClC-ec1, a Cl^-/H^+ antiporter from Chloride Channel (CLC) superfamily. The other theme is to explore the transport mechanism and pathways of phospholipids and ions through nhTMEM16, a phospholipid scramblase from TMEM16 superfamily. Chapter 2 of this dissertation introduces the MD simulation technique and other relevant techniques. Chapter 3-6 cover various mechanistic aspects of the membrane transport proteins.

1.1 Chloride Channel (CLC)

The chloride channel (CLC) proteins [48, 49] constitute a superfamily of membrane transport proteins ubiquitous across species ranging from bacteria to mammals. CLC proteins allow the transport of various anionic species [50–55], such as Cl^-, Br^-, I^-, NO_3^-, and SCN^-, across the cellular membrane. Among those permeating anions, Cl^- is the most important, since it is the most abundant anion in organisms.

CLC proteins are evidently of physiological importance due to their involvement in a broad range of fundamental biological tasks and to their connection to genetically inherited diseases [48,56]. The CLC superfamily was originally thought to include only Cl^- *channels* that catalyze passive diffusion of ions, but it is now well established to include *transporters* that catalyze the transmembrane exchange of Cl^- for H^+ with a 2:1 stoichiometry [57–59]. ClC channels are found in the plasma membrane and participate in maintenance of resting membrane potential, and cell volume regulation. ClC transporters are found in the intracellular membrane, and participate in acidification of intracellular compartment, such as endosomes and lysosomes. Despite the fundamentally different functional properties of the two CLC sub-classes, CLC channels and transporters share the same basic architecture. Therefore, gaining knowledge on CLC transporters will help to understand the overall transport mechanism in CLC superfamily.

1.1.1 Molecular Structural Features

The determination of detailed crystal structures of a bacterial CLC transporter, ClC-ec1, by Roderick Mackinnon's group in 2002, immensely accelerated the structural and functional studies on the CLC family [61]. ClC-ec1, like all canonical CLCs, is a homodimeric protein in which each subunit contains a anion-permeation pathway across the membrane (Fig. 1.2A). The pathway is characterized by an hourglass-shaped selectivity filter (structural element for selective ion conduction), with two aqueous vestibules extending from the extracellular and intracellular sides of the membrane and three anion binding sites [61].

These anion binding sites are formed by residues from four motifs that are highly conserved across the whole CLC family. The four motifs spread out in sequence space, including (ClC-ec1 numbering) GSGIP (106-110), GREGP (146-150), GIFAP (355-359), and Y445 (Fig. 1.2C). These sequences are located at the N-terminal end of helice D, R, F and N, the positive helix dipoles thus create an electrostatically favorable environment for anion binding.

The external anion-binding site (named S_{ext}) can be occupied either by anion or by the deprotonated carboxylate of E148, a conserved residue in the GREGP motif [61]. This residue, which is known as "Glu_{ex}", projects its negatively charged side chain into the pore and obstructs

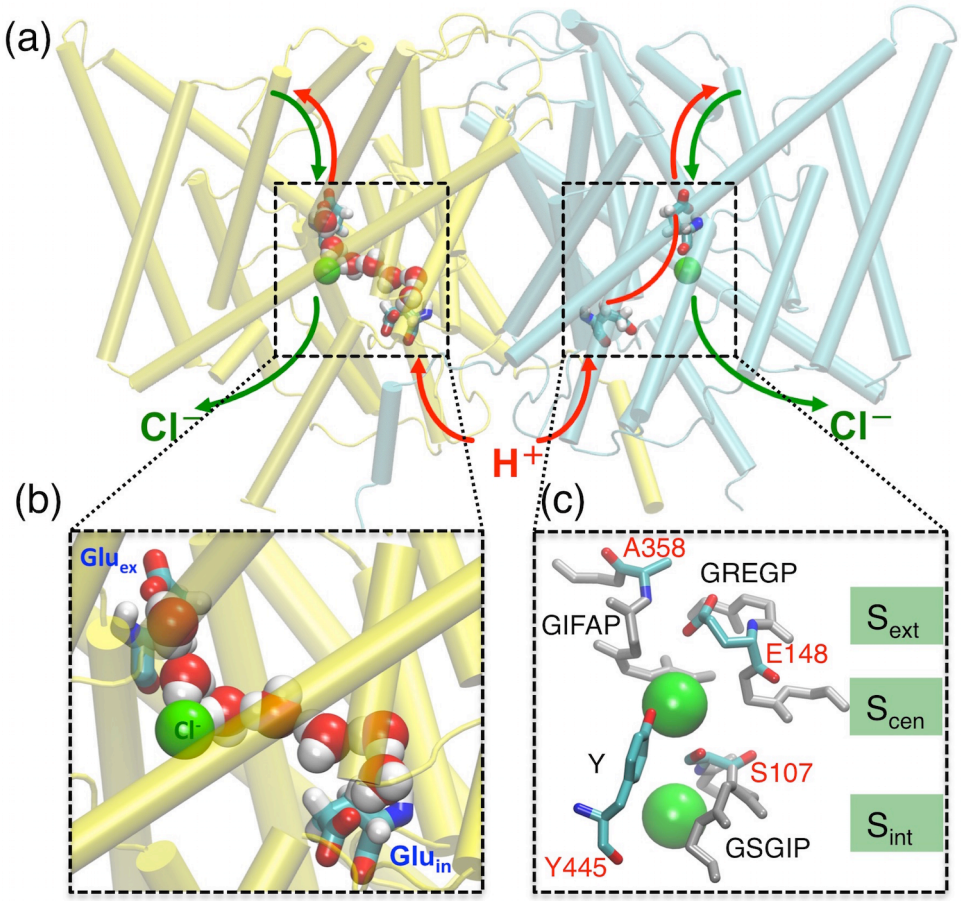

Figure 1.2: Key structural and functional aspects of CLC antiporters. **(a)** Cartoon representation of the ClC-ec1 homodimer (extracellular side on top), with the two identical subunits shown in yellow and cyan, respectively. Approximate Cl^- and H^+ permeation pathways are indicated by green and red arrows, respectively. The H^+ pathway deviates from the Cl^- pathway based on the identification of two key residues, Glu_{ex} and Glu_{in} (see panel (b)), required for H^+ transport. The Cl^- ions bound at S_{cen} are represented as green spheres. **(b)** Representative structure of the most common water wire connecting Glu_{ex} and Glu_{in} observed in MD simulations of Cl^--bound ClC-ec1 [60]. **(c)** The selectivity filter and the three Cl^- binding sites (S_{ext}, S_{cen} and S_{int}) formed by the four highly conserved motifs (GSGIP, GREGP, GIFAP, and Y). In this structure (WT, PDB 1OTS), S_{ext} is occupied by residue E148 (Glu_{ex}), and S_{cen} and S_{int} are occupied by Cl^- ions (green spheres). Residues forming the main constriction points (E148/A358 and S107/Y445) that occlude Cl^- at S_{cen} from the extracellular and intracellular solutions are drawn in color and individually labeled.

the extracellular end of the anion-permeation pathway, as seen in the wild-type crystal structure. When Glu_{ex} is neutralized by protonation or mutation, the side chain swings upwards and S_{ext} becomes occupied by Cl^-, which comes in contact exclusively with backbone nitrogen atoms of motif-residues F357, A358, R147, E148, and G149 [62]. Glu_{ex} has been shown to be crucial not only for the gating mechanism in CLC channels but also for the H^+ coupled Cl^- transport in the bacterial CLC transporters.

The central anion-binding site (S_{cen}) is isolated from the extracellular and intracellular aqueous solutions by the structures containing E148 and S107/Y445, respectively. The ion at S_{cen} is coordinated by backbone nitrogen atoms of I356 and F357, and by the side-chain oxygen atoms of S107 and Y445. Structural and functional studies on ClC-ec1 indicate that S_{cen} has unique characteristics worthy of special attention [55,60,63]. Specifically, experimental and modeling studies have demonstrated a strong connection between Cl^- occupancy of this site and Cl^-/H^+ coupling [55, 60, 63], although the exact molecular mechanism of coupled anion/H^+ exchange remains unresolved.

Lastly, the anion at the internal site (S_{int}) is coordinated by backbone nitrogen atoms of S107 and G108 on one side, and exposed to the intracellular solution on the other side.

1.1.2 Potential H^+ Transfer Pathway

The CLC channels mediate selective Cl^- conductance, while CLC transporters catalyze stoichiometrically coupled exchange of Cl^- and H^+ across the cellular membrane (Fig. 1.2A) [64–67]. CLC transporters exchange two Cl^- ions with one H^+ during each transport cycle [64, 68]. A critical question concerning the CLC Cl^-/H^+ antiporters is how does H^+ being transferred in a highly coupled manner with Cl^- translocation [55, 63, 65]. Information on the H^+ transport pathway and mechanism in CLC transporters is scarce with the exception of the involvement of two highly conserved acidic residues, E148 (Glu_{ex}) and E203 (Glu_{in}) (Fig. 1.2A and B), which have been shown to act as H^+ binding sites on the extracellular and intracellular sides, respectively [69, 70]. However, the central hydrophobic region separating Glu_{ex} and Glu_{in} by about 15 Å raises the concern about the actual mechanism of H^+ transport between these two sites.

H^+ transfer is essential in many biological processes, including membrane transport, in which H^+ is among the most commonly used co-transported species [71–77]. Atomic details of H^+ transfer have proven to be difficult to observe experimentally, rendering computer simulations the main source of knowledge about its detailed mechanism. Among the computational methods that deal with proton transfer are *ab initio* MD [78], empirical valence bond (EVB) [79,80] and reactive force field [81] approaches, which provide realistic descriptions of the process, but at high computational costs. Despite classical MD simulations being unable to model breaking and formation of chemical

bonds involved in proton transfer reaction, its transfer pathways and mechanisms could be inferred by analyzing classical MD simulations for hydrogen-bonded water configurations. This approach is based on the old and well-established Grotthuss mechanism [78], which suggests that protons diffuse through networks formed by water molecules.

Involvement of water wires as potential H^+ transport pathways has been proposed in previous studies on membrane proteins [82–87], most prominently in bacteriorhodopsin [88] and other bioenergetic membrane proteins [89–91], as well as calcium pumps [92]. For studies on CLC transporters, Wang and Voth proposed a transient water-mediated H^+ transport in ClC-ec1 through a pathway connecting E148 and E203, and successfully showed the H^+ propagation along such a pathway using multistate empirical valence bound (MS-EVB) simulations [87]. Ko and Jo reported spontaneous formation of a continuous water network that links E203 with E148 using MD simulations [93]. A similar water network was captured by Cheng and Coalson in their simulations of a eukaryotic CLC transporter homolog CmCLC when E148 was protonated and occupied S_{cen} [94, 95]. In a recent collaborative work from our group, MD simulations showed that water wires can form transiently and repeatedly connecting Glu_{ex} and Glu_{in} across this void (Fig. 1.2B) [60]. The role of these water wires in the H^+ transport mechanism was validated by identifying a residue that is conformationally coupled to water-wire formation and experimentally demonstrating the impact of its mutations. This work also demonstrated the importance of the Cl^- ion bound at the S_{cen} site for stabilizing the water wires, thereby proposing a putative mechanism underlying the coupling of the two ions [60].

Chapter 3 of this dissertation investigated the binding mode and dynamics of various anions transported by CLCs. Through multiple extended MD simulations, the structure and dynamics of ClC-ec1 were examined in the presence of different anionic species, namely, Cl^-, F^-, NO_3^-, and SCN^- bound at S_{cen}. Different anions adopt distinct binding coordinations and hydration patterns, and, more importantly, exhibit differential abilities to support the formation of water wires between the H^+ transfer sites (Glu_{in} and Glu_{ex}). In contrast to the continuous water wires observed in the presence of Cl^-, the wires formed in the presence of F^- or NO_3^- directly incorporate the anions (pseudo-waterwires). This intervention by the anion may reduce the ability of the wire to conduct H^+. Binding of SCN^-, on the other hand, eliminates the water wires altogether. These findings

explain the variable H^+ coupling measured experimentally for these four representative anions, including fully coupled (Cl^-), intermediately coupled (NO_3^-), absolutely uncoupled (SCN^-), as well as impermeant (F^-). These results highlight the importance of anion binding for coupled H^+ transport in ClC-ec1, thus providing deeper mechanistic insight into the function of CLC proteins.

In **Chapter 4** of this dissertation, the local conformational change induced by a single mutation S107P in the S_{cen} binding site of ClC-ec1 was examined. The structural change in the loop containing the mutation affects the binidng of anions at the S_{cen} site, which may underlie the molecular origins of anionic specificity in CLC transporters. Obtaining knowledge on the structural and functional role of S107 is essential to the overall understand of the H^+ coupling mechanism in CLCs.

1.1.3 Global Conformational Change

As secondary active transporters, CLC transporters can use the energy from Cl^- moving down its electrochemical gradient to pump H^+ against its electrochemical gradient, or vice versa. To achieve the stoichiometric exchange of 2 Cl^- for every H^+, CLC transporters must follow the alternating-access mechanism [6] and tightly couple protein conformational change to substrate binding, translocation, and unbinding events. The alternating-access mechanism implies the existence of at least two major conformational states, "outward-facing (OF)" state, in which the external, but not internal, solution is accessible to the bound substrates); and "inward-facing (IF)" state, in which the internal, but not external, solution is accessible (Fig. 1.1). A large number of intermediate states can form during the interconversion between the major states (IF$\leftrightarrow$OF) in each transport cycle. Substrate binding site in these intermediate states can be made occluded to both sides of the membrane (an "occluded" state) by various mechanisms including movements of loops, amino acid side chains, and/or segments of broken helices, while the overall conformational state of the protein can remain IF or OF.

For all other transporters studied to date, including the superfamilies with MFS, LeuT, the conformational changes from outward-facing to occluded to inward-facing have been shown to involve global protein motions, including reorientation of helices or even entire domains. For the

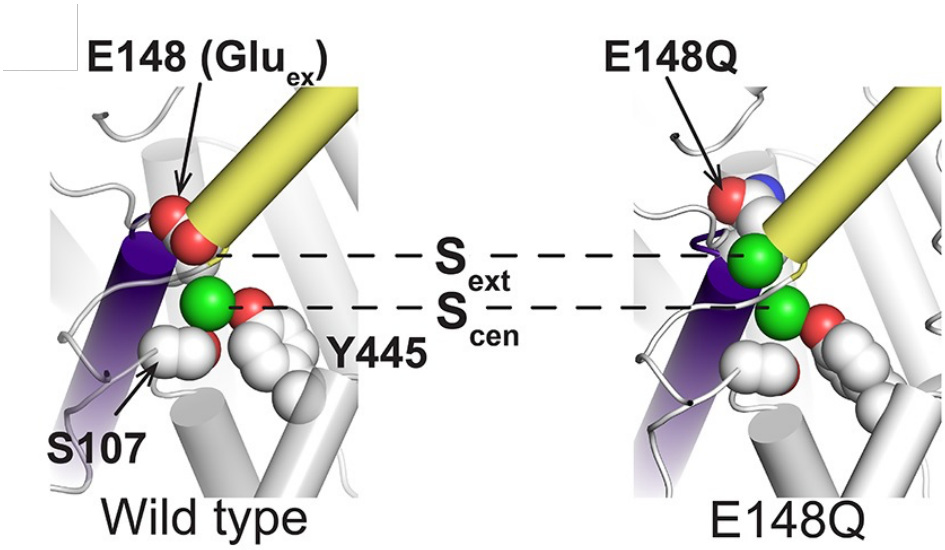

Figure 1.3: Structure comparison of WT (left) and E148Q (right) ClC-ec1 Cl^-/H^+ transporter. The intracellular and extracellular gate residues S107, Y445, and E148 (Glu_{ex}) are highlighted. In the WT ClC-ec1 (pdb: 1OTS), The bound Cl^- (green sphere) at site S_{cen}) is coordinated by the highly conserved Ser and Tyr residues (shown as spacefilled). Glu_{ex} also acts as a "gate" that blocks the Cl^- permeation pathway from the extracellular solution. In the E148Q mutant (pdb: 1OTU), the Gln side chain, mimicking the protonated Glu_{ex}, swings away from the Cl^- permeation pathway and is replaced at S_{ext} with a Cl^- ion. The structure of this mutant is otherwise indistinguishable from the WT structure.

CLC transporters, however, only a single conformation has been detected crystallographically, which is known as the occluded state. Extensive efforts using crystallography have failed to detect any global conformational changes in the transport cycle. Based on the available Xray structures, the side chain rotation of a highly conserved glutamate residue represents the sole differences distinguished in crystallographic studies of CLC transporters [62,96]. This highly conserved residue, Glu_{ex}, is located towards the extracellular side of the anion-permeation pathway, where it physically blocks anions from the extracellular solution. In the structure of a mutant in which Gln is used as a proxy for the protonated Glu_{ex}, the side chain swings upwards and appears to unblock the Cl^--permeation pathway. Thus, the site previously occupied by the glutamate side chain is occupied by an anion (Fig. 1.3). However, in this mutant structure the pathway to the extracellular solution is still very too narrow to accommodate Cl^- or other permeant ions, which suggests that additional conformational changes are required for for external anions to access the external anion-binding site S_{ext}. Given the strong constraining forces in a crystal environment, which often prevent the protein from populating all naturally accessible, functionally relevant conformational states, alternative approaches for detecting CLC conformational change during its function are strongly motivated.

In **Chapter 5** of this dissertation, large scale conformational changes of ClC-ec1 was studied by cross-linking simulations in collaboration with experimental methods (Merritt Maduke, Stanford University). Using NMR, our collaborator detected a H^+-dependent conformational changes near the interface of the homodimer, in which a buried residue Y419 became solvent exposed after increasing the H^+ concentration. To test the functional relevance of this motion, a cysteine cross-link was generated to constrict motion at the interface. Constriction of this motion via the cross-link correlated directly with reduced Cl^- transport. By applying normal mode analysis on the cross-linking MD simulations, we are able to probe functionally relavent motions near the Cl^- permeation pathway that was affected by the long distance conformational changes near dimer interface. The results show that the extracellular vestibule of the anion-permeation pathway was widened at low pH and thus generates a previously uncharacterized "outward-facing open" CLC conformational state. This finding clearly indicates that structural changes beyond the rotation of Glu_{ex} is in volved in the CLC Cl^-/H^+ transport cycle.

1.2 Phospholipid Scramblase Anoctamin/TMEM16

Plasama membranes are cell boundaries that physically separate and protect the cell interior from the extracellular environment. They are constructed of a bilayer structure, where different lipids asymmetrically distributed in the outer and inner leaflets to form distinct lipid compositions of the membrane. Lipid asymmetry is essential to cellular physiology and plays key roles in regulating membrane protein functions [97–103] and determining membrane curvatures [104–108]. Creation and maintenance of lipid asymmetry in normal cells requires the concerted actions of lipid flippases and floppases that actively transport specific lipids in preferred directions at the expense of ATP hydrolysis (Fig. 1.4) [109–114]. When a perturbation of lipid asymmetry is needed for the cell, ATP-independent lipid scramblases are needed to carry out nonspecific and bidirectional transport of lipids in response to the elevation of cytoplasmic Ca^{2+} concentration [115,116]. Lipid scrambling is an ubiquitous cell signaling mechanism for many critical cellular events, including marking the apoptotic cells [117–120] and initiating blood coagulation [115, 121–124]. Since it is energetically unfavorable to translocate the polar headgroup of lipid through the hydrophobic interior of the membrane bilayer, transbilayer movement of lipid by itself is a very slow process. Thus, gaining

knowledge on the physiological process of lipid scrambling is critical for the overall understanding of the regulation of lipid asymmetry.

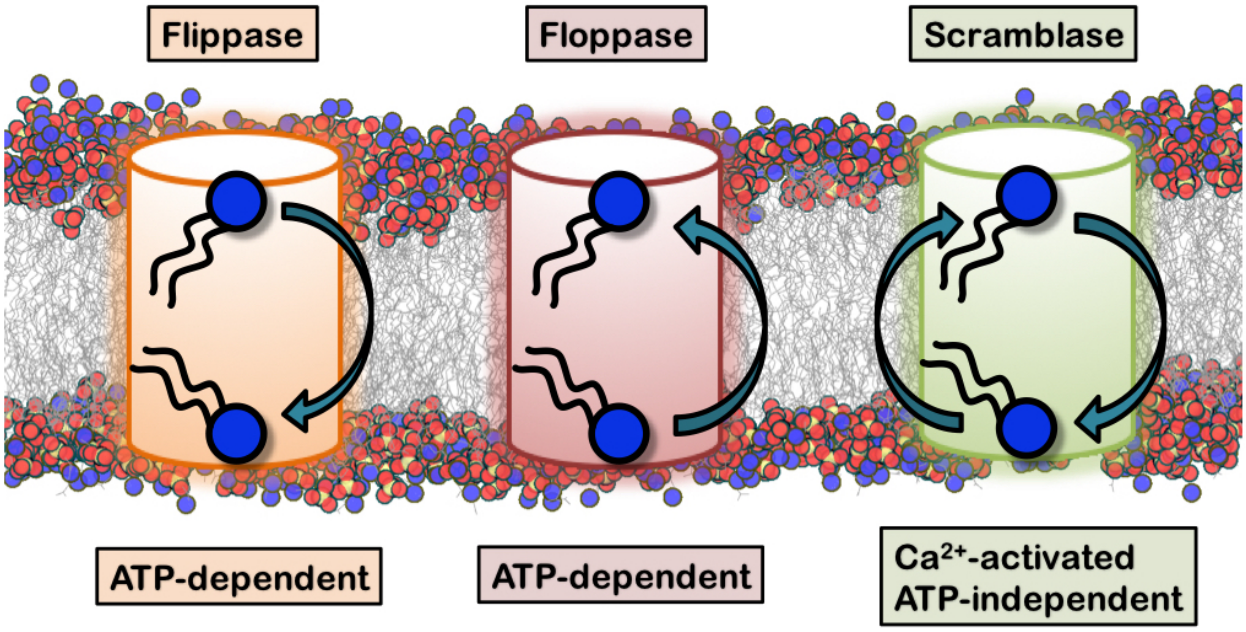

Figure 1.4: Lipid asymmetry is established by lipid flippases and floppase, which use energy from ATP hydrolysis to actively transport lipids in a preferred direction. Scramblases randomize lipids across the membrane bidirectionally and thus degrade membrane lipid asymmetry. The scrambling process is essential for cellcell fusion, blood coagulation, apoptosis, glycosylation, autoimmune diseases and inflammation.

The TMEM16 family constitutes a class of membrane proteins that contribute to remarkably diverse physiological processes, ranging from ion transport to phospholipid scrambling [125]. The first two family members (TMEM16A and B) were functionally characterized as Ca^{2+}-activated Cl^- channels (CACCs) [126–130], while TMEM16F was identified as a Ca^{2+}-activated nonselective cation channel [124], and is essential for the Ca^{2+}-dependent scramblase activity [122, 124]. The roles of the other members remain poorly understood, many of them were suggested to function as scramblases [117]. Despite the broad range of functions, experimental studies on TMEM16 proteins have demonstrated a similar mode of Ca^{2+} activation throughout the family [115, 116]. The high sequence similarities among the homologues suggest a basic structure as well as mechanism of action that is commonly shared by the family members [131–133]. Thus, investigating the mechanistic details of the scramblase and ion channel function, especially the activation by Ca^{2+} ions will not only shed light on the potential scrambling and ion conduction mechanism but also provide a framework for unraveling the functional mechanisms of other TMEM16 members.

1.2.1 Molecular Structural Features

The recently crystallized structure of a TMEM16 family member from fungi *N. haematococca* (nhTMEM16), provides the first insight into the architecture of TMEM16 proteins [134]. nhTMEM16 functions as a Ca^{2+}-activated lipid scramblase, which facilitates the passive bidirectional transport of diverse lipids between the two leaflets of the membrane [134]. The nhTMEM16 protein is organized as a dimer of two identical subunits, each subunit contains ten transmembrane helices. The most intriguing feature of the structure is a hydrophilic aqueduct located on the opposite surface of each subunit from the dimer interface. This aqueduct harbors the highly conserved Ca^{2+}-binding site for two Ca^{2+} ions and is exposed to the lipid bilayer as a potential site of lipid scrambling (Fig. 1.5). Although the static structure of the lipid scramblase gives insight into the potential site of catalysis, there were no lipophilic molecules resolved in the crystal structure. Hence, to characterize the specific features of the protein and identify the relationship between the structural features and the mechanism of functions, detailed atomic information of the dynamic interactions between the scramblase and its lipid environment is needed.

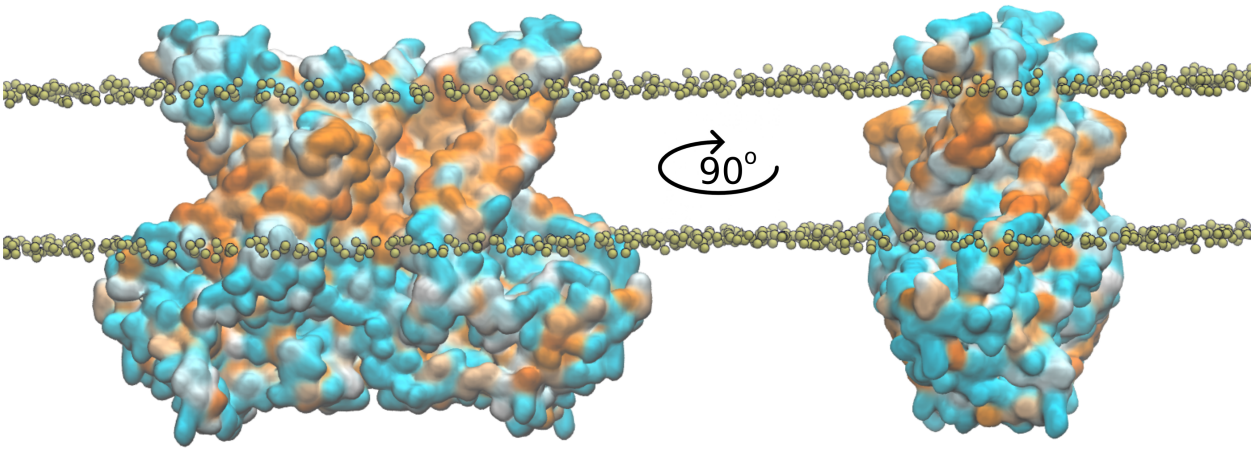

Figure 1.5: Scramblase surface hydrophobicity. Molecular surface representation of nhTMEM16 crystal structure, colored according to the hydrophobicity scale of Kyte and Doolittle (Cyan = hydrophilic (-4.5), Orange = hydrophobic (4.5)), illustrating the hydrophilic surfaces near the entrances of the aqueduct, exposed to the hydrophobic core of the membrane. The initial headgroup region of the lipid bilayer is represented by the phosphorus atoms of the headgroups shown as tan spheres.

1.2.2 Dual Function of nhTMEM16 Scramblase

A recent study on nhTMEM16 indicated that this lipid scramblase also function as a Ca^{2+}-activated nonselective cation channel [135]. Thus raises another major question concerning the TMEM16 proteins - how is the same structure accommodate such a diversity of functions. The crystal structure of nhTMEM16 does not offer an obvious alternative pathway for ion permeation through the bilayer other than the hydrophilic aqueduct exposed to the membrane interior. Atomistic details on the structural and functional properties of nhTMEM16, especially the pathway for lipid translocation as well as ion permeation, will not only provide mechanistic insights into the overal understanding of the scrambling mechanism, but also add critical information on our knowledge of the ion channel function of the TMEM16 members.

Chapter 6 of this dissertation sought to investigate the mechanistic details of three critical aspects involved in the substrate transport processes of nhTMEM16: the pathway that mediates the rapid redistribution of lipid polar headgroups across the hydrophobic core of the membrane, the pathway for ion conduction through the membrane, and the molecular basis of the Ca^{2+}-dependence. In this study, both MD simulations and experimental methods (H. Criss Hartzell, Emory University) have been applied in order to investigate these critical aspects of protein function. By performing extended MD simulations, a membrane-traversing lipid translocation aqueduct was observed on the protein surface, effectively connecting the inner and outer leaflets of the bilayer. Spontaneous binding of lipid headgroups to the aqueduct is observed in the Ca^{2+}-activated system, exhibiting a number of specific residues in the aqueduct that favor lipid headgroup binding. Moreover, by applying external electric field to generate voltage difference across the membrane, the permeation of Na^{+} ions from the extracellular bulk to the intracellular bulk via the same structural path - the fully hydrated aqueduct was observed, which provides the first atomisitc information on the ion permeation pathway of TMEM16. Furthermore, simulation also demonstrated that Ca^{2+} ions play a key role in determining the functional conformation of the lipid aqueduct, which is necessary for full hydration of the aqueduct and smooth diffusion of headgroups along the aqueduct. These findings not only characterize the entire lipid and ion translocation pathway but also uncover the nature of Ca^{2+}-dependence at atomic level, thus add a crucial layer of details into the overal understanding of TMEM16 proteins.

2 Overview of Methods[1]

Simulation with classical molecular dynamics (MD) [136] is a compelling addition to the scientific arsenal, going beyond the resolution and interpretation limitations of conventional experiment to provide models of these systems at arbitrary resolution. Crucially, MD permits atomic events (such as a side chain rotation or the formation of a salt bridge) to be observed on a single molecule level, allowing the effect of specific mutations or binding events to be captured for biological assemblies [137].

The resolution offered by MD is particularly important because transporters are inherently dynamic, which can cause difficulties for experimental observation. While static methods such as X-ray crystallography [138] or cryo-EM [139, 140] are indispensable to determining a 3D structure, they are missing some of the rich details that can only be obtained by exploiting the unparalleled simultaneous spatial and temporal resolution of MD simulation [141, 142]. Instead, ensemble spectroscopy techniques such as NMR [143, 144] or EPR [145] as well as single molecule techniques such as FRET [146] have had the greatest success in probing transporter conformational change. However, due to resolution restrictions on these techniques, computational modeling and MD also have a role to play.

The relationship between simulation and experiment can best be thought of as a symbiotic one [147, 148]. Simulation is impossible without the high-resolution experimentally-derived structures. Likewise, experiment is driven forward by understanding of the interactions present in the

[1]The materials presented in this chapter were published in:
1) Giray Enkavi, Jing Li, Pochao Wen, Sundarapandian Thangapandian, Mahmoud Moradi, **Tao Jiang**, Wei Han and Emad Tajkhorshid,"A Microscopic View of the Mechanisms of Active Transport Across the Cellular Membrane".*Annual Reports in Computational Chemistry*, 10:77-125, 2014 [1].
2) Joshua V. Vermaas, Noah Trebesch, Christopher G. Mayne, Sundarapandian Thangapandian, Mrinal Shekhar, Paween Mahinthichaichan, Javier L. Baylon, **Tao Jiang**, Yuhang Wang, Melanie P. Muller, Eric Shinn, Zhiyu Zhao and Emad Tajkhorshid, "Microscopic Characterization of Membrane Transporter Function by in Silico Modeling and Simulation". *Methods in Enzymology*, 578:373-428, 2016 [2].

system at the nanoscale. Later chapters of this dissertation will describe how the computational techniques were used to probe a system of interest, and the fruitful collaboration with experiment that improve the final scientific result.

2.1 Molecular Dynamics (MD)

Molecular dynamics (MD) is a computational method to investigate the dynamics of molecules based on classical and statistical mechanics [149]. The simulation system is composed of a collection of particles connected with bonds to reflect their chemical properties. The interaction between the particles in classical MD simulations is defined by a predefined potential energy function. The potential energy functions, called "empirical force fields" in this case, are designed to reproduce chemical and thermodynamic properties of the molecules using experimental data and quantum mechanical calculations as a reference. Typical force fields generally include potential energy terms describing bonded (bonds, angles, dihedrals) and non-bonded (van der Waals and electrostatic) interactions:

$$U = U_{bond} + U_{angle} + U_{dihedral} + U_{vdW} + U_{elec}$$

The number of bonded terms is generally smaller and the non-bonded interactions usually form the expensive part of the computation. Electrostatic potential is defined as

$$U_{elec} = k_e \frac{q_i q_j}{r},$$

where k_e is Coulomb's constant, r is the distance between the two atoms with charges, q_i and q_j. The van der Waals interactions are represented by the Lennard Jones potential:

$$V_{vdW} = 4\varepsilon[(\frac{\sigma}{r})^{12} - (\frac{\sigma}{r})^{6}],$$

where ε is the well depth, σ is the distance at which the potential is zero.

The negative gradient of the potential energy, U, with respect to the coordinates, $\vec{r}$, is used to

calculate the force, $\vec{F}$, acting on each atom:

$$\vec{F} = -\vec{\nabla}U.$$

Integration of the Newtonian equations of motion [149, 150] is required to propagate the positions, $\vec{r}$, and the velocities, $\vec{v}$, of atoms in time, t:

$$\vec{F} = m\vec{a}; \quad \vec{a} = \frac{d\vec{v}}{dt}; \quad \vec{v} = \frac{d\vec{r}}{dt},$$

where m is the mass and $\vec{a}$ is the acceleration. Several thermodynamic and dynamic properties of the systems can be assessed from the trajectories generated by MD simulations.

MD simulations require calculation of interactions between each pair of particles in the simulation system, making them highly dependent on developments of algorithms and computer technology for efficient performance [151]. Despite being computationally demanding and therefore limited by the accessible time-scales, MD provides dynamical information at high spatial and temporal resolutions. MD studies have successfully complemented experiments for a wide range of biomolecular systems and phenomena, including membrane transport proteins and their mechanisms [44,46,152]. Continuous algorithmic improvement, availability of faster hardware, better force fields, and enhanced sampling techniques continue to close the gap between simulations and experiments mainly by improving the accessible time scale of MD [153–156].

2.2 Simulation System Preparation

MD simulations require a set of initial coordinates and velocities to start the integration of Newton's equations of motion. While the initial velocities are randomly selected from a Maxwell-Boltzmann distribution, initial coordinates are generally obtained from experiments that provide atomistic resolution, especially in the case of biomolecular simulations. For any level of biomolecular simulation, a correct starting structure is essential to the validity of the results. For simulations discussed in this dissertation, the starting coordinates for a 3D structure were generally retrieved from the Protein Data Bank (PDB) [157–159].

2.2.1 Protein Structure Refinement

Once a starting point was obtained, there are a number of additional technical elements that were checked prior to starting simulation, including the completeness of the structure and protonation. PDB structures from crystallographic data are often missing pieces of the native protein, which were too floppy or dynamic to be well resolved in the crystal lattice. To fill in these gaps, SuperLooper [160] was used to generate candidate models for membrane protein loops, in order to complete the protein structure. The missing atoms such as hydrogens were added using psfgen implemented in VMD [161].

For ionizable residues such as histidine or aspartate, their pKa can shift dramatically depending on their protein environment. To determine the protonation states of the ionizable residues, the pKa of each and every residue was estimated using PROPKA [162, 163]. When combined with the PDB2PQR originally designed for Poisson-Boltzmann electrostatics calculations [164], PROPKA generates an output that assigns protonation locations, including the always ambiguous histidine, which has two neutral forms.

2.2.2 Membrane Structure Construction

To build a molecular model for a membrane-embedded system, the protein is usually inserted into a rectangular patch of a lipid bilayer. Prior to assemble a membrane system, it is important to consider what lipid composition is most appropriate for the transport protein in question. Single composition membranes containing phosphatidylcholine (PC) and phosphatidylethanolamine (PE) lipids are commonly used because they represent the largest components of steady state mammalian and bacterial cell membranes respectively [165, 166]. The location of the membrane protein must also be considered; mitochondrion, for example, have high levels of cardiolipin, a bacterial lipid not found elsewhere in mammalian cells [167]. Yeast and bacterial cells have a membrane composition that can differ substantially from mammalian cells. Context in which the transporter operates should be taken into account as well. For proteins function on activated platelets or cells undergoing apoptosis, such as the scramblases, it is likely that they interact more frequently with charged lipids flipped from the inner membrane [118]. Thus, in the scramblase systems, phosphatidylserine (PS)

lipids are also included in the inner leaflet of the membrane bilayer, in order to approximate the eukaryotic membrane *in vivo*, where PS is preferentially located in the inner leaflet. The PS concentration (33.3%) is strongly enriched in the mixed lipid composition, to enhance the chance for the embedded scramblase protein to interact with the lipids. This enrichment depends on the assumption that the protein in study locally enhance the concentration of certain lipids from the heterogeneous lipid distribution in live cells, and is likely true for proteins with specific lipid binding sites.

Once the lipid composition for the simulation has been determined, the CHARMM-GUI membrane builder [168] is used to generate a lipid patch of appropriate size for the system. CHARMM-GUI includes most physiological mammalian and bacterial phospholipids, permits the membrane geometry to be selected, and contains an interface to alternative membrane representations that accelerates lipid diffusion [169].

2.2.3 Membrane Protein Placement

Transmembrane proteins typically have a very distinct belt-like region in contact with the membrane. This region may not be obvious merely through visual inspection alone. In order to orient and place the protein correctly relative to the membrane, the PPM (Positioning of Proteins in Membrane) web server [170–173] is used to automatically identify the hydrophobic belt region of a transmembrane protein. This is done by minimizing the transfer energies of the membrane protein from water to an artificial lipid bilayer [173]. This is a crucial step because the function of the membrane protein is greatly affected by the lipid-protein interactions. Misplacement of the orientation of the protein and mismatch of the protein hydrophobic belt and membrane bilayer may lead to long equilibration requirements or misleading conclusions.

The module named "Membrane Builder" from the web application CHARMM-GUI [168,174,175] is then used for inserting the protein into the bilayer. The algorithm used by CHARMM-GUI "Membrane Builder" first determines the lipid head group position on the two membrane surfaces via a simulation with pseudo atoms that surround the embedded protein [174]. The pseudo atoms are then replaced by full lipids selected from a conformer library with 2000 distinct conformations

taken from a MD trajectory, generating a membrane embedded membrane protein.

2.2.4 Simulation Conditions

The membrane-embedded protein system is then placed in a box of water, and ions are added to achieve a desired concentration and a charge neutral system. The VMD plugin solvate was used for the solvation, and the TIP3P [176] was used as the water model. The VMD plugin autoionize was used for the ionization, where 150 mM NaCl was used for the simulations. In many cases, while functionally relevant molecules co-crystallized with the protein, such as ligands, are kept, remnants of the crystallization conditions, such as detergents, are removed from the system. While the force field parameters have been developed and optimized for standard molecular systems, such as protein residues, nucleotides, and lipid molecules [15, 177], parameters for ligands either have to be developed by analogy from the available force fields or parameterized using quantum mechanical methods used for force field development [178].

MD simulations were carried out with NAMD2.9 [179] using the CHARMM-CMAP and CHARMM36 force fields parameter sets [15, 177, 180, 181] to model the proteins and lipids, respectively. The periodic boundary condition (PBC) was used to surround the simulation box with an infinite number of copies of itself, thus minimize the surface effects due to the size of the simulated systems. The particle mesh Ewald (PME) method [182] was used to calculate long-range electrostatic interactions every 4 fs. A smoothing function was employed for van der Waals and short-range electrostatic interactions at a distance of 10 Å with a cutoff of 12 Å. The bonded interactions and the short-range non-bonded interactions were calculated every 2 fs. The pairs of atoms whose interactions needed to be evaluated (neighbor list) were updated every 20 fs. A cutoff (13.5 Å) slightly longer than the non-bonded cutoff was applied to search for the atom pairs. To reproduce physiological and experimental conditions, all simulation systems were subjected to Langevin dynamics [183] with the damping coefficient γ of 1 /ps and the Nosé-Hoover Langevin piston method [183–186] with the piston period of 200 fs to maintain the constant pressure ($P = 1$ atm) and temperature ($T = 310$ K) (NPT).

The simulations are started with a brief relaxation (1-5 ns) of the membrane and the solvent,

where the protein atoms are constrained to allow adjustment of the newly added environment of lipids and solvent to the protein. The production simulations are then performed after removing the constraints up to μs time depending on the system and the problem.

2.3 Nonequilibrium Simulations

Many biologically relevant phenomena in biomolecular systems generally take place in time-scales that are currently inaccessible to MD. To describe such long time-scale events, various nonequilibrium and biased simulations methods have been developed [187–194].

2.3.1 External Electric Field

Osmotic imbalances between the interior and the exterior of a biological cell cause electrostatic potentials of a few hundred millivolts across the membranes. Transmembrane potentials functionally affect the conformation and permeation properties of membrane proteins. With regard to the particular subject under investigation, ion permeation through the membrane protein could be facilitated by applying an external electric field to induce a voltage difference across a pore-containing membrane. The principles behind the such nonequilibrium simulations are the same of those behind the patch-clamp experiments, where electrodes are placed at opposite sides of a membrane to produce an electric field, in order to study the behavior of membrane proteins under the action of a controlled electrostatic potential. In these nonequilibrium simulations, the electric field, which is specified as a vector, is applied to all atoms in the system, resulting in an electrostatic potential drop across the simulation cell. Note that unusually large electrostatic potentials might be used in order to obtain results during the short time-scales achievable by simulations.

3 Differential Anion Binding and Proton Coupling in ClC-ec1[1]

3.1 Introduction

The coupling between the transport of different chemical species is at the heart of the mechanism of function of secondary transporters. In order to achieve stoichiometric transport of two ions, the transporter protein needs to be equipped with a precise molecular mechanism through which the translocation of the two (ionic) species are coupled. Despite the central role of this phenomenon in a large number of transporters, the underlying molecular mechanism is by and large lacking in the field of membrane transporters. This chapter investigates this mode of operation in a representative member of the H^+/Cl^- antiporters.

CLC transporters catalyze transmembrane exchange of Cl^- and H^+ necessary for pH regulation of key physiological processes [64–67]. One intriguing transport property of CLC proteins - both channels and transporters - is their ability to conduct various anionic species [50–55], namely, Cl^-, Br^-, I^-, NO_3^-, and SCN^-, with the permeability ratios varying within a factor of 10 for different anions and different CLC proteins [50–55, 195–197]. Characterizing the interaction of different permeant anions is of special significance in mechanistic studies of CLC transporters, due to widely different levels of H^+ coupling, or complete lack thereof, among different anions. While Cl^-, Br^-, I^-, NO_3^-, and SCN^- all can pass through the anion selectivity filter with similar efficiencies, they exhibit strikingly different couplings to H^+. In ClC-ec1, a prokaryotic homolog representing the best structurally and biophysically characterized CLC transporter, Cl^- is transported with strict

[1]The materials presented in this chapter were published in:
1) Giray Enkavi, Jing Li, Pochao Wen, Sundarapandian Thangapandian, Mahmoud Moradi, **Tao Jiang**, Wei Han and Emad Tajkhorshid,"A Microscopic View of the Mechanisms of Active Transport Across the Cellular Membrane".*Annual Reports in Computational Chemistry*, 10:77-125, 2014 [1].
2) **Tao Jiang**, Wei Han, Merritt Maduke, and Emad Tajkhorshid. Molecular Basis for Differential Anion Binding and Proton Coupling in the Cl^-/H^+ Exchanger ClC-ec1. *Journal of the American Chemical Society*, 138 (9):3066-3075, 2016 [3].

$2Cl^-/1H^+$ stoichiometry, whereas NO_3^- shows a weaker coupling of 7-10 NO_3^- for each H^+, and SCN^- is transported without any measurable H^+ transport, i.e., complete lack of coupling [55].

It is notable that the $2Cl^-/1H^+$ stoichiometry has been shown not only for bacterial ClC-ec1, but also for cyanobacterial syCLC [198], algal cmCLC [95], mammalian endosomal ClC-4, and ClC-5 [57, 59], and mammalian lysosomal ClC-7 [199]. Moreover, anion-dependent uncoupling has also been observed in ClC-4 and ClC-5, which show less H^+ countertransport with NO_3^-, and almost complete loss of H^+ transport with SCN^- [196, 197, 200].

Characterizing the interaction of the impermeant anion F^- is also of interest. For many years, it was thought that the F^- ion's lack of detectable permeation through CLC transporters [201] and channels [50,202] was due to the ion's strong hydration. However, a recent study demonstrated that the dehydrated F^- ion binds in the anion-permeation pathway with similar affinity to Cl^- [203]. While crystallography has pinpointed binding interactions [203], an understanding of the dynamics of these interactions will add critical detail to our understanding of the mechanism by which F^- inhibits the transport cycle. Worth noting, CLCs from a recently discovered prokaryotic clade, named CLC^F , function as F^-/H^+ exchangers [204–206]. These homologs are phylogenetically distant from the canonical CLCs: they share only ∼20% sequence identity even to other prokaryotic CLCs, and they lack key signature-sequence residues. Structures have not yet been determined for these unique CLCs. The focus of the work presented here is on the interaction of F^- with the canonical CLC transporters.

Even though the inner workings of Cl^-/H^+ exchange remains poorly understood, plenty of experiments and modeling studies of ClC-ec1 on the basis of its crystal structure have confirmed the importance of Cl^- occupancy at S_{cen} for the Cl^-/H^+ exchange and coupling [55, 60, 63]. Electrophysiological studies showed that substitution of small residues at Y445, one of the S_{cen} coordinating residues, leads to a loss of H^+ coupling to Cl^- transport [63,207], which strikingly correlates to the decrease of apparent halide occupancy at S_{cen} measured crystallographically [63]. The parallel loss of electrophysiologically measured H^+ coupling and crystallographically determined S_{cen} occupancy is also observed in wild-type (Y445-containing) ClC-ec1 when Cl^- is replaced by small non-halide anions [55]. For example, X-ray crystallographic analysis of ClC-ec1 demonstrated that $SeCN^-$ (the crystallographic analog of the uncoupling anion SCN^-) does not detectably occupy the S_{cen}

binding site [55]. Presumably, the partial uncoupler NO_3^- may partially occupy this site; however, the crystallographic resolution of ClC-ec1 structures are too low to unambiguously determine NO_3^- occupancy. The impermeant F^- can be discerned crystallographically at the S_{cen} binding site. Its strong H^+-bond to the protonated Glu_{ex} (mimicked by a Glu_{ex}–Gln mutation) provides a nice rationale for how this ion can halt the transport cycle [203]. However, there may be additional effects of the F^- ion not detectable in static crystal structures. To fully understand the relationship between anion binding and H^+ transport (and therefore the mechanism of coupling itself) we need to develop a deeper understanding of the detailed atomic interactions at the S_{cen} binding site.

Elucidating the degree of H^+ coupling to different anions in ClC-ec1 depends on the understanding of the H^+ transport pathway across the membrane. In contrast to the well defined Cl^- transport pathway [61, 63, 208], the H^+ pathway remains relatively under-investigated, except for the identification of the two critical H^+ transfer sites E148 (Glu_{ex}) and E203 (Glu_{in}) in ClC-ec1 [58, 62, 69, 70, 207, 209]. These two H^+ sites, however, are separated by a ∼15-Å hydrophobic region within the central part of ClC-ec1 void of any polar/charged groups capable of supporting H^+ transfer. Previous studies examining the H^+ transport mechanism suggested that water networks occupying the hydrophobic regions of proteins could be utilized as H^+ translocation pathways [82–87]. Earlier simulations in our group also revealed that dynamical hydration of the central region leads to spontaneous formation of water wires that connect Glu_{ex} and Glu_{in}, which is assisted by Cl^- ion bound at the S_{cen} site (Fig. 1.2B) [60]. These water wires may mediate H^+ transport between the two H^+-binding sites.

This chapter systematically evaluates the differential binding modes of chemically diverse anions at the S_{cen} site and their effect on water wire formation between Glu_{ex} and Glu_{in} in ClC-ec1 at an atomic level. The motivation was to construct a qualitative explanation that connects the chemical nature of anionic substrates with their ability to assist in the coupled H^+ transport. Our results infer that the difference in the anion/H^+ coupling is due to their influence on the formation of water wires connecting Glu_{ex} and Glu_{in}, which could be essential for H^+ transport. This view adds a crucial layer of detail to our understanding of the Cl^-/H^+ coupling mechanism.

3.2 Materials and Methods

3.2.1 Construction of the Membrane-embedded ClC-ec1 Model

The ClC-ec1 crystal structure (PDB ID: 1OTS, solved at 2.51 Å) [62], including all crystal water molecules, was used for the MD simulations. The program DOWSER [210] was used to guess additional water molecules within the protein. DOWSER placed 49 additional water molecules (referred to as "solvation" water molecules, hereafter) in energetically favorable positions. As suggested by multiple computational studies [87, 211, 212] using various force fields, one additional molecule was placed between the carboxylate group of E148 and the anion at S_{cen} in each subunit, in order to stabilize the two negative charges in close proximity. For the solvation water molecules (i.e., those added by DOWSER), those in the central hydrophobic lumen of the protein (referred to as the "hydrophobic region", hereafter) were removed prior the simulations to ensure that the hydration of the hydrophobic region is not artificially biased by our initial setup. E148 and E203 were modeled in their deprotonated (charged) forms, while E113 was protonated according to the thorough pKa analysis on titratable residues of the protein using Poison-Boltzmann electrostatic calculations [213]. The protein was embedded into a POPE lipid bilayer, fully solvated with TIP3P water [214] and buffered in 0.15 M NaCl. The resulting system, contained in a $105 \times 105 \times 110\,\text{Å}^3$ simulation box comprising of ∼110,000 atoms.

3.2.2 Simulation Protocols

Long Simulations

ClC-ec1 systems with either Cl^-, F^-, NO_3^-, or SCN^- bound at S_{cen} in both subunits were simulated. The simulation system of Cl^--bound ClC-ec1 was adopted from our previous study [60]. The systems with the other anions were generated by replacing the Cl^- at the S_{cen} site with either F^-, NO_3^- (N replacing Cl^-), or SCN^- (C replacing Cl^-). All simulation systems included ClC-ec1 dimers, therefore providing two independent copies of the anion-bound systems to be examined (we note that the two subunits in the crystal structure of ClC-ec1 are not identical).

For each of these four systems, 5000 steps of energy minimization were performed, followed by an initial equilibration of 1 ns, during which the protein atoms and oxygen atoms of the crystallographic water molecules were positionally restrained ($k = 2\,\text{kcal/mol/Å}^2$). Harmonic potentials ($k = 0.1\,\text{kcal/mol/Å}^2$) were also applied on water molecules to keep them out of the membrane. This stage allows the movement of lipids such that better packing around the inserted protein will be achieved. After the initial relaxation simulations, 350-400 ns of unrestrained simulations were performed for each system.

Short Simulations

To ensure that the absence of water wires in the case of SCN^- was not caused by the limited simulation time, an additional set of 20 short simulations in the presence of SCN^- were performed. Each simulation was initiated with a Cl^--bound ClC-ec1 structure containing the most representative water wire (obtained from the Cl^--bound simulation) [60]. The Cl^- was then replaced by SCN^- while keeping the pre-formed water wire. The system was then energy-minimized (5000 steps), and simulated for 0.5 ns with positional restraints on all protein atoms and oxygen atoms of the water wire (pre-equilibrium). Then 20 1-ns simulations with different initial velocities were carried out during which the stability and lifetime of the water wires were evaluated.

3.2.3 Analysis Tools

Pore radius profiles were calculated using HOLE [215]. Radial distribution function (RDF) calculations were performed using *g(r)* embedded in VMD. The hydrated radius was defined as a distance cutoff which encompassed the first density peak in the RDF. The coordination number was determined as the average number of protein or water hydrogen atoms within the hydrated radius.

3.3 Results and Discussion

3.3.1 Protein Stability

ClC-ec1 was simulated in the presence of four different anions (Cl^-, F^-, NO_3^-, or SCN^-), in order to investigate and compare the mode of binding of these ions and their impacts on protein structure and dynamics, and on the hydration pattern of the protein lumen. During the simulations, the overall protein structure remains stable (average backbone RMSD $< 1.5\,\text{Å}$ for each subunit), regardless of the type of anion bound at the S_{cen} site (Fig. 3.1(a)). The configuration of the anion conduction pore is also intact in the presence of different anions (Fig. 3.1(b) and (c)). In all the cases, the average pore radius profile of the anion conduction pathway follows the trend observed for the crystal structure (Fig. 3.1(c)). The two main bottlenecks, corresponding to the constriction regions that occlude the anion from the aqueous solutions, are clearly preserved, although the extracellular bottleneck shows a moderate ($\sim$0.5 Å) expansion relative to the crystal structure in all the simulated systems (Fig. 3.1(c)). In general, the overall structure and dynamics of the protein do not appear to be largely affected by the chemical nature of the bound anion.

3.3.2 Continuous Water Wires Arise in the Presence of Cl^-

Cl^- binds firmly at the S_{cen} site in both subunits, where it is coordinated by the backbone amide nitrogen atoms of I356 and F357, and by the side-chain oxygen atoms of S107 and Y445 (Fig. 3.2(a)). The average interaction energies between the Cl^- at S_{cen} and individual residues throughout the protein indicate that the Cl^- binding is mainly supported by residues from three motifs: GIFAP, GSGIP, and Y445 (Fig. 3.2(b) and Fig. 3.3). The Cl^- coordination shell, involving both surrounding protein residues and water molecules, is examined in detail by calculating the anion-hydrogen RDF for protein and water hydrogen atoms, respectively (Fig. 3.4). The RDF analysis reveals that the bound Cl^- is coordinated, on the average, by five hydrogen atoms, with $\sim$1.6 of them originating from water molecules (Fig. 3.6). To monitor the fluctuations of the Cl^- coordination shell, we quantified separately the involvement of protein residues and water molecules in the coordination shell during the course of the simulation (Fig. 3.5). In both subunits, the Cl^- ion is coordinated

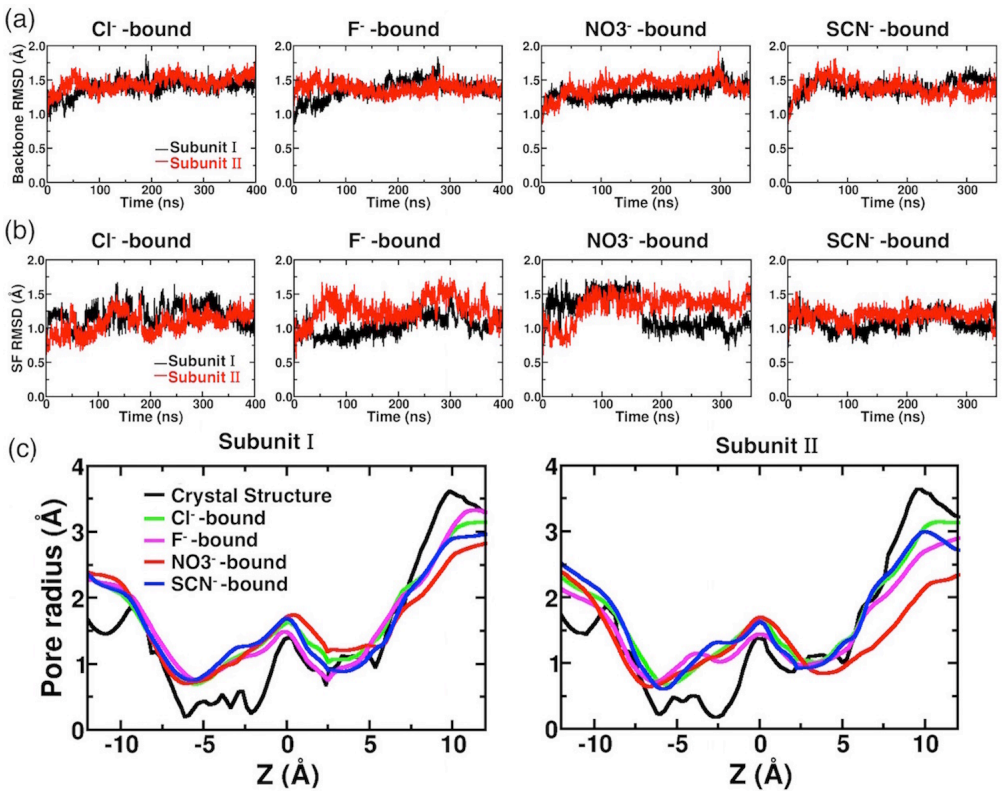

Figure 3.1: Protein structural dynamics in the presence of different anions. **(a)** Backbone RMSDs of individual subunit shown as a function of simulation time for anion-bound simulations. **(b)** The RMSDs of all heavy (non-hydrogen) atoms of the selectivity filter (SF) in the presence of different anions. **(c)** Comparison of pore radius profiles of the crystal structure (black) and those of MD simulations (averaged over the whole trajectory) with different anions bound at S_{cen} (colored traces). The center of the bound anion at $t = 0$, which corresponds to the Cl^- position in the crystal structure, is set as the origin. The extracellular side is towards the left ($z < 0$), and the intracellular side is towards the right ($z > 0$).

mainly by protein residues during the first 100 ns. Later, the ion becomes hydrated by 2-4 water molecules located nearby S_{cen}, usually lining the central hydrophobic region between Glu_{ex} and Glu_{in}.

To understand in detail the influence of Cl^- on the surrounding water molecules that fall between the two H^+ sites, we characterize further the distribution of the Cl^- hydration water molecules along the axis defined by the carboxylate groups of Glu_{ex} and Glu_{in} that is, the putative H^+ pathway axis, see Fig. 3.6 (b)). A water molecule was considered as a hydration water molecule if the shortest Cl^--water distance falls within 3 Å. For both subunits, hydration water molecules are observed uninterruptedly along the H^+ pathway axis, including the region right next to the Cl^- ion ($z = 0$ Å, Fig. 3.6(c)). The presence of a continuous array of hydration water molecules implies

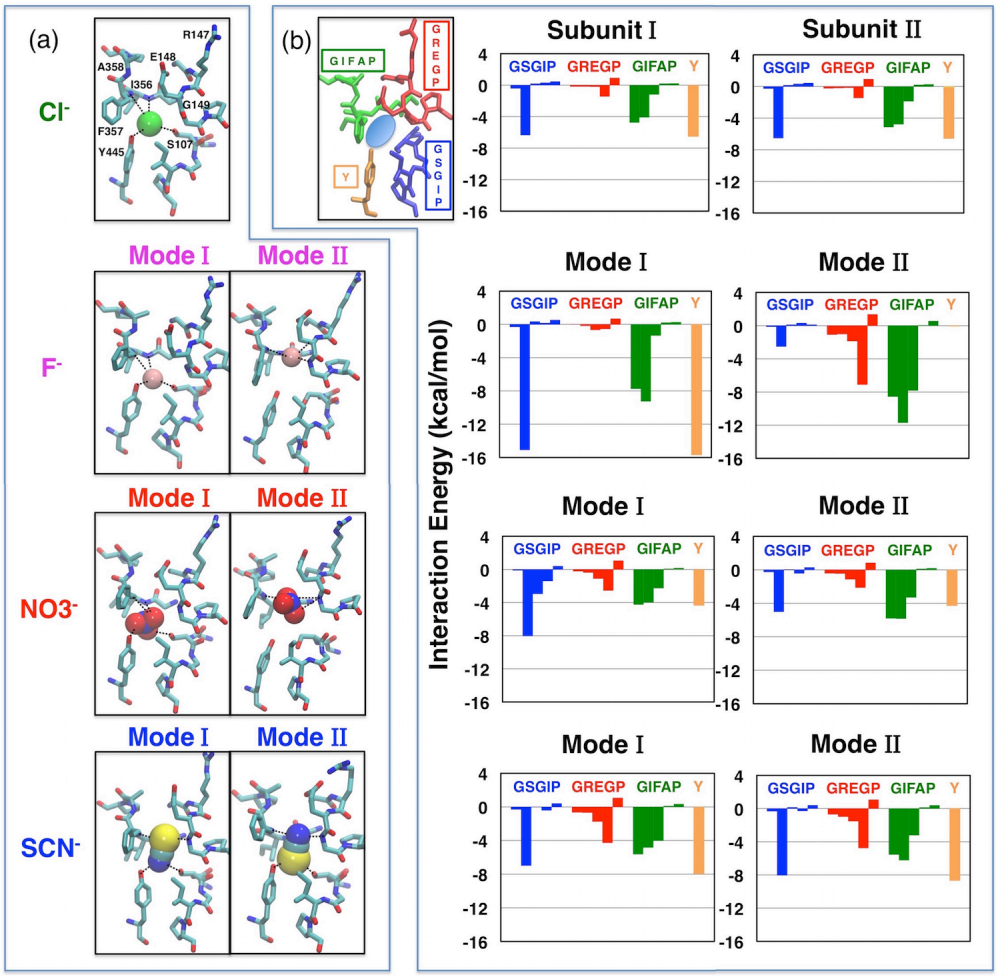

Figure 3.2: Anion binding modes. **(a)** Cl^-, F^-, NO_3^-, and SCN^- (shown in van der Waals) bind distinctively in the selectivity filter. For F^-, NO_3^- and SCN^-, two binding modes (Modes I and II) are observed in the two subunits. Cl^- exhibits only one binding mode. Selected residues in the vicinity of the bound anions are shown. Coordinations of the bound anions by the protein residues are shown as dashed lines. **(b)** Interaction energy between the bound anion and the four highly conserved motifs. Motifs (colored and labeled in the left panel) forming the selectivity filter contribute the majority of the interaction energy between the anion and protein. Residues in the rest of the protein show negligible anion-interaction energies (absolute value < 0.3 kcal/mol per residue, with the exception of K131 (-0.3 – -0.7 kcal/mol)).

a favorable environment for hydrogen-bonded water wire to arise nearby the Cl^- ion. Consistent with this expectation, formation of continuous water wires is observed in both subunits of Cl^--bound ClC-ec1 during the simulation [60]. Although the frequency of water wire formation in Subunit I is almost three times of that in Subunit II, in both subunits water wires containing 6-7 water molecules arise frequently (Fig. 3.7(a)). The different behaviors observed in the simulations for the two subunits may be due to the minor structural asymmetry of the subunits in the crystal

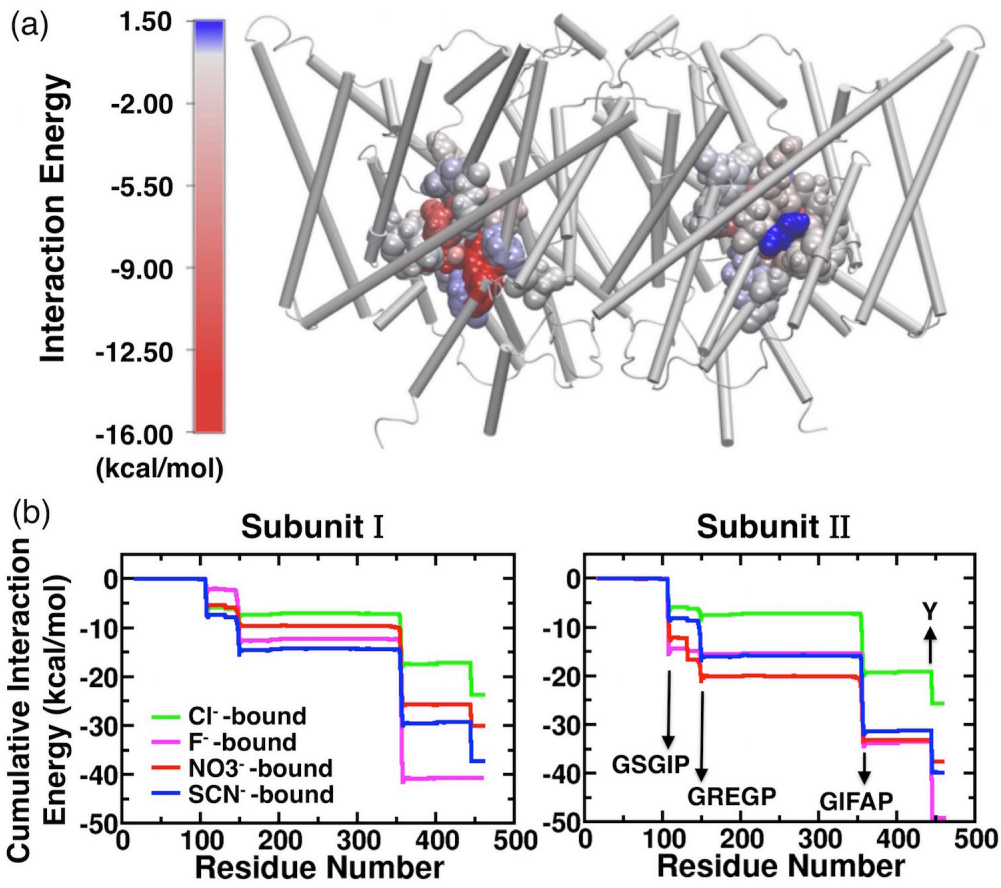

Figure 3.3: Interaction energy between the anions at S_{cen} and ClC-ec1. **(a)** A representative system used to map the interaction energies on the protein. The protein is colored according to the residue-based interaction energies with F^-, which has very strong interactions with the binding-site residues. Bound F^- ions are shown as pink spheres. Residues with absolute interaction energy values larger than 0.1 kcal/mol are shown in van der Waals. **(b)** and **(c)** Cumulative interaction energies between the bound anion and protein are in the order of $F^- > SCN^- > NO_3^- > Cl^-$ in both subunits. Each sharp drop in the plots is resulted from the strong interaction with a conserved motif within the ion-binding region (see Fig. 1).

structure (Fig. 3.1(a) and (b)), which results in differences in the micro-environments of the binding sites and individual conduction pores. We note that the two subunits mediate Cl^-/H^+ exchange independently [216].

3.3.3 Pseudo-water-wires Form in the Presence of F^-

F^-, which has a radius $\sim$0.5 Å smaller than Cl^-, displays two binding modes around the S_{cen} site (Fig. 3.2(a)). In Subunit I, F^- binds firmly at S_{cen} (similar to what was observed for Cl^-),

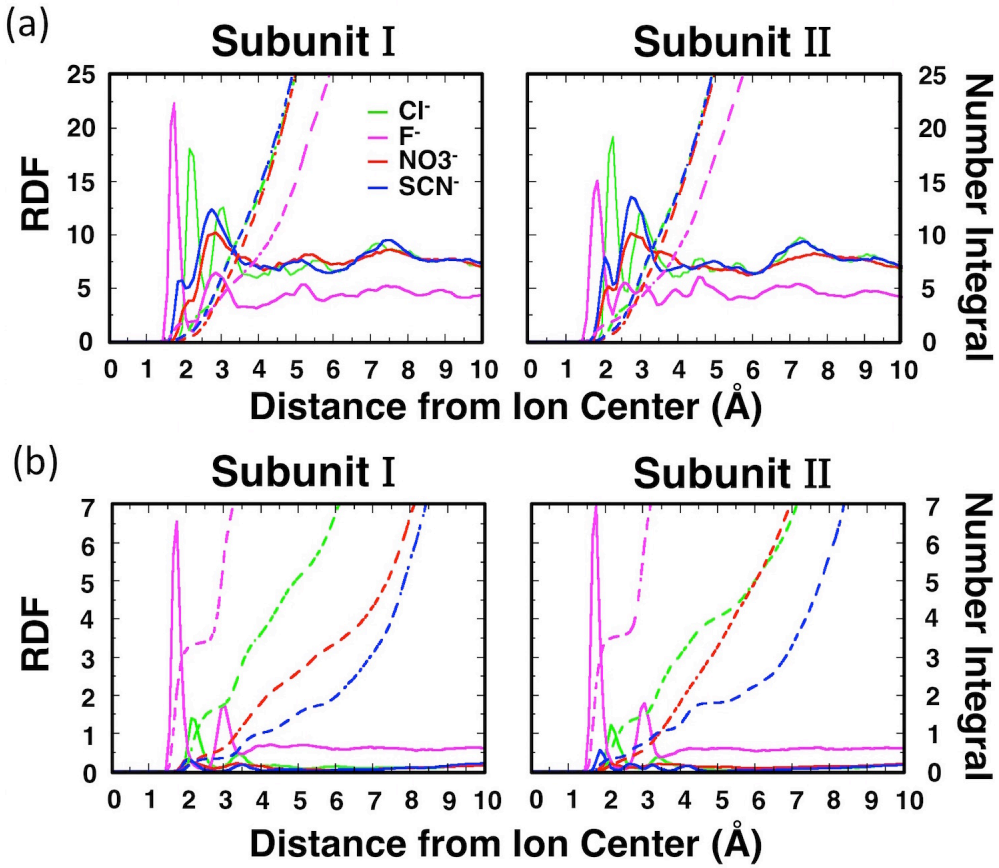

Figure 3.4: Anion-hydrogen RDF for S_{cen} bound anions with protein or water hydrogen atoms. RDF indicates the variation of amino acid hydrogen density **(a)** or water molecule hydrogen density **(b)** with distance from the center of the anion. The number integrals are represented by dashed lines. The first hydration shell is defined by the first minimum after the major peak of the RDF, and the coordination numbers are obtained by the corresponding number integral.

while in Subunit II, it moves upward after ∼40 ns and adopts a stable position somewhere between S_{cen} and E148 for ∼340 ns, with E148 side chain moving slightly toward the extracellular side (Fig. 3.2(a)). The upward movement of F^- results in hydrogen bond interactions between the F^- ion and backbone nitrogen atoms of E148 and G149; meanwhile, F^- loses its direct contacts with S107 and Y445 hydroxyl groups on the opposite side. Switching between these two binding modes arises only in Subunit II on the timescale of our simulation.

The average coordination number for F^- is slightly over 5 in both binding modes, which is comparable to that of Cl^-. However, a relatively larger portion of the coordination is contributed by water molecules (∼3.5, Fig. 3.6(a)). Moreover, the simulation trajectory in the presence of F^-

shows no apparent dehydration phase for F^- as seen in the first 100 ns simulation with Cl^-. The F^- ion becomes hydrated quickly after the simulation starts and remains coordinated by ∼3 water molecules throughout the simulation (Fig. 3.6(a) inset and Fig. 3.5). Due to its strong tendency for hydration, F^- exhibits a different arrangement of hydration water molecules when compared to Cl^-. In the Cl^--like binding mode (Mode I), F^- is coordinated by water molecules from above ($z > 0$; extracellular side), while contacting the side chains of S107 and Y445 on the opposite side. In binding Mode II, F^- is sandwiched by water molecules both from above ($z > 0$) and below ($z < 0$) (Fig. 3.6(c)).

The distinct pattern of hydration of F^- appears to be the main reason for not observing the formation of continuous water wires between Glu_{ex} and Glu_{in} in either subunit during the simulation. Detailed inspection revealed that in binding Mode II, F^- can be actually connected to Glu_{ex} and Glu_{in} by separate, shorter water wires, involving about 7 water molecules. The separated water wires together with the F^- ion form pseudo-water-wires connecting the two H^+ sites that are however intervened by the anion (Fig. 3.7(b)), indicating an essential difference between F^- and Cl^-.

3.3.4 Shorter Pseudo-water-wires Intervened by NO_3^-

NO_3^- is a polyatomic anion and exhibits a more complex chemical structure involving three oxygen atoms at corners of a triangle sharing the negative charge around a central nitrogen atom. Similar to the F^--bound system, the simulation of ClC-ec1 with NO_3^- reveals two possible binding modes for the anion. In Mode I, NO_3^- is fitted into S_{cen} with one of its oxygen atoms coordinated by the backbone nitrogen atoms of I356 and F357, and the other two oxygen atoms coordinated by the side chain hydroxyl groups of S107 and Y445, respectively (Fig. 3.2). Mode I is relatively more populated and is observed in both subunits. In Mode II, NO_3^- exhibits a similar behavior to F^- in its binding Mode II, in that NO_3^- moves upward to a position between S_{cen} and E148 and pushes away E148 side chain by ∼2.30 Å. This binding mode involves hydrogen bond interactions between the oxygen atoms of NO_3^- and the backbone nitrogen atom of G149, instead of direct interaction with S107 and Y445 hydroxyl groups (Fig. 3.2). Binding Mode II only occurs in Subunit I for ∼150 ns (t = 10-160 ns), before NO_3^- moves back to the original, S_{cen} binding site.

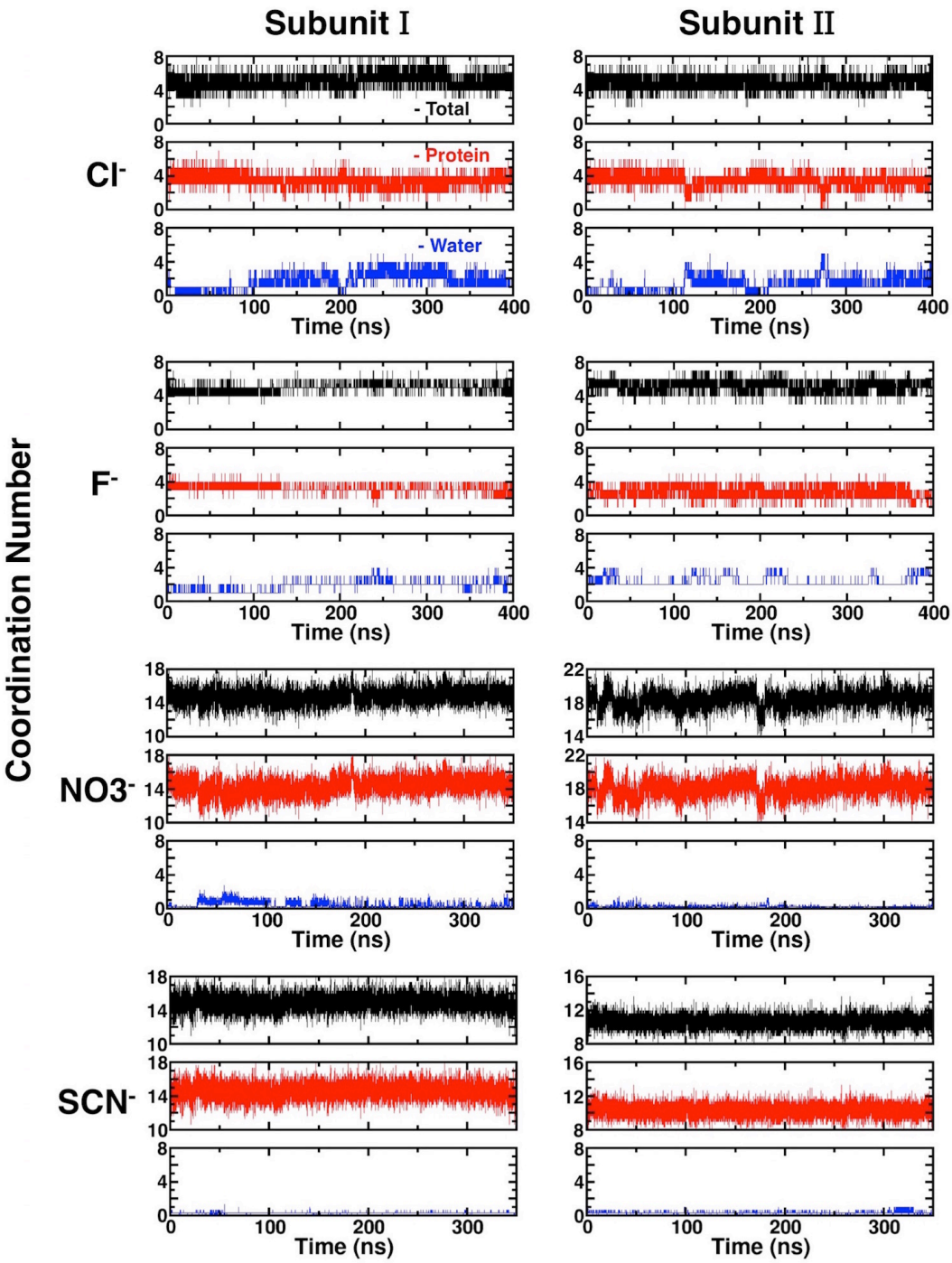

Figure 3.5: Coordination number of bound anions as a function of simulation time. Panels from top to bottom in each case denote the coordination number for all ligands (black), for protein hydrogen atoms only (red), and for water hydrogen atoms only (blue), respectively. The scales for coordination number (y axis) are different, but the range is 8 Å for all panels. The coordination numbers of NO_3^- and SCN^- show large fluctuations due to their extensive coordination to the protein. Both NO_3^- and SCN^- are minimally hydrated during the simulations compared to the halide anions Cl^- and F^-.

According to the RDF profiles, NO_3^- establishes a more extensive coordination to its environment compared to Cl^- and F^-, but much fewer of them ($\sim$0.5) arise from anion-water interactions (Fig. 3.6(a) and Fig. 3.4), suggesting that this large polyatomic anion relies less on interaction with water in order to be stabilized when bound at S_{cen}. During the simulation, NO_3^- is only minimally hydrated (Fig. 3.5), resulting in differential hydration configurations along the H^+ pathway axis (Fig. 3.6(c)).

In binding Mode I, hydration water molecules are observed along the H^+ pathway axis except for the area right beside the anion ($z = 0$), while in binding Mode II, only the region above the bound NO_3^- is hydrated ($z > 0$, Fig. 3.6(c)). As a result, pseudo-water-wires only arise when the anion is in binding Mode II. Compared to the pseudo-water-wires formed in the presence of F^-, those involving NO_3^- favor shorter water wires, often containing only four water molecules (Fig. 3.7(c)). The difference between the pseudo-water-wires involving F^- and NO_3^- can be attributed to the different sizes of the anions. In particular, due to its geometry involving multiple negatively charged sites (oxygen atoms), NO_3^- appears larger effectively reducing the spatial gap between the Glu_{ex} and Glu_{in} for formation of pseudo-water-wires.

3.3.5 SCN^- Eliminates the Water Wires

The other polyatomic anion investigated, SCN^-, has a linear chemical structure which extends to 4.77 Å in length [217]. Due to its long shape, SCN^-, which was initially centered at S_{cen} in both subunits, rotates and shifts immediately after the simulation starts in order to optimally fit into the available space, resulting in two different binding orientations in the two independent subunits (Fig. 3.2(a)). Both binding orientations of SCN^- were stable over the simulation time.

Because of its larger size, SCN^- occupies S_{cen} while extending almost to S_{ext} in both orientations, stabilized by its interaction (7-8 kcal/mol) with motif GREGP (Fig. 3.2(a) and (b)). In one orientation (Mode I), the sulfur atom of SCN^- is coordinated by the backbone nitrogen atoms of G149, I356, and F357, while the nitrogen atom of the anion is coordinated by the side-chain hydroxyl groups of S107 and Y445. In the alternative orientation (Mode II), SCN^- adopts an opposite configuration and binding coordination (Fig. 3.2(a) and (b)).

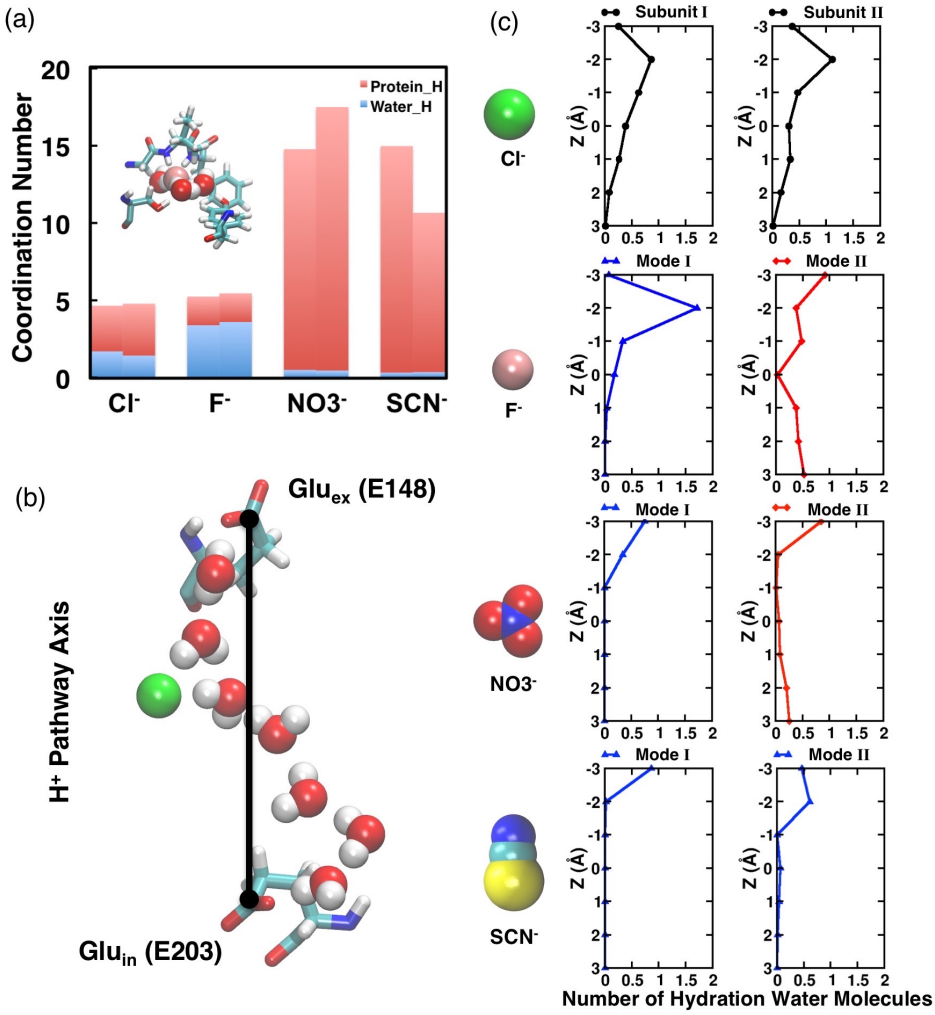

Figure 3.6: Anion solvation by protein and water. **(a)** Anion coordination numbers obtained from radial distribution function (RDF) analysis (see Fig. 3.4) with protein or water hydrogen atoms. Inset shows an example of anion coordination, depicting F^- surrounded by at least three water molecules on the average. **(b)** The H^+ pathway axis is defined by the Glu_{ex} and Glu_{in} carboxylate groups. **(c)** The distributions of anion hydration water molecules along the H^+ pathway axis. Blue curves (▲) indicate the anion hydration water is only located above the anion ($z > 0$, extracellular side); red curves (⧫) indicate the anion hydration water is observed both above ($z > 0$, extracellular side) and below ($z < 0$, intracellular side) the anion; and black curves (●) indicate the anion hydration water exists along the H^+ pathway axis including the region right next to the anion ($z = 0$). The center of the bound anion is set as the origin.

SCN^- fills up a larger portion of the space within the binding region, resulting in very large coordination to its environment (Fig. 3.6(a)). RDF calculations revealed that SCN^- is only weakly hydrated in either binding mode, with only ∼0.3 of the coordination arising from anion-water interactions (Fig. 3.6(a) and Fig. 3.4). Specifically, the hydration water molecules are only observed above the bound SCN^- ion ($z > 0$) in either binding mode (Fig. 3.6(c)). Hydration from the other

side of SCN^- (below it, $z < 0$) is not observed, since the central hydrophobic region remains dehydrated in the presence of this anion. Consequently, neither water wires nor pseudo-water-wires are observed to form in the presence of SCN^- (Fig. 3.7(d)), suggesting that water wires necessary for H^+ are unlikely to be supported by this anion.

To preclude the possibility that the absence of water wires in the case of SCN^- was merely due to the limited simulation time, we also examined the stability of pre-formed water wires in the presence of SCN^- through a set of short simulations. These simulations all started from a configuration in which the water wires had been formed (adopted from Cl^--bound simulations), and were done in the presence of SCN^-. The pre-formed water wires diminish quickly in all the simulations, and SCN^- breaks the water wires immediately after the simulations start, by inserting either its sulfur or nitrogen atom into the water wires (Fig. 3.6(e)). The lifetime of water wires averaged over 20 1-ns runs is 0.024 ± 0.026 ns with SCN^-, which is significantly shorter than 0.6 ± 0.2 ns for Cl^--bound ClC-ec1 [60].

3.4 Summary and Perspective

The molecular origin of coupled Cl^-/H^+ exchange is a central mechanistic aspect of CLC transporters. Understanding the atomic details underlying differential H^+ coupling of various anions constitutes a major question that motivated this study. To address this question, we performed extended equilibrium MD simulations to investigate differential binding modes of different anions transported by ClC-ec1 to S_{cen} and to determine whether and how they may affect the formation of water wires within the lumen, which in turn may be an important component of the H^+ transport reaction [60, 87]. The most important points of the simulation study with ClC-ec1 are summarized below.

(1) **Bound protein structure** X-ray crystallographic studies of ClC-ec1 suggest that the bound anion does not induce major changes in the overall structure of the protein [55]. Our RMSD results and pore profile calculations (Fig. 3.1) confirm that the protein structure is not compromised by binding of the studied anions, which also include large, non-halide species, and that the binding site/region can accommodate both the physiologically relevant Cl^- ion as well as other anions,

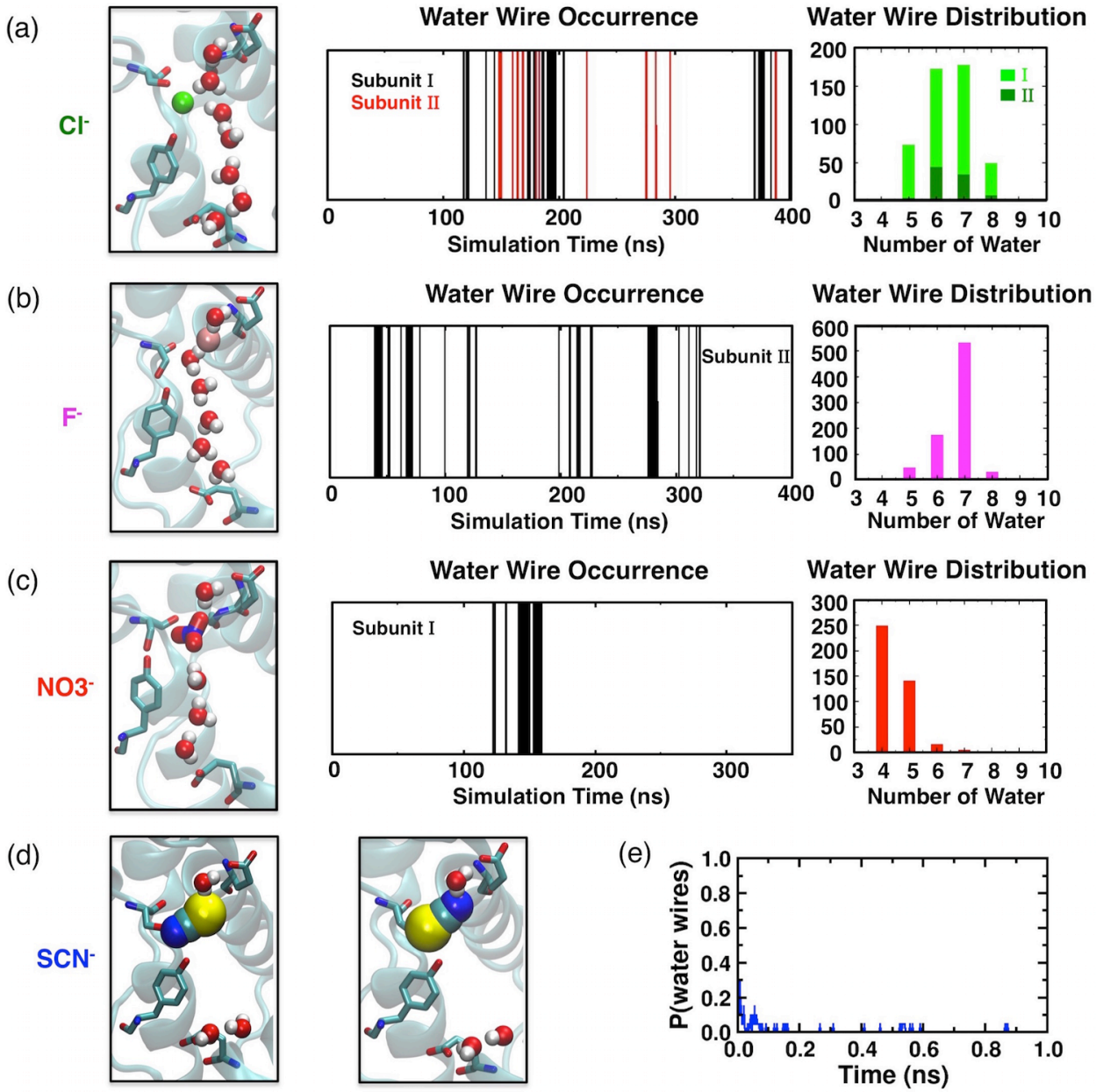

Figure 3.7: Effect of anion bound at S_{cen} on formation of water wires. **(a)** Continuous water wires arise in both subunits in the presence of Cl^- [60], following a normal distribution dominated by configurations including 7 water molecules. **(b)** Pseudo-water-wires are observed only in Subunit II when F^- binds in binding Mode II. Those intervened wires follow a normal distribution dominated by 7 water molecules. **(c)** Pseudo-water-wires formed in Subunit I when NO_3^- binds in binding Mode II and follow an exponential distribution dominated by 4 water molecules due to the large size of NO_3^-. **(d)** Neither water wires nor pseudo-water-wires are observed in the presence of SCN^-. **(e)** Average probability of water wires obtained from short (1 ns) simulations of ClC-ec1 with SCN^- bound, starting from a pre-formed configuration of the most representative wire structure.

namely F^-, NO_3^-, and SCN^- (Fig. 3.1). Although the overall protein structure does not seem to be affected by the type of anion bound at S_{cen}, the details of the coordination and interaction between the bound anion and protein/water vary significantly among the anions examined (Fig. 3.2 and Fig. 3.6). X-ray crystallography of anion-bound ClC-ec1 suggests that F^- binds to S_{cen} similarly to the biological substrate Cl^- [203]. NO_3^- and SCN^- have not been unambiguously localized, and their binding modes not well characterized in ClC-ec1, due to low crystallographic resolution [55].

(2) **Anion binding mode** The present study provides a detailed description of the binding modes of these anions in ClC-ec1. In contrast to Cl^-, which binds stably at S_{cen}, the same site observed in the Cl^--bound crystal structures [61, 62], both F^- and NO_3^- are found to populate two different binding positions (modes), one located at the original S_{cen} site, and the other located between S_{cen} and E148. SCN^-, due to its extended shape, occupies S_{cen} while extending almost to S_{ext} with two possible (opposite) binding orientations. Despite the differential binding modes, all anions stay at or around the S_{cen} site, during the simulations, where they are stabilized by several conserved motifs (Fig. 3.2). However, the cumulative interaction energy between the anion and the protein varies in the order of $F^- > SCN^- > NO_3^- > Cl^-$ in both subunits, with the stabilization of F^- almost twice as favorable as that of Cl^- (Fig. 3.3).

(3) **Anion hydration feature** In a previous computational study, Ko and Jo showed that Cl^- was coordinated by protein hydrogen atoms and no water molecules were observed along the Cl^- conduction pore when E148 was protonated and Cl^- was pulled from the intracellular side to the extracellular side along the pore axis [218]. Several other simulation studies focusing on anion conduction, however, suggested that Cl^- is partially hydrated [87, 211, 212, 219]. Our recent study revealed that water molecules can enter the anion-binding region via the H^+ pathway and hydrate the initially dehydrated Cl^-, a feature which we proposed to be critical to H^+ transport in ClC-ec1 [60]. Therefore, the configuration of the anion coordination shell, including the number of water molecules in the first coordination shell, as well as the size and shape of the anion within this shell, can be critical to anion-coupled H^+ transport by the protein [220, 221]. RDF and related calculations reveal that the anions at S_{cen} exhibit two types of coordination shell structures, with distinguishable number of coordinations from protein and water molecules (Fig. 3.6(a)). Halide anions (Cl^- and F^-) both exhibit an average coordination number of $\sim$5, while the polyatomic

anions (NO_3^- and SCN^-) establish a more extensive coordination (number of coordination > 10) to their environment. Under equilibrium conditions, the physiologically transported anion, Cl^-, is the only one that supports full hydration along the H^+ pathway axis (Fig. 3.6(c)), which we showed to be a prerequisite for water wires to arise and connect Glu_{ex} and Glu_{in} [60].

(4) **Water wire types** The observation that the anions at S_{cen} exhibit distinct coordination structures and hydration shells suggests that the functionally important water wires, which need to arise nearby the anions, could experience different environments. Thus, we investigated further the effect of various anions at S_{cen} on the formation of water wires. Different types of water wires were observed for various anions (Fig. 3.7). They can be classified into two types based on the pattern of interaction with the bound anions as well as their configurations: (i) continuous water wires, supported by the anion located nearby, which connect the two H^+ sites seamlessly, and (ii) pseudo-water-wires, where the anion participates in the wire and prevents water molecules from forming a continuous hydrogen-bonded chain connecting the two H^+ sites. The continuous water wires are only observed in the presence of Cl^-, while the pseudo-water-wires were observed for both F^- and NO_3^- in their alternate binding modes (Mode II).

(5) **Insight on F^-** Lim and colleagues recently showed that F^- is coordinated much like Cl^- at S_{cen} [203]. They also showed that F^- binding to this site forms a strong hydrogen-bond to the protonated Glu_{ex}, as revealed by the short distance between the F^- ion and the Gln side-chain in the E148Q mutant (where Gln mimicks the protonated Glu_{ex}). This strong hydrogen bond likely plays a key role in slowing the transport cycle. However, there may be additional factors contributing to the complete lack of F^- transport. A hint that other factors may be involved is suggested by the fact that the inner-gate mutant Y445A, which destabilizes Cl^- (and presumably F^-) binding to S_{cen} (see Introduction) retains wild-type selectivity against F^- [203]. Our observation of the binding Mode II for F^- provides a microscopic view of how F^- can bind in the permeation pathway away from the S_{cen} site. The pseudo-water-wires arising in this binding mode are likely an additional key contributor to the transport selectivity against F^-. This picture provides a compelling rationale for the wild-type selectivity against F^- observed in the Y445A mutant: since the pseudo-water-wires only occur in binding Mode II, in which F^- loses its direct contacts with S107 and Y445 hydroxyl groups, the Y445A mutation will not affect the behavior of the protein toward F^-. In the future,

it will be of interest to determine whether water wires play a role in the mechanism of the CLC^F exchangers. Such an idea is speculative, given that the exchange stoichiometry of $1F^-$:$1H^+$ implies a significantly different exchange mechanism from that occurring in the canonical 2:1 Cl^-:H^+ CLCs. Addressing this important question awaits a high-resolution structure of the CLC^F homologs.

(6) **Insight on NO_3^-** NO_3^-, like F^-, induces the formation of pseudo water wires that are intervened by NO_3^- itself. Such water wires could allow occasional transport of H^+, but with less fidelity than the pure water wires observed with Cl^-. These pseudo water wires arise in binding Mode II, where the NO_3^- ion moves upward and has no direct interaction with the S_{cen}-coordinating residues S107 and Y445, which in losing their interaction with the ion form a hydrogen bond one to another (Fig. 3.2(a)). Such a binding mode is never observed with Cl^-. Thus, the simulation predicts that these two residues are determinants of Cl^-/NO_3^- selectivity. Consistent with the prediction, certain plant CLC homologs that function as 2:1 NO_3^-:H^+ exchangers [222] have a proline at position 107, which is a serine in all 2:1 Cl^-:H^+ exchangers. In ClC-5, mutating the serine to a proline partially reproduces the plant phenotype, reducing the NO_3^-/H^+ stoichiometry from ∼10-25 to ∼2-8 (over the +60-120 mV voltage range examined) [223,224]. In ClC-ec1 mutating this serine to a proline increases the binding affinity for NO_3^- ∼4-fold [208]. Though it is not yet known whether this change in binding affinity is paralleled by a change in $NO3_3^-/H^+$ stoichiometry, a crystal structure of this ClC-ec1 mutant together with MD simulations might further illuminate mechanism of $NO3_3^-/Cl^-$ selectivity in CLC anion/H^+ coupling.

(7) **Insight on SCN^-** Early experimental studies showed a striking correlation between anion occupancy at S_{cen} and Cl^-/H^+ coupling stoichiometry in ClC-ec1. Specifically, the halides Br^- and Cl^- are transported with a strict 2:1 exchange ratio to H^+, whereas the pseudo halides, SCN^- and $SeCN^-$, are transported in a completely uncoupled manner [55]. In ClC-ec1 crystal structures, Br^- density is clearly observed at S_{cen}, while $SeCN^-$ is not [55]. Although difficult to interpret these data mechanistically, it was speculated that low occupancy at S_{cen} could somehow promote occasional simultaneous opening of the inner and outer gates (which are in direct contact with S_{cen}), thus creating an anion leak that degrades the coupling stoichiometry. Our simulation results provide an alternative explanation for uncoupling transport of non-halides: the disruption of water wires that facilitate H^+ transfer between Glu_{ex} and Glu_{in}. The uncoupling ion SCN^- remains bound

in the vicinity of S_{cen} (within the simulation time), but it is unable to sustain water wires. In this model, uncoupled SCN^- transport need not necessarily involve simultaneous opening of both gates but could entail alternate opening of gates, similar to the alternate opening of gates that occurs in the coupled transporter but no longer coordinated with H^+ transport. Such an uncoupling mechanism has precedent in ClC-ec1 Glu_{ex} mutations, where uncoupled Cl^- transport involves protein conformational change similar to that observed in the coupled transporter [225]. The idea that uncoupled Cl^- and SCN^- transport share some similarities is consistent with the observation that mutations at Glu_{in} dramatically slow both Cl^- and SCN^- transport in ClC-5 [196]. We note also that our observation of SCN^- binding to S_{cen} is not inconsistent with the crystallographic studies, in which the lack of anion density at S_{cen} could reflect high disorder rather than lack of occupancy.

4 Comparing Anion Selectivity in ClC-ec1 and S107P Mutant

4.1 Introduction

The transport cycle of membrane transporters involves conformational changes at diverse length and time scales. Some of these conformational changes, e.g., local rearrangements of side chains, localized motions of loops, and even those of helices, can be characterized within the time scales accessible to equilibrium MD simulations. These local structural changes can be captured by MD as a manifestation of the natural vibrational motions of the protein as a response to the thermalization of the crystal structure in its natural environment composed of lipids and water. Sometimes, the structural changes take place beacause of specific simulation conditions, for example, in response to placing/removing substrates, mutating residues, protonation/deprotonation events, etc. Such conformational changes have been successfully elucidated by MD simulations of a large number of membrane transporters [16–39, 226–228]. This chapter examines the local conformational change induced by a single mutation in the S_{cen} of ClC-ec1, which affects the binidng of anions at the S_{cen} site, thus may influence the transport and coupling mechanism in the H^+/Cl^- antiporters.

CLC transporters are known to exchange various inorganic anions with H^+ countertransport [229, 230]. Proper function of the CLC transporters is strongly substrate dependent: different anions markedly alter the degree of H^+ coupling in the transporters. As discussed in **Chapter 3**, the anion-dependent uncoupling has been observed in several CLC family members, including bacterial ClC-ec1, as well as mammalian endosomal ClC-4 and ClC-5 [196,197,200], which normally exchange two Cl^- ions with one H^+ across the cellular membrane during each transport cycle [57, 59, 64, 68]. It is notable that the 2:1 anion:H^+ stoichiometry has been shown not only for Cl^- ions, but also for NO_3^- ions in certain plant CLC homologs [222]. Although these plant CLC transporters share the same fundamental property of being anion/proton exchangers, they display different anionic

specificity compared to their bacterial and mammalian homologs. Understanding the molecular origins of anion selectivity is essential to the overall understand of the H^+ coupling mechanism in CLCs.

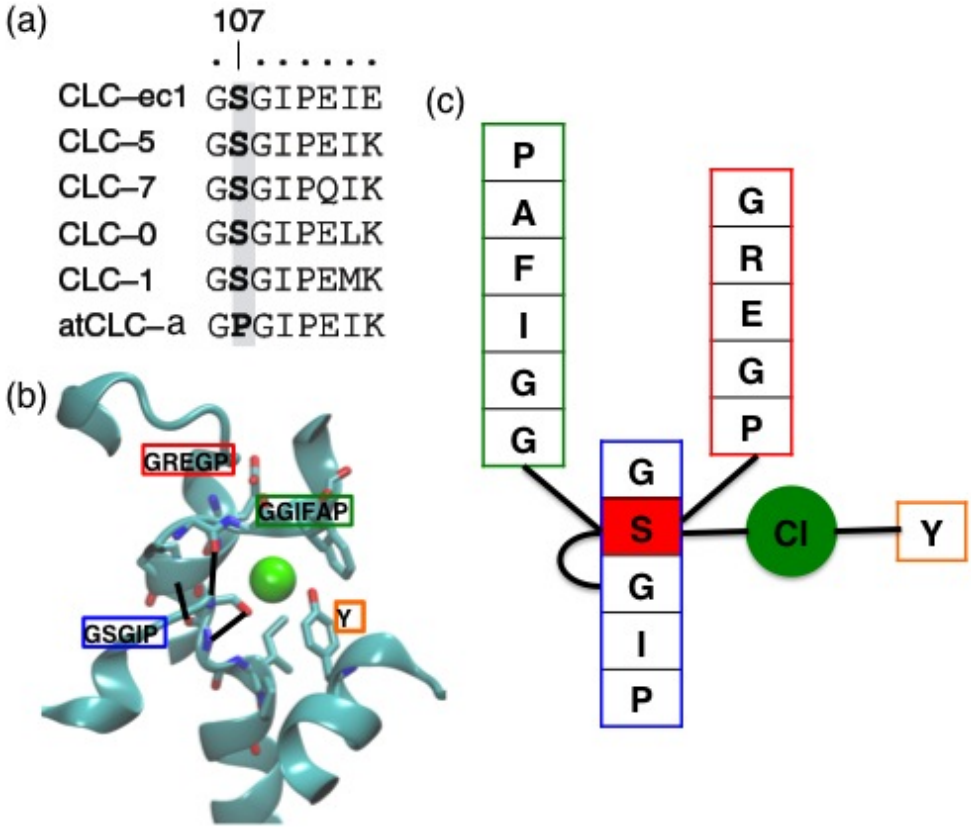

Figure 4.1: The role of S107 in regulating selectivity and anion binding. **(a)** The alignment of a sequence stretch comprising the conserved serine (highlighted in bold on a gray background) in several CLC channels and transporters. **(b)** S107 in ClC-ec1 forms multiple hydrogen bonds with several highly conserved residues from the ion-binding motifs. **(c)** Schematic illustration showing S107 connects the four functionally important motifs as well as the S_{cen} bound Cl^- through hydrogen bonding.

ClC-ec1 and ClC-5 mediate stoichiometrically coupled $2Cl^-/1H^+$ exchange, but the NO_3^- transport is largely uncoupled from H^+ [55,57,59]. By contrast, the plant AtClC-a has been shown to be able to mediate tightly coupled $2NO_3^-/1H^+$ exchange more efficiently than Cl^-/H^+ exchange [222]. Comparison of the transporter sequences identified a proline in AtClC-a that is replaced by serine in the bacterial and mammalian CLC isoforms (Fig. 4.1(a)). This residue is located in the highly conserved motif GSGIP (106-110) known to form the S_{cen}, and is responsible for the coordination of the bound Cl^- according to the ClC-ec1 crystal structures. In addition, the NO_3^- binding mode

described in **Chapter 3** also suggests that the S_{cen}-coordinating residue S107 may determine the Cl^-/NO_3^- selectivity. Notably, when the proline was mutated to serine in AtClC-a, its Cl^-/H^+ exchange proceeded as efficiently as NO_3^-/H^+ exchange [231]. When the corresponding serine of ClC-5 was replaced by proline, this Cl^-/H^+ exchanger gained efficient NO_3^-/H^+ coupling [223]. To be specific, the mutated ClC-5 partially reproduces the plant phenotype, reducing the NO_3^-/H^+ stoichiometry from $\sim$ 10-25 to $\sim$2-8 (over the +60-120 mV voltage range examined) [223, 224]. In ClC-ec1, the serine-to-proline substitution at this site confers NO_3^- selectivity upon the Cl^--specific ClC-ec1 transporter by enhancing NO_3^- binding affinity by $\sim$4-fold and weakening Cl^- binding, as well as slowing the Cl^--H^+ exchange to $\sim$15% that of the WT protein [208]. Thus, S107 has an important function in determining anionic specificity of the exchange mechanism in CLC transporters. In order to investigate the role of S107 in determining anion selectivity, and to characterize the structural changes upon the introduction of the single point mutation S107P, MD simulations were performed on S107P mutant with Cl^- or NO_3^- bound at S_{cen}, respectively.

4.2 Materials and Methods

4.2.1 Construction of the ClC-ec1 Mutant Model

The crystal structure of ClC-ec1 (PDB ID:1OTS solved at 2.51 Å) [62] was used to construct the mutant ClC-ec1 simulation systems. The wild-type residue Serine 107 was mutated into Proline using the PSFGEN plugin of VMD [161], employing the CHARMM27 topology file for proteins [177, 180, 232]. Two S107P mutant systems were constructed in the presense of bound anions (Cl^- or NO_3^-) to examine the anion binding behavior in ClC-ec1. In every system, all the crystal water molecules in the crystal structure were included, in addition to the internal water molecules placed by DOWSER [210]. To rule out the possibility that the formation of water wires between Glu_{ex} and Glu_{in} is artificially biased by the initial setup, all the water molecules in the central hydrophobic region were removed, except for a water molecule placed between Glu_{ex} and the anion bound at S_{cen}, to stabilize the two negative charges in close proximity as suggested in previous simulation studies [87,211,212]. Glu_{ex} and Glu_{in} were both deprotonated while E113 was protonated according to previous Poison-Boltzmann electrostatic calculations [213]. The protein was embedded into a

POPE lipid bilayer, fully equilibrated TIP3P waters [214] and buffered in 0.15 M NaCl solution. The resulting system, contained in 105 Å × 105 Å × 110 Å simulation box, comprises ∼110,000 atoms.

4.2.2 Simulation Protocols

For each of the two mutant systems, a 5000-step energy minimization was performed, followed by an equilibration for 1 ns, during which the protein atoms and oxygen atoms of the crystallographic water molecules were positionally constrained ($k = 2\,\text{kcal/mol/Å}^2$). Harmonic potentials ($k = 0.1\,\text{kcal/mol/Å}^2$) were also applied on water molecules to keep them out of the membrane. Then 350-400 ns of unrestrained simulations were performed for each system.

4.3 Results and Discussion

4.3.1 S107 Acts as the Central Node of the Selectivity Filter

The key to unveiling the mechanistic detail of the serine-specific Cl^-/H^+ coupling is to characterize the structural elements involved with this residue. Inspection on our prior 400 ns equilibrium simulation of WT ClC-ec1 in the presence of Cl^- revealed that S107 forms multiple hydrogen bonds with several highly conserved residues in close proximity, thus acts as the central node that connects all of the four motifs involved with ion-binding (Fig. 4.1(b) and (c)). To be specific, the amide oxygen atom from S107 is involved in the hydrogen bonding with the amide nitrogen atom from P150 (motif GREGP); the amide nitrogen atom from S107 is involved in the hydrogen bonding with the amide oxygen atom from G354 (motif GIFAP). Moreover, by forming a hydrogen bond with the amide nitrogen atom of G108 (motif GSGIP), the serine hydroxyl group is maintained at a suitable conformation for Cl^- binding and is polarized to interact more strongly with the bound Cl^-. In addition, S107 interacts with Y445 (motif Y) via coordinating the Cl^- ion from opposite sides. Thus, S107 communicates with all of the four functionally important motifs as well as the Cl^- bound at S_{cen}, resulting in a fully compact ion-binding region that is especially fit for Cl^-.

4.3.2 Single Mutation Induced Structural Change

From a physiochemical point of view, serine has a polar lateral chain, while proline is a non-polar amino acid presenting fix ϕ and ψ torsion angles in a protein structure. The S107P mutant simulation in the presence of Cl^- revealed that, due to the peculiar chemical properties of proline, its introduction leads to a backbone rearrangement that could be responsible for the decrease of Cl^- binding affinity as well as the decoupling of H^+ to Cl^-. The serine-proline substitution breaks the hydrogen bonds between residue 107 and P150/G354; and the removal of the hydroxyl side chain eliminates the hydrogen bond with G108 and the coordination with Cl^- and Y445. Such structural changes result in a incompact selectivity filter which underlies the specific features of the single mutation. In order to compensate the lost coordination from S107, the Cl^- ion moves downward to gain the coordinations with the amide nitrogen atoms from G108 and I109 (Fig. 4.2). Such a slight movement increases the distance between the bound Cl^- and the putative H^+ pathway, which could be the reason that no water wire arises during the S107P simulation in the presence of Cl^-.

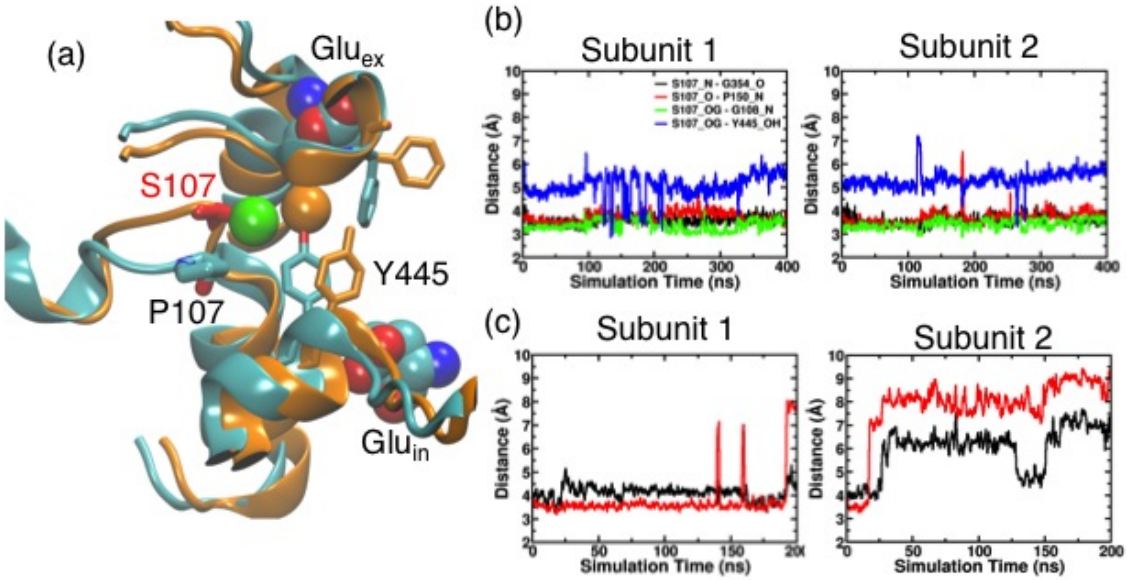

Figure 4.2: The conformational change of the Cl^- binding region induced by S107P mutant. **(a)** Structural comparison between the WT (orange) and S107P mutant indicates the backbone rearrangement of the ion binding region and the displacement of the S_{cen} bound Cl^- upon the single point mutation. **(b)** Hydrogen bonds formed between S107 and the surrounding residues in the WT simulation. **(c)** The serine-proline substitution breaks the hydrogen bonds between residue 107 and P150/G354; and the removal of the hydroxyl side chain eliminates the hydrogen bond with G108 and the coordination with Cl^- and Y445.

4.3.3 NO_3^- is Better Accommodated in S107P Mutant

Our WT simulation revealed that due to the large size, NO_3^- cannot bind as stable as the physiologically transported Cl^-, and exhibits two interchangeable binding configurations during the simulation. Based on structural analysis on the S107P mutant, the absence of hydrogen bonds among the ion-binding motifs moderately looses the selectivity filter, thus creates more space for larger anion to bind at S_{cen}. The simulation indicated that upon the introduction of this single mutation, the comparatively larger polyatomic anion $NO3^-$ can comfortably fit into S_{cen} and is stabilized by the amide nitrogen atoms from G108 and I109, and hydroxyl group of Y445 (Fig. 4.3). NO_3^- binding configuration in the S107P mutant is very similar to that of the Cl^- binding in the WT structure, which is compatible with the fact that S107P greatly favors NO_3^- binding. Moreover, comparison of NO_3^- binding in S107P mutant with WT simulation indicated that the bound NO_3^- steps away from the putative H^+ pathway, which could result in the formation of continuous water wires that are not intervened by NO_3^-.

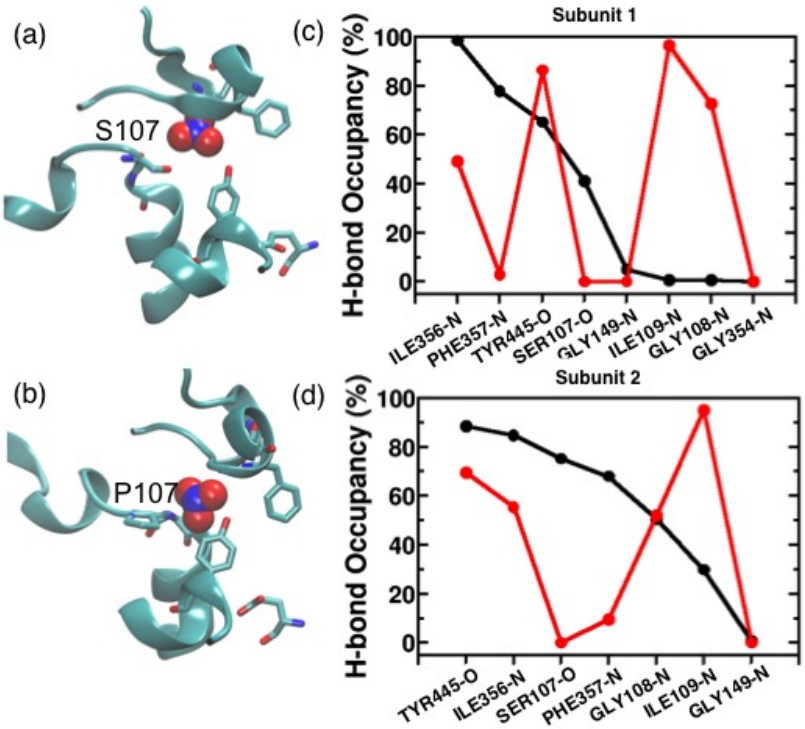

Figure 4.3: Comparison of NO_3^- binding in WT and S107P mutant. **(a)** and **(b)** NO_3^- comfortably fits into S_{cen} due to the comparatively larger space created by S107P. **(c)** and **(d)** Coordination of NO_3^- in WT (black) and S107P mutant (red) are different.

4.4 Summary and Perspective

The mechanism of coupling between stoichiometric transport of H^+ and Cl^- (1:2) in opposite directions across the membrane is the most important mechanistic aspect of CLC function [64, 65]. Both crystal structures and physiological measurements have pinpointed the importance of the intracellular gating residues S107 and Y445 for Cl^-, as well as the H^+ transfer residues E148 (Glu_{ex}) and E203 (Glu_{in}) [70, 233, 234]. However, how the transportation of Cl^- and H^+ ions is coupled remains unclear. Our previous MD simulations have shown that the presence of Cl^- at the S_{cen} site can stabilize the water wires formed between the two H^+ transfer sites Glu_{ex} and Glu_{in} [60], revealing a novel mechanism that accounts for the Cl^-/H^+ coupling. Analysis of water dynamics of short simulations have shown that the occupancy of the S_{cen} site by the other anions ($NO_3^-/SCN^-/F^-$) could significantly perturb formation of water wires. However, the ability of exchange two NO_3^- for one H^+ in plant CLCs [222] and the conversion of the Cl^-/H^+ exchanger ClC-5 into a efficient NO_3^-/H^+ exchanger by a single mutant draw our attention to a specific residue in the S_{cen} site that has the potential to functionally affect the anion selectivity in CLC proteins.

The MD simulation performed in this chapter concludes that S107 plays a key role in determining the structure conformation of the loop containing the motif GSGIP (106-110), which forms part of the S_{cen} site. The conformational change of the loop results in a loose binding site such that the Cl^- ion is free to move around in order to gain coordination from the residues in close proximity. However, without a firmly bound Cl^- at the S_{cen} site, the probability for water wires to arise between Glu_{ex} and Glu_{in} is rare. One possible reason is that the Cl^- ion at the S_{cen} site could play an important electrostatic role in promoting the water wires, as suggested in our earlier study on ClC-ec1 [60]. Another reason could be the arrangement of the dipole orientations of the water molecules occupying the middle part of the water wire, which may also be affected by the negative electrostatic potential created by a stably bound anion at the S_{cen} site [60]. The poor binding of Cl^- at the S_{cen} site and the lower chance of forming water wires between the Glu_{ex} and Glu_{in} in our simulation provides a likely explanation for the experimental data that the S107P mutation in ClC-ec1 greatly weakens the Cl^- binding and slows the H^+ coupling to $\sim$15% that of the WT protein [208].

NO_3^-, as discussed in chapter 3, induces the formation of pseudo water wires that are intervened by NO_3^- itself in ClC-ec1 [3]. This observation provides atomistic details for the experimental data that shows significant reduction of H^+ transport for NO_3^- in ClC-ec1 [55]. However, for plant CLCs which function as NO_3^-:H^+ exchanger, intact water wires (as those seen in the Cl^- bound systems) are expected to allow efficient transport of H^+. Because of the large volume of the polyatomic anion, NO_3^- cannot fit into the S_{cen} site of ClC-ec1 as perfectly as the physiologcially transported anion Cl^-, and thus takes up part of the space in the central hydrophobic region that is occupied by water molecules in the Cl^- bound systems. Upon the loop conformational change, the comparatively larger polyatomic anion NO_3^- can comfortably fit into the S_{cen} site and is well coordinated by surrounding residues. This result is paralleled with the experimental observation that the S107P mutation in ClC-ec1 greatly increased the binding affinity of NO_3^- [208]. Since the loop conformational change took place 10s to 100s of ns after the simulation initiated and the relaxation of the surround environment is also needed, the simulation time is too limited to observe any water wires formed after the loop is reoriented and the NO_3^- finds its binding position and conformation. Even though water wires have not been captured in the 400 ns mutant simulation with NO_3^-, this simulation provides invaluable information on structural details that could potential explain the anionic specificity among CLC proteins, especially before a crystal structure of the ClC-ec1 mutant or the plant CLC homologs is available. Long MD simulation and experimental work will further illuminate the selective coupling between H^+ and anions, and provide more insight on the mechanism of NO_3^-/Cl^- selectivity in CLC proteins.

5 Determine Structural Changes Associated with Steps in the CLC Transport Cycle[1]

5.1 Introduction

From bacteria to humans, Cl^-/H^+ exchange by CLC transporters occurs with a strict stoichiometry of 2 Cl^- for every H^+ [57, 198, 199, 230, 235]. To achieve this stoichiometric exchange, CLCs must follow an alternating access mechanism, in which bound substrate ions access either side of the membrane alternately, i.e., they cannot access both sides simultaneously [6]. The alternating access mechanism can only be realized by coupling of ion binding, translocation, and unbinding events to conformational changes in the transporter protein. Specifically, movement of ions between solution and the ion-binding sites of the transporter, as well as ion movement between binding sites, needs to be coupled to conformational changes between "outward-facing" (in which the external, but not internal, solution is accessible to ions), "occluded" (in which neither solution is accessible), and "inward-facing" (in which the internal, but not external, solution is accessible) states [10].

In all other active transporters that have been structurally (or biophysically) characterized, the conformational changes governing the interconversion between these major functional states involve significant protein motions, including reorientation of helices or even entire domains [236]. For the CLC transporters, in contrast, it has been proposed that the transport mechanism may be fundamentally different and involve only localized side chain motions [96, 237]. However, this proposed mechanism is based largely upon the observation that no large-scale CLC conformational change could be detected crystallographically. The crystal structure of a mutant in which the highly conserved glutamate residue Glu_{ex} is replaced by Gln, has been thought to represent an outward-

[1] The materials presented in this chapter were published in:
Chandra M. Khantwal, Sherwin J. Abraham, Wei Han, **Tao Jiang**, Tanmay S. Chavan, Ricky C. Cheng, Shelley M. Elvington, Corey W. Liu, Irimpan I. Mathews, Richard A. Stein, Hassane S. Mchaourab, Emad Tajkhorshid, Merritt Maduke, "Revealing an outward-facing open conformational state in a CLC Cl^-/H^+ exchange transporter". *eLife*, 5:e11189, 2016 [4].

facing (OF) CLC conformational state (Fig. 5.1). However, in this structure the pathway to the extracellular solution is still too narrow to accommodate Cl^- or other permeant ions [238, 239] - suggesting that additional conformational changes are required for the formation of the OF state in order for external anions to access the S_{ext} site. Therefore, the state identified in the E148Q crystal structure was hypothesized as an "outward-facing occluded" state, and that a distinct "outward-facing open" state may exist to permit access of external Cl^- to the Glu_{ex}-vacated S_{ext} site (Fig. 5.1). Addressing this hypothesis is crucial to understanding the CLC transport mechanism and how it relates to those of canonical transporters.

Various experimental approaches have been used to evaluate whether CLC conformational changes beyond Glu_{ex} are involved in the transition to an OF open state. Since the pKa of Glu_{ex} is $\sim$6 [209], a change in pH from 7.5 to 5.0 will cause Glu_{ex} to transition from mostly deprotonated to mostly protonated, and therefore from its position occupying S_{ext} outward towards the extracellular solution. Such pH manipulations can therefore be used to enrich the OF state and probe for changes in protein conformation. Although crystallization at pH 4.6 failed to reveal any conformational change [61], spectroscopic approaches have shown that H^+-dependent changes do occur outside the restraints of crystallization. Using ^{19}F NMR, our collaborator Maduke's lab showed that the ^{19}F-labeled Y419, a residue located near the dimer interface (Fig. 5.2), reported $[H^+]$-dependent changes in chemical environment. Y419, which is largely buried in the crystallographically captured state of ClC-ec1, became exposed to the bulk solution when pH is changed from 7.5 to 4.5. This H^+-dependent change in accessibility is reversible, when pH is returned to 7.5 from 4.5. They then investigated the functional relevance of the conformational change detected at Y419 by introducing cysteines into this region at residue D417 (Fig. 5.2) and examining the effects of inter-subunit cross-linking. Cross-linking at subunit interface would restrict the conformational changes responsible for the increased solvent accessibility of Y419 at low pH. If these conformational changes are functionally important, cross-linking should also reduce the efficiency of Cl^-/H^+ transport. Consistent with this picture, the Cl^- efflux assay showed that cross-linking at 417C correlates directly with a decrease in transport activity, with Cl^- and H^+ transport inhibited in parallel. Thus, CLCs undergo H^+-dependent conformational changes beyond those revealed by crystallography, and these conformational changes are involved in the transport cycle. The question remains how are these long distance conformational changes regulate ion binding and translocation

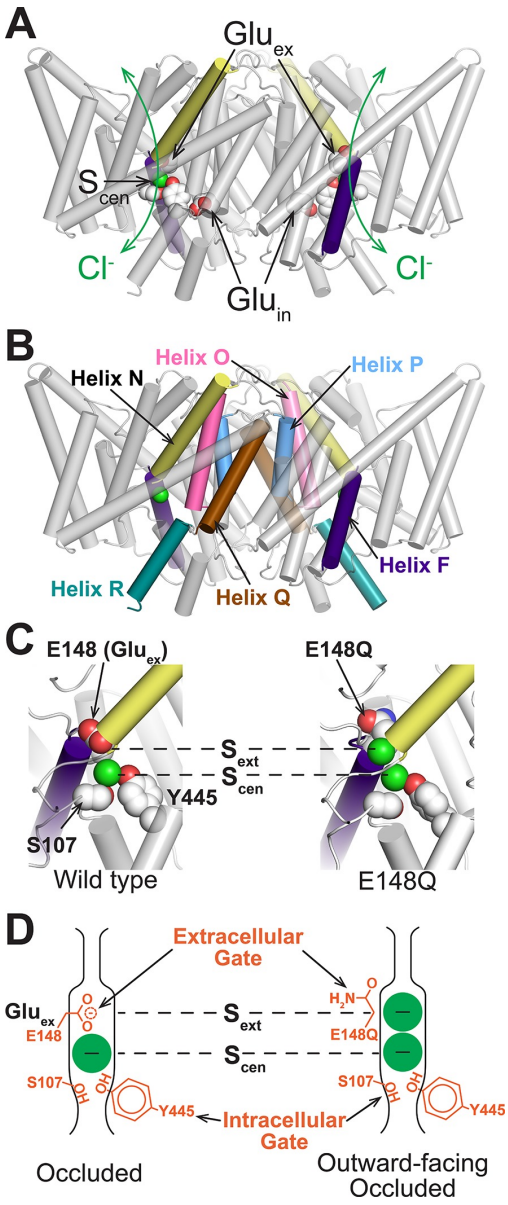

Figure 5.1: Structure of CLC transporters. **(A)** Structure of ClC-ec1 (pdb: 1OTS). The bound Cl^- (one in each identical subunit at site S_{cen}) is coordinated by conserved Ser and Tyr residues (shown as spacefilled). The N-termini of helices F and N (shown in purple and yellow respectively) point towards this site and provide a positive electrostatic environment for the anion. The H^+ permeation pathways are delineated by two key residues, Glu_{ex} and Glu_{in}. Glu_{ex} also acts as a "gate" that blocks the Cl^- permeation pathway (green arrows) from the extracellular solution. **(B)** CLC structure highlighting helices discussed: F (purple), N (yellow), O (pink), P (blue), Q (brown), and R (aquamarine). **(C)** Close up of the Cl^- binding region in WT (left) and E148Q (right) ClC ec1, highlighting intracellular and extracellular gate residues S107, Y445, and E148 (Glu_{ex}). In the E148Q mutant (pdb: 1OTU), the Gln side chain, mimicking the protonated Glu_{ex}, swings away from the Cl^- permeation pathway and is replaced at S_{ext} with a Cl^- ion. The structure of this mutant is otherwise indistinguishable from the WT structure. **(D)** Cartoon of the Cl^- binding region, illustrating the hypothesis that the E148Q structure represents an "outward-facing occluded" rather than an "outward-facing open" conformation.

during Cl^-/H^+ transport.

In addition to the OF states, "channel-like" ClC-ec1 variants can be generated when the outer- and inner-gate residues of ClC-ec1 (Glu_{ex} and Y445 respectively) (Fig. 5.1) are replaced by smaller residues Ala, Ser, or Gly [240]. This excavation of the gates yields a narrow water-filled conduit through the transmembrane domain, which allows rapid Cl^- throughput and abolishes H^+ coupling. Thus, it appears that the mechanism of Cl^- flux through these variants involves channel-like diffusion that is independent of substrate-dependent conformational change. Consistent with this picture, the ^{19}F NMR data showed that E148A/Y445S ClC-ec1 (exhibiting the highest Cl^- permeability among the channel-like variants) does not undergo the substrate-dependent spectral changes observed in the coupled ClC-ec1 transporters [241]. In channel-like E148A/Y445S, the accessibility of Y419 indicates that the channel-like ClC-ec1 variant adopts a conformation in solution different from that observed in the crystal structure and similar to the conformation adopted by WT at low pH. Importantly, to the degree it can be cross-linked, D417C in channel-like ClC-ec1 is inhibited similarly to D417C in WT. Thus, structural changes beyond the rotation of Glu_{ex} is necessary for maximal activity in both transporter and channel-like ClC-ec1.

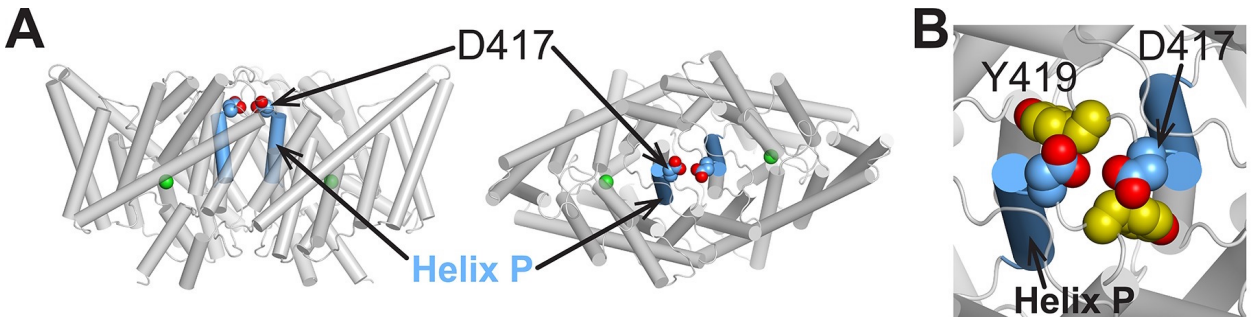

Figure 5.2: Location of Y419 and D417 in ClC-ec1. **(A)** ClC-ec1 with D417 side chain shown spacefilled, viewed from the membrane (left) and from the extracellular side (right). **(B)** Close-up view showing D417 and Y419 side chains.

In this chapter, MD simulations were used to to model how ClC-ec1 changes shape in details. The simulations predict that the extracellular gate region of the transporter undergo major rearrangements, which is correlated to the long distance conformational change near the dimer interface, resulting in a gate-opening motion that widens a passage to allow the Cl^- ions to bind to the protein. These findings will prompt future studies to reveal the other shapes and how CLCs transition between them.

5.2 Materials and Methods

5.2.1 Construction of the Membrane-embedded ClC-ec1 Models

The ClC-ec1 crystal structure at 2.51 Å (PDB ID: 1OTS) [62] was used to prepare for the MD simulations of all the systems studied in the present work - WT, D417C, channel-like (E148A/Y445S), and D417C/channel-like. The system setup for the WT ClC-ec1 is detailed in our previous work [60]. In short, to have the protein hydrated properly, all the crystallographic water molecules were maintained and 49 additional water molecules were added using DOWSER [210]. One additional water molecule was placed between Glu_{ex} (E148) and the Cl^- ion bound at the S_{cen} site of ClC-ec1 in order to stabilize the two closely (within ∼4 Å) positioned negative charges, as suggested in previous simulation studies [87, 211, 212]. Glu_{ex} (E148) and Glu_{in} (E203) were both deprotonated, while E113 was modeled in its protonated form according to previous Poison-Boltzmann electrostatic calculations [213]. The protein was embedded into a POPE lipid bilayer, fully equilibrated TIP3P water [214] and buffered in 150 mM NaCl, resulting in a $105 \times 105 \times 110\,\text{Å}^3$ box with ∼110,000 atoms.

The mutant systems were constructed on the basis of that of the WT. For each mutant, residue substitutions were done using the Mutator plugin of VMD [161]. Disulfide bonds were constructed by introducing geometric restraints on two cysteine residues, including a distance restraint between the sulfur atoms and angular restraints involving C_β atom of either cysteine and the two sulfur atoms. To avoid structural disruption of the protein due to sudden introduction of restraints, the disulfide restraints were turned on gradually over 20-ns simulations. Note that the systems prepared as such are not significantly different from the cross-linked D417C crystal structure. In fact, during the equilibrium simulation of the mutant containing the disulfide bond (see below), the RMSD of the protein to the D417C crystal structure is on average ∼1.6 Å, even smaller than its RMSD (∼1.9 Å) to the WT crystal structure that the simulation started from.

5.2.2 Simulation Protocols

Each system was energy-minimized for 5,000 steps, followed by a 1-ns MD run with positions of all protein atoms and oxygen atoms of the crystallographic water molecules restrained. Each system was simulated without any restraints for ∼300 ns.

5.2.3 Analysis of Collective Motions of Protein

The collective motions of the protein were analyzed through principal component analysis (PCA) of the equilibrium MD trajectories. Specifically, we first constructed the covariance matrix **C** of C_α atoms of select parts of the proteins for each subunit based on equilibrium MD trajectories. The covariance matrix **C** was calculated as $c_{ij} = <(x_{in} - <x_{in}>)(x_{jn} - <x_{jn}>)>$, where $\mathbf{X}_n = x_{in}$ are the coordinates of C_α atoms of select parts of protein in the n^{th} sampled structure and the brackets <> denote the averages over all the sampled structures. The first 50 ns of each MD trajectory were discarded to remove any initial bias. Only the transmembrane helical regions were selected for this analysis as they define the overall architecture of the protein and most relevant to the functionally relevant global motions. We then derived orthonormal eigenvectors $\mathbf{R}=\mathbf{R}_k$ of the covariance matrix **C**. Each eigenvector $\mathbf{R}_k=\mathbf{r}_{ik}$ defines relative movement ($\mathbf{r}_{ik}$) of each select atom in a collective motion of the protein represented by the eigenvector. The 20 eigenvectors with the largest eigenvalues were chosen for further analysis. These eigenvectors correspond to the collective motions that account for >75% of protein motion observed in the simulations.

Following the approach by Bahar and co-workers [242], conformational deformation driven by a given collective motion can be calculated according to the associated eigenvector $\mathbf{R}_k$ as follows:

$$X' = X_0 \pm AR_k$$

where$\mathbf{X}_0$ and **X'** denote the coordinates of the reference structure and the structure of the protein deformed by the collective motion, and A is an arbitrary scaling factor determining the extent of structural deformation to be examined. The value of A is related to the RMSD between the reference and the deformed structures through the relationship RMSD = $A/M^{1/2}$, where M is the

number of atoms selected to calculate RMSD (here M=538, the number of C_α atoms located in the transmembrane helical region of the protein). To make a meaningful comparison of all collective motions investigated, the value of A was chosen such that the structure of the protein is altered by each motion to the same extent, targeting always a total RMSD of 3.5 Å with respect to the original structure. Thus, the distance change (Δr) between two sites ($\mathbf{x}_i$ and $\mathbf{x}_j$) of interest (Fig. 5.4B) can be calculated according to

$$\Delta r = \left| x_i' - x_j' \right| - |x_i - x_j|$$

Finally, we quantified the protein's ability of opening its gates via collective motions by counting the dominant collective motions that involved an increase in the distance between residues lining the gates by $\Delta r > 1.5$ Å. To achieve a statistical estimate of such counts, each 300-ns simulation trajectory of the homodimer was divided evenly into three time blocks [243], each being analyzed through the procedure described above, providing a dataset of six segments (three time blocks for each subunit x 2 subunits). Statistical comparisons between datasets were made using the Wilcoxon-Mann-Whitney test [244].

5.3 Results and Discussion

5.3.1 Helix P Cross-link Specifically Affects the Cl^- Permeation Pathway

The results with channel-like and uncoupled transporters support the conclusion that the D417C cross-link inhibits the Cl^- branch of the Cl^-/H^+ transport mechanism but do not rule out an effect on H^+ transport. As an approach to examine the effect of the cross-link on H^+ transport, MD simulations were used to examine water entry into the hydrophobic region between Glu_{in} and Glu_{ex}, which is essential to connect these two major H^+-binding sites and thus support H^+ transport [60, 86, 245–247]. Water entry occurs via a narrow portal on the cytoplasmic side of the protein, lined by Glu_{in} together with E202 and A404 [60, 247]. Constricting this portal by introducing large side chains at position 404 inhibits water entry detected computationally and H^+ transport detected experimentally [60]. Since A404 is on the intracellular end of Helix P (Fig. 5.3A), restricting movement of this helix via the D417C cross-link might restrict water entry.

To determine whether the D417C cross-link affects water entry, the number of water molecules entering the central hydrophobic region during the simulation of cross-linked D417C was compared to the WT simulation. In contrast to the A404L mutation, which greatly reduces water permeation through the portal [60], the D417C cross-link has no effect on water entry (Fig. 5.3B). This result suggests that the cross-link reduces ClC-ec1 transport predominantly via an effect on the Cl^- permeation pathway rather than on the H^+ permeation pathway.

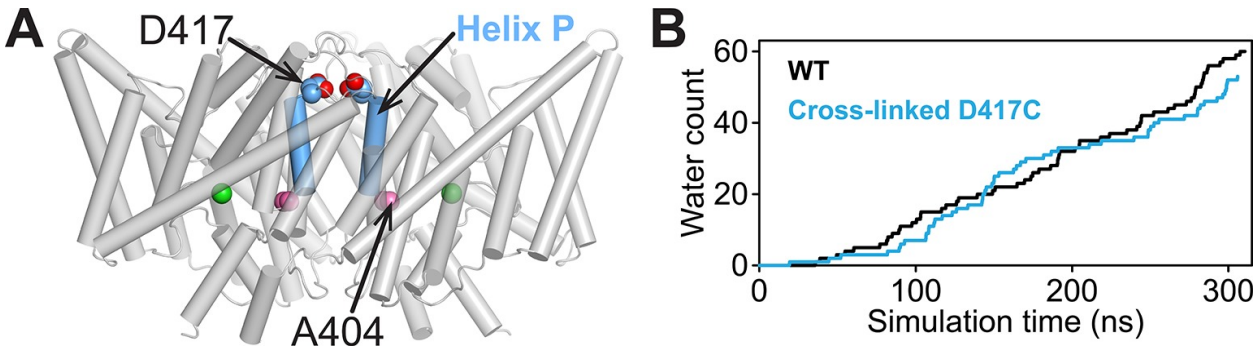

Figure 5.3: Computational analysis of water entry through the portal lined by A404 (Helix P). **(A)** ClC-ec1 structure highlighting the location of the A404 "portal" residue at Helix P. **(B)** The D417C cross-link does not affect water entry into the pathway connecting Glu_{in} and Glu_{ex}. The aggregate number of water molecules entering the region between the two residues was determined as described previously [60] and compared for wild-type (WT) and cross-linked mutant (D417C) over the same timescales.

5.3.2 Potential Gate-opening Motions in WT and Cross-linked ClC-ec1

Experimental results suggested that there could be functionally important motions of ClC-ec1 that open the Cl^- transport pathway and are impeded by the D417C cross-link. To investigate the molecular basis of such motions, extensive MD simulations were conducted either in the absence or in the presence of the D417C cross-link. Note that even the hundreds of nanoseconds of simulations performed here can probe mainly conformational fluctuations of ClC-ec1 near its reference conformation (in this case, the crystal structure), which did not permit direct observation of the opening of the gates. Nevertheless, the sampled dynamics and fluctuations can provide information that can be used to derive collective motions, which are often functionally relevant [248]. Collective motions are defined as those involving concerted movements of a large number of atoms distributed throughout the protein, and are therefore distinguished from localized conformational changes. A series of collective motions of a protein can be obtained in general by decomposing the fluctua-

tions of a protein sampled through MD simulations, e.g., through principal component analysis, or by analyzing normal modes of the protein that underlie protein motions [248, 249]. Collective motions can further be used to probe how larger-magnitude conformational change along the identified displacement vectors (modes) might involve crucial, functionally-relevant protein motions, such as opening-closing movements of enzymatic active sites, ligand-binding sites on receptors and channel pores. For example, collective motions obtained from normal mode analysis (NMA) were used to project opening movements of potassium-channel pores, and these predicted movements are consistent with those seen in single-molecule and X-ray crystallographic experiments.

In this study, collective motions in ClC-ec1 were identified using principal component analysis (PCA) of the equilibrium MD simulations (see Methods), which in general identifies similar collective motions to those derived from NMA. Deformations in the reference protein structure were the introduced along each of the top 20 collective motions identified in PCA analysis (75% of the motions observed in the equilibrium MD simulation). Amplitude of these collective motions (which overcomes timescale limitations of the simulation) was then increased to see whehter they confer conformational change to the Cl^- transport pathway. Regions around the extracellular and intracellular gates to the Cl^- transport pathway was then examined, since motions near these region may lead to opening of either gate (which are both closed in the reference protein structure).

The extracellular gate is formed by the juxtaposition of Helix F (which contains Glu_{ex}) and Helix N (Fig. 5.1B). To scrutinize opening of this gate, C_α distance changes (Δr) between several residue pairs on these helices were examined: I356-G149, F357-E148, and A358-R147 (Fig. 5.4A and B). A search over the 20 dominant collective motions obtained through the PCA of the entire WT MD simulation revealed that deformations along some of the collective motions increase the distances between these pairs by >1.5 Å and thus are coupled to gate opening. To conduct a statistical analysis of these motions, the entire simulation trajectory was devided into six blocks and the number of times such collective motions occur in each block was determined (Fig. 5.3C, blue bars). An identical analysis performed on the MD simulation trajectory obtained from the cross-linked D417C mutant revealed that the motions that open the extracellular gate are dampened due to the cross-linking ($P = 0.002 - 0.008$) (Fig. 5.3C, orange bars). The intracellular gate is formed by two key residues S107 and Y445 [207, 250, 251] (Fig. 5.1). To scrutinize opening of this

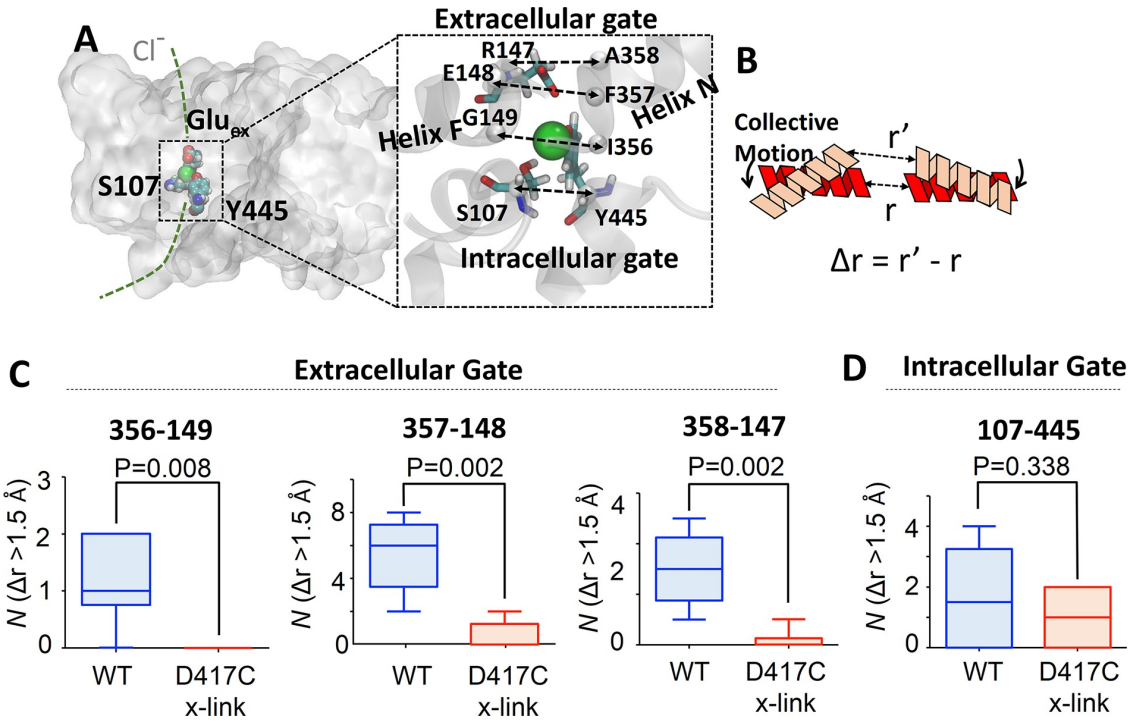

Figure 5.4: Coupling of extracellular and intracellular gating motions to collective motions in ClC-ec1 detected computationally. **(A)** Key inter-C_α distances were employed to detect functional motions. The left panel shows the location of the Cl^- gates (dashed box) and transport pathways (dashed green line) in ClC-ec1. Right panel shows a close-up of the Cl^- gates where key inter-C_α distances for both the extracellular and intracellular gates are denoted by dashed double arrows. **(B)** Scheme for determining distance change (Δr) caused by a collective motion. Following a collective motion, a native structure (red helices) undergoes structural transition (peach helices). As a result, the distance between the helices increases by $\Delta r = r' - r$. **(C)** Opening motions of the extracellular gate. The number (N) of collective motions that lead to distance changes ($\Delta r > 1.5$ Å) at each of the extracellular-gate residue pairs was determined from analysis of MD simulations for WT and cross-linked ("D417C x-link") ClC-ec1, as described in the text. The data are shown in a box-and-whisker plot where the whiskers denote minimum and maximum of the data and the box denotes the range of 25th percentile to 75th percentile of the data when sorted. The horizontal line in the box denotes the median of the data. **(D)** The number (N) of collective motions that lead to distance changes ($\Delta r > 1.5$ Å) at the intracellular gate pair 107-445 is not significantly different between WT and cross-linked ClC-ec1.

intracellular gate, distance changes between these two residues as a result of collective motions were examined. As with the extracellular gate, some collective motions that lead to distance changes (Δr) of >1.5 Å were observed. Unlike the extracellular gate, however, the cross-link at residue 417 does not significantly dampen the distance changes around the intracellular gate ($P = 0.338$) (Fig. 5.4D).

5.3.3 Collective Motions in Channel-like ClC-ec1

The comparison of dominant gate-opening motions between WT and cross-linked forms described above suggests that the cross-link at residue 417 likely cripples the opening of the extracellular gate, thereby slowing Cl^- transport. However, along this line of reasoning, one must reconcile why the E148A mutants, in which the extracellular gate has ostensibly been removed, are inhibited when the cross-link is introduced. To address this question, the bottleneck for Cl^- transport in ClC-ec1 was investigated based on the crystal structures. The radius profile of the ClC-ec1 Cl^- transport tunnel, calculated using the program HOLE [215], shows an extracellular bottleneck with a minimum radius of ∼0.2 Å (Fig. 5.5). Interestingly, the calculated radius profile for both the E148A mutant (lacking Glu_{ex}) and the channel-like variant E148A/Y445A also reveal extracellular bottlenecks. (E148A/Y445A was evaluated rather than the E148A/Y445S construct used here because this is the only channel-like variant for which there is a crystal structure.) With minimum radii of ∼0.9 Å (Fig. 5.5) these bottlenecks are still too narrow to allow Cl^- permeation (r(Cl^-) ≈ 1.81 Å). Thus, additional opening motions in the gate region are needed for Cl^- transport.

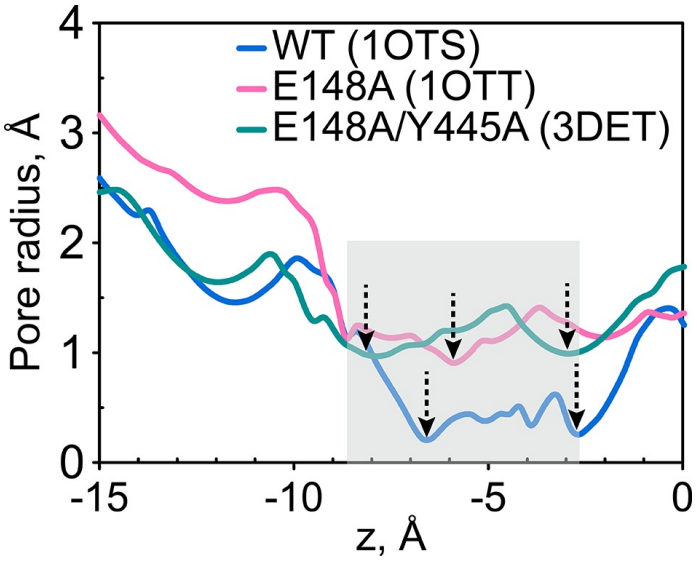

Figure 5.5: The extracellular gate remains narrow in the Gluex mutant (E148A) and in the channel-like variant E148A/Y445A. The pore radius profiles of the ClC-ec1 Cl^- transport tunnel for WT ClC-ec1 (blue), E148A (pink) and E148A/Y445A (green) along the z-axis (membrane normal). Shown are the profiles for subunit 1. The results for subunit 2 are very similar and thus not shown. The z-position of the central Cl^- binding site is chosen as the origin of the z-axis. The shaded region denotes the extracellular-gate region; dashed arrows highlight the z-positions of the bottlenecks.

To test the idea that additional gate-opening motions occur in the absence of Glu_{ex}, the computational analysis discussed above was applied to characterize and analyze the collective motions of channel-like ClC-ec1. The analysis revealed that there are fewer collective motions that can open the extracellular gate after the cross-link is introduced to the channel-like mutant ($P = 0.001--0.070$) (Fig. 5.6A), whereas the intracellular gate was not significantly affected ($P = 0.354$) (Fig. 5.6B). This result is consistent with that obtained in the WT background. Taken together, MD results suggest that the cross-link at residue 417 hinders the opening of the extracellular gate - beyond the Glu_{ex} motions - in both the WT and channel-like ClC-ec1.

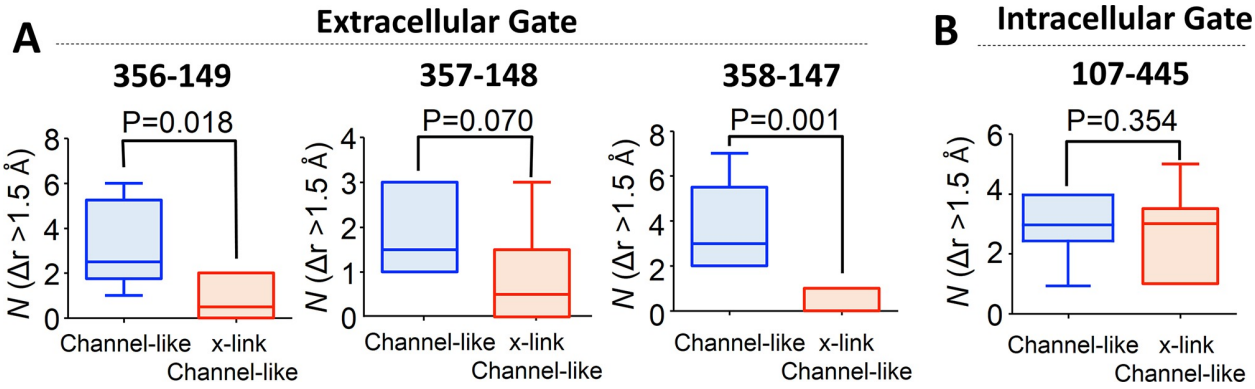

Figure 5.6: Cross-linking at 417 impedes opening of the extracellular but not the intracellular gate in channel-like ClC-ec1, as detected by computational analysis. **(A)** Opening motions of the extracellular gate. The number (N) of collective motions that lead to distance changes ($\Delta r > 1.5$ Å) at each of the extracellular-gate residue pairs was determined from analysis of MD simulations for WT and cross-linked ("x-link") channel-like ClC-ec1, as described in the text. The data are shown in a box-and-whisker plot where the whiskers denote minimum and maximum of the data and the box denotes the range of 25th percentile to 75th percentile of the data when sorted. The horizontal line in the box denotes the median of the data. **(B)** The number (N) of collective motions that lead to distance changes ($\Delta r > 1.5$ Å) at the intracellular gate pair 107-445 is not significantly different between WT and cross-linked channel-like ClC-ec1.

5.4 Summary and Perspective

This work described a previously unidentified protein conformational state and suggest a new framework for understanding the CLC transport mechanism, introducing two key concepts. First, the structure of the E148Q mutant, with the side chain rotated away from S_{ext} (Fig. 5.1C) represents an "outward-facing occluded" ($OF_{occluded}$) state, in which bound Cl^- does not have full access to the extracellular solution. Second, H^+ binding promotes an "outward-facing open" (OF_{open}) state, involving conformational rearrangement of Helices N and P, that widens the extracellular ion

permeation pathway in comparison to the known crystal structures.

Inter-subunit cross-linking of D417C restricts the conformational transition to the OF_{open} state and inhibits activity. The inhibition occurs not only in the WT background but also in uncoupled E148A, Y445S, and E148A/Y445S (channel-like) backgrounds (Fig. 5.4 and 5.6). Therefore, the conformational change being restricted is something other than the localized movements of side-chain gates, as these gates (E148 and Y445) are missing altogether in the uncoupled transporters. To gain insight into how conformational change near the subunit interface affects activity, MD simulations were performed on WT and channel-like ClC-ec1, with and without the D417C crosslink. Simulations revealed that the major motions of both WT and channel-like involve opening of the extracellular vestibule and that these opening motions are dampened by the cross-link at D417 (Fig. 5.4 and Fig. 5.6).

The long-range conformational change described in this chapter improves our understanding of CLC mechanisms by providing a first glimpse of an "outward-facing open" CLC conformational state and its mechanistic implications. In future studies, it will be important to investigate the transition between the OF_{open}, $OF_{occluded}$ and inward-facing conformational state(s). Understanding these interactions will be critical to providing a molecularly detailed view of the CLC transport mechanism.

6 Characterizing the Lipid Translocation and Ion Conduction Pathway in nhTMEM16[1]

6.1 Introduction

Phospholipids distribute asymmetrically between the two leaflets of plasma membranes in quiescent cells. Dissipation of lipid asymmetry in response to the elevation of cytoplasmic Ca^{2+} concentration is a ubiquitous cell signaling mechanism for many critical cellular events, including cell activation, apoptosis, and blood coagulation [117–124, 252, 252]. Regulated transbilayer redistribution (scrambling) of phospholipids requires lipid transporters, namely, phospholipid scramblases, which harvest the energy in the phospholipid gradient to drive the nonspecific and bidirectional transport of phospholipids [116, 252]. The machineries that are known to be responsible for the Ca^{2+}-activated lipid scrambling are belong to the anoctamin/TMEM16 superfamily [117,122,124]. Among the ten mammalian TMEM16 homologs, TMEM16A and TMEM16B are Ca^{2+}-activated Cl^- channels (CaCC), and TMEM16C, D, F, G, and J were identified as Ca^{2+}-activated phospholipid scramblases, some of them also mediate nonselective ion transport. With a commonly shared architecture and mode of Ca^{2+} activation throughout the family [131–133], identification of the corresponding ion and lipid pathways is necessitated to reveal the molecular basis for the mechanism of functions and to understand how the functional diversity is accommmodated by these closely related proteins.

As the first and only lipid scramblase with structure determined, the fungal nhTMEM16 [134, 253] became the most important target for structural and functional investigation of TMEMs. The Xray structure of nhTMEM16 revealed a rhombus-like structure of a homodimer, with ten transmembrane helices resolved in each subunit. The arrangement of the membrane-spanning helices is noval compared to known membrane protein structures; some of them are tilted with respect to the membrane plan, exposing charged and polar residues on the surface of the protein

[1]The materials presented in this chapter are in the manuscript submitted by **Tao Jiang**, Kuai Yu, H. Criss Hartzell, and Emad Tajkhorshid.

within the membrane-embedded part. The most intriguing feature of the structure is a $\sim$10 Å wide hydrophilic aqueduct located on the surface of each subunit away from the dimer interface. The aqueduct is formed by transmembrane helices (TM) 3-7 of the same subuint, with the borders lined by TM 4 and TM6. This aqueduct is twisted along the z-axis as it extends through the membrane, the lining helices TM4 and TM6 are arranged in a crisscross pattern, which results in a relatively narrow and deep bottleneck region near the center of the membrane, and two wide entrances open to each side of the membrane. This membrane-exposed crevice also harbours a highly conserved Ca^{2+}-binding site for two Ca^{2+} ions, mutations of the equivalent coordinating residues affect both the ion conduction and lipid scrambling activities in the family.

Although the membrane-exposed aqueduct on the static structure of nhTMEM16 provides insight into the potential site of catalysis, there were no lipophilic molecules resolved in the crystal structure. It is also puzzling how the aqueduct might provide the aqueous environment required for ion conduction, since it is exposed to the hydrophobic core of the membrane. To elucidate the structural and mechanistic features of the scramblase and to advance the understanding of the molecular basis of the mechanism of regulation by Ca^{2+}, detailed atomisitic information of the dynamic interactions between the scramblase and its lipid environment is needed. Here, through a combined computational and exprimental approach, we have addressed the physiologically most important aspects of TMEMs by identifying and characterzing the transport pathways for phospholipids and ions, and revealing the role of Ca^{2+} for active functions. Especially, the simulations revealed that ions permeate across the membrane through the same structural path that taken by the phospholipid, assisted by both the residues forming the aqueduct and the lipid headgroups occupying the aqueduct. Furthermore, simulation-guided mutational analysis successfully pinpoint the residues that are capable to switch on and off the scrambling activities of the TMEM proteins through single mutation, thus provding fundamental insight into the evolutionary relationship of the TMEM family members.

6.2 Materials and Methods

6.2.1 Preparation of the Simulation Model

The X-ray crystallographic structure of fungal nhTMEM16 (4WIT) at 3.4 Å resolution [134] was used as the starting structure for the simulations. The missing loop regions (residue 1-18, 130-140, 465-482, 586-593, 657-659, 685-691 and 720-735) are located in the intracelluar and extracellular bulk, thus likely will not directly affect the catalytic center embedded in the membrane. The missing loops were added using SuperLooper [160], which provides loop templates from known membrane protein structures or water soluble globular protein structures to effectively fill in the gaps and complete the protein structure with spatial conformation of the loops. The pKa of each and every ionizable residue was estimated using PROPKA [163, 254], and the default protonation states were used based on the pKa analysis. The missing hydrogen atoms were added using PSFGEN in VMD [161]. The program DOWSER [210] was used to locate 109 internal water molecules in energetically favorable positions within the protein, two of them were placed in the hydrophilic aqueduct in each subunit, coordinating the polar side chains of Gln374, Asn378 and Arg505. The two Ca^{2+} ions bound to the two subunits were perserved for the simulation of the Ca^{2+}-activated system, and removed for the simulation of the Ca^{2+}-free system.

The protein was embedded into an asymmetric lipid bilayer that was generated using CHARMM-GUI membrane builder [168]. The outer leaflet is composed by pure POPC, while the inner leaflet is a 2:1 POPC/POPS mixture, as a representation of eukaryotic membranes, where PS is preferentially located in the inner leaflet. This mixed lipid composition was also designed to allow us to investigate the lipid specificity of the scramblase. The membrane/protein system was then fully solvated with TIP3P water [214] and buffered in 0.15 M NaCl to keep the system neutral. The resulting systems (Ca^{2+}-activated and Ca^{2+}-free), consisting of ∼360,000 atoms, was contained in a $204 \times 162 \times 130$ Å^3 simulation box.

6.2.2 Simulation Protocols

The simulation systems (Ca^{2+}-activated and Ca^{2+}-free) were first optimized for 10000 steps, followed by two 1 ns equilibrations, during which the heavy atoms and the backbone atoms from the crystalized protein structure were positionally restrained ($k = 2\,\mathrm{kcal/mol/\AA^2}$), respectively, to allow the added loops to be fully relaxed. Then 1000 ns unrestrained equilibrium simulation was performed for each system.

To investigate the ionic permeation in nhTMEM16, an additional set of simulations were extended from the fully equilibrated Ca^{2+}-activated simulation with different levels of voltage across the membrane induced by external electric fields. The electric field E was applied perpendicular to the membrane plane in the negative z direction (from the extracellular side to the intracellular side), and the total potential drop across the system is calculated by E^*L_z, where $L_z \approx 133.33\,\mathrm{nm}$ is the size of the simulation box in the direction parallel to the applied field. Four simulations with the electric fields of intensity E = 0.011, 0.018, and 0.037 V/nm were carried out, resulting in membrane potentials of ∼0.15, 0.25, and 0.5 V across the system, respectively. Each of the three systems was performed for 700 ns, during which the ion conductivity across the membrane was examined.

6.2.3 Analysis of Protein Surface Hydrophobicity

The overall structural organization of most transmembrane proteins has a very distinct hydrophobic belt region that is in direct contact with the membrane interior. Interestingly, in the case of nhTMEM16 structure, charged and polar residues are observed to expose on the surface of the protein within the membrane-embedded part. Those residues are mainly located near the extracellular and intracellular mouths of the hydrophilic aqueduct, which form hydrophilic areas that are ∼25% deep into the membrane from both sides. Each and every exposed residue was assigned the corresponding hydrophobicity value, according to the hydrophobicity scale of Kyte and Doolittle (Cyan = hydrophilic (-4.5), Orange = hydrophobic (4.5)) (Fig. 1.5).

6.2.4 Analysis of Membrane Structure

The midplane of the membrane is set as the xy-plane (z = 0 Å). The phosphorus atoms from the outer and inner leaflets of the bilayer were initially loacted at ∼18 and −18 Å, respectively. To characterize the protein-induced membrane deformation, the location of PO_4 in proximity of the protein was analyzed using Volmap embedded in VMD. A cutoff of 10 Å within the protein was used to select the shell of lipids that are directly affected by protein-lipid interaction. The occupancy of PO_4 was averaged over the trajectory in order to get the density during the Ca^{2+}-activated simulation.

6.2.5 Analysis of Hydration of the Aqueduct

In order to investigate the influence of hydration on the behavior of lipids within the aqueduct, we monitored the number of water molecules within the aqueduct, as well as the number of headgroup heavy atoms and fatty acid tail carbon atoms during the simulations. To count water molecules in the lipid translocation aqueduct, a cylindrical region of 13 Å radius was defined for each subunit across the membrane. For each cylinder, the central axis is parallel to the membrane normal (z axis), passing through the geometric center of the transmembrane helices that form the wall of the aqueduct (TM4-7 and the C-terminal half of TM3). The cylinder was then divided into 2 Å-thick slabs. Water molecules inside the cylindrical region were binned into corresponding slabs based on the coordinates of the oxygen atom of each water molecule.

6.2.6 Tracing Lipid Headgroups Inside the Aqueduct

To trace the movement of lipid headgroups along the lipid translocation aqueduct, the same cylindrical region as defined in the previous section was used to identify lipid headgroups that penetrate into the aqueduct. The positions (z-coordinate) of the phosphorus atoms of these lipid headgroups were traced during the simulation for both subunits. If a phosphorus atom of the lipid headgroup enters the aqueduct from one leaflet and leaves the aqueduct from the other end, the lipid is considered as being fully scrambled by the scramblase.

6.2.7 Analysis of Headgroups Binding

To characterize the binding of lipid headgroups along the aqueduct, the occupancy map of the phosphate groups over the trajectories were calculated using Volmap embedded in VMD. Three most visited sites within the aqueduct are identified by contouring the volumetric map of PO_4 occupancy at isovalue 0.15, namely, "internal site (S_{int})", "central site (S_{cen})", and "external site (S_{ext})", respectively. To determine the residues that contribute to the binding of the phosphate groups at those sites, contact number between phosphate groups and protein heavy atoms was calculated for each frame of the trajectory, using a distance cutoff of 3.0 Å. The averaged contact number between each residue and the phosphate groups quantitatively describe the intense and frequency of the interaction.

6.3 Results and Discussion

6.3.1 Lipid Bilayer Deformation Induced by the Scramblase

Most transmembrane proteins have a very distinct hydrophobic belt region that is in direct contact with the membrane interior. However, analysis of the surface hydrophobicity of nhTMEM16 revealed a significant dislocation of the hydrophobic belt near the aqueduct that distorts the membrane and primes phospholipid scrambling mechanism. The hydrophobic belts on the left (TM4) and right (TM6) sides of the aqueduct are shifted into the extracellular and intracellular solutions by ∼9 Å. This distinct structural feature causes a membrane distortion immediately after the Ca^{2+}-activated simulation starts, due to the tendency of the surrounding lipids to match the hydrophobic surface of the protein. The PO_4 density of the shell of lipids that are directly affected by protein-lipid interaction indicates that the lipid bilayers on the left and right side of the aqueduct were shifted up and down (Fig. 1(A)), respectively, resulting in a unique staggered membrane structure that greatly reduces the membrane thickness near the aqueduct. To quantitatively describe the deformation of the membrane structure, the number of phosphorus atoms within the 10 Å shell of the protein that spontaneously penetrate the 25 Å- and 20 Å-thick core regions of the membrane

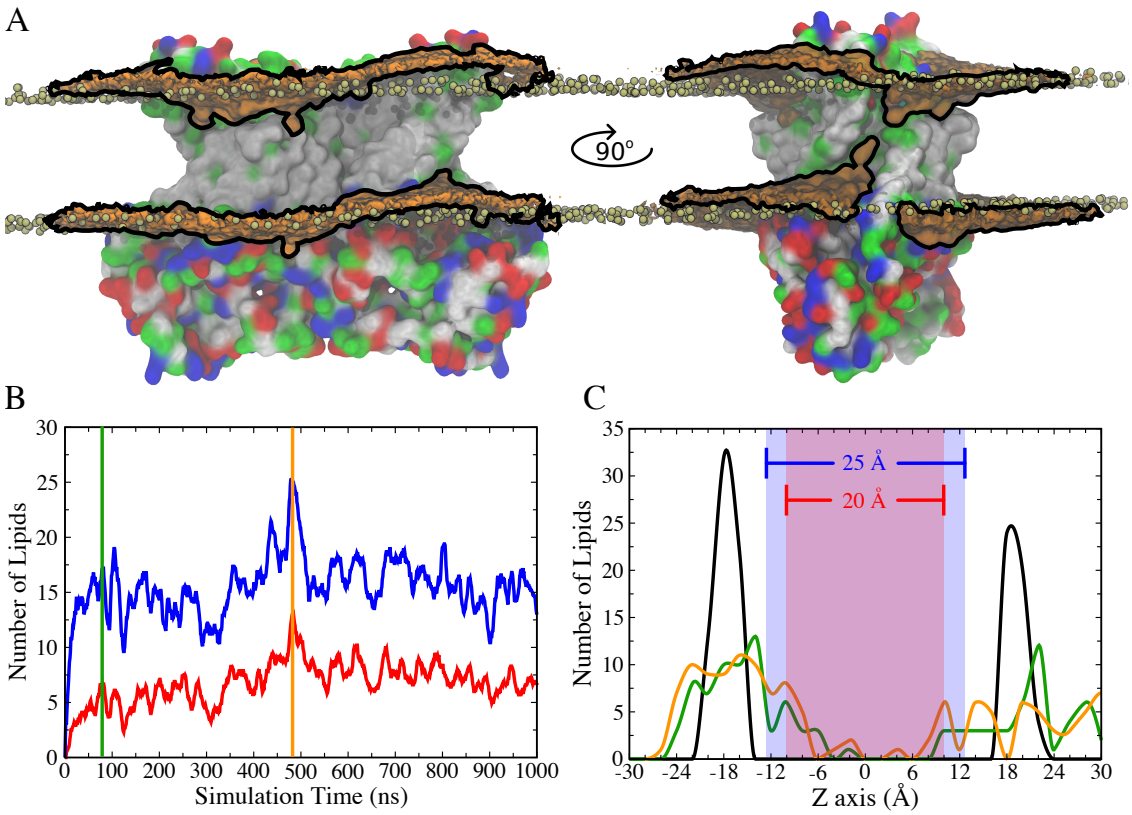

Figure 6.1: Membrane deformation triggered by nhTMEM16. **(A)** The nhTMEM16 protein is shown as a molecular surface (extracellular side on top) and colored by residue type (blue, basic; red, acidic; green, polar; grey, nonpolar) embedded in a phospholipid bilayer composed of PC and PS. The initial ($t = 0$) distribution of phospholipids is represented by the tan phosphorus atoms of the phospholipid phosphate groups. At the end of a 1000 ns MD simulation, the average phospholipid PO_4 density within 10 Å of the protein during the Ca^{2+}- activated simulation is shown as an orange surface outlined by black lines that is contoured at 7.5% of the bulk PO_4 density. **(B)** Deformation of the membrane structure during the simulation, measured as the number of phosphorus atoms within 10 Å of the protein that enter the 25 Å- (blue curve) or 20 Å- (red curve) thick core region of the membrane, as defined by the blue and red areas in panel (C). **(C)** Distribution of phosphorus atoms perpendicular to the membrane (z axis) at 0 ns (black curve), 80 ns (green curve, corresponding to vertical green bar in B), and 480 ns (orange curve, corresponding to vertical orange bar in B) extracted from panel (B).

was counted over the simulation trajectory (Fig. 6.1(B)). The distribution of the P-midplane distances (the distances between the phosphorus atoms and the midplane (z = 0 Å) of the membrane bilayer), in particular, the upper and lower bounds of the distribution curve represent the degree of membrane deformation (Fig. 6.1(C)). At the starting point, the shape of the distribution curve was clearly separated into two main peaks for the inner and outer leaflets, reflecting the flat membrane structure. As the simulation continues, the P-midplane distances became more distributed, resulting in a more flattened distribution curve for both leaflets. The wide-spread and flattened

curve indicates that the membrane structure near the protein was disrupted. Since the lipids in close proximity of the aqueduct are mobile and in continuous contact with the bulk membrane bilayer, the local membrane curvature may serve as an important mechanism priming the lipid translocation.

6.3.2 The Lipid Translocation Pathway

To gain a comprehensive understanding of lipid-protein interaction, we first characterized the behavior of lipids in the immediate proximity of the aqueduct. Intriguingly, spontaneous penetration of lipid headgroups into the membrane interior along the hydrophilic aqueduct was observed in both subunits of the Ca^{2+}-activated simulation, resulting in a continuous file of lipids connecting the outer and inner leaflets (Fig. 6.2(A) middle and right panels). The aqueduct in each subunit can accommodate up to six phosphate groups in its 20 Å-thick core region (Fig. 6.2(A) and (B)), and at least four phosphate groups were present for 51.5% (subunit I) or 28.0% (subunit II) of the simulation time during the last 500 ns (Fig. 2(C)).

Although the distances between the neighboring lipid phosphate groups fluctuate during the simulation, three most visited sites within the aqueduct are identified by calculating the density of the phosphate groups over the whole trajectory (Fig. 6.4(A) left panel). According to their spatial locations along the aqueduct, the three most visited sites are named as "internal site (S_{int})", "central site (S_{cen})", and "external site (S_{ext})". By observing lipid dynamics along the aqueduct during the simulation, we obtained key insights into the mechanisms of phospholipid scrambling. As shown in Fig. 6.3(A), lipid headgroups from the inner and outer leaflets spontaneously bound to the S_{int} ($\sim$-10 Å) and Sext ($\sim$10 Å) sites located near the aqueduct entrances, before they migrated along the aqueduct and propagated toward the center of the membrane. The headgroup at the Scen site ($\sim$-3 Å) was isolated from both leaflets by S_{int} and S_{ext}, and it usually dwelled there for an extended time (Fig. 6.3(A)). Transition of a lipid headgroup from S_{cen} to S_{ext} was captured in subunit II, during which the headgroup at S_{ext} was knocked away from the binding site and quickly merged into the outer leaflet (Fig. 6.3(A) right panel, cyan curve). Immediately after the transition to S_{ext} was completed, the next lipid following in the queue quickly jumped from the S_{int} site to occupy the S_{cen} site (Fig. 6.3(A) right panel, red and dark green curves). This observation indicates that

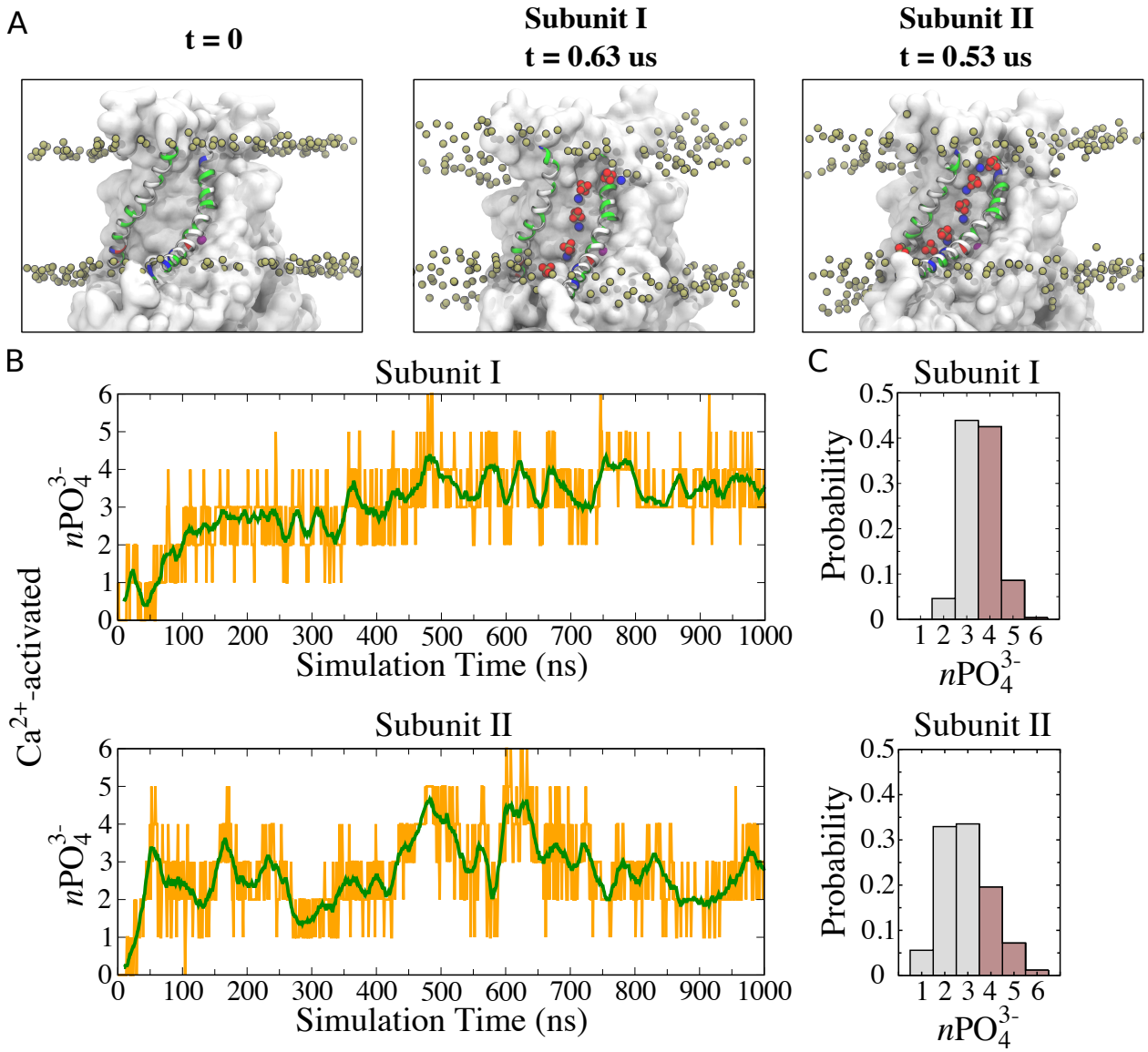

Figure 6.2: Features of the "Lipid aqueduct" on nhTMEM16 surface. **(A)** Representative snapshots of the lipid aqueduct with the aqueduct-lining helices TM4 and TM6 colored by residue type. The phospholipid head groups are shown by the tan phosphorus atoms. The aqueduct is devoid of phospholipid head groups at $t = 0$ (left panel), but aqueducts in both subunits (middle and right panels) become fully occupied by lipid headgroups during the simulation of the Ca^{2+}-activated system. Lipid headgroups inside the aqueduct are shown as phosphate groups and nitrogen atoms with van der Waals radii (oxygen atoms are colored red, phosphorus tan and nitrogen blue). Ca^{2+} ions are purple spheres. **(B)** Number of phosphate groups (orange curve) within the 20 Å-thick core region of the aqueduct of each subunit for the Ca Å-activated simulation. The green curve shows the moving average ($bin = 20$) overlaid. **(C)** Normalized probability histograms of the phosphate count in the 20 Å-thick core region of each aqueduct during the last 500 ns. Numbers larger than three are highlighted in brown.

lipids move along the aqueduct in a highly concerted fashion. Notably, the lipid translocated from the S_{cen} site eventually diffused away from the track and merged into the outer leaflet, after binding at the S_{ext} site for a few hundred nanoseconds, yielding a full permeation of a lipid from the inner leaflet to the outer leaflet under equilibrium condition.

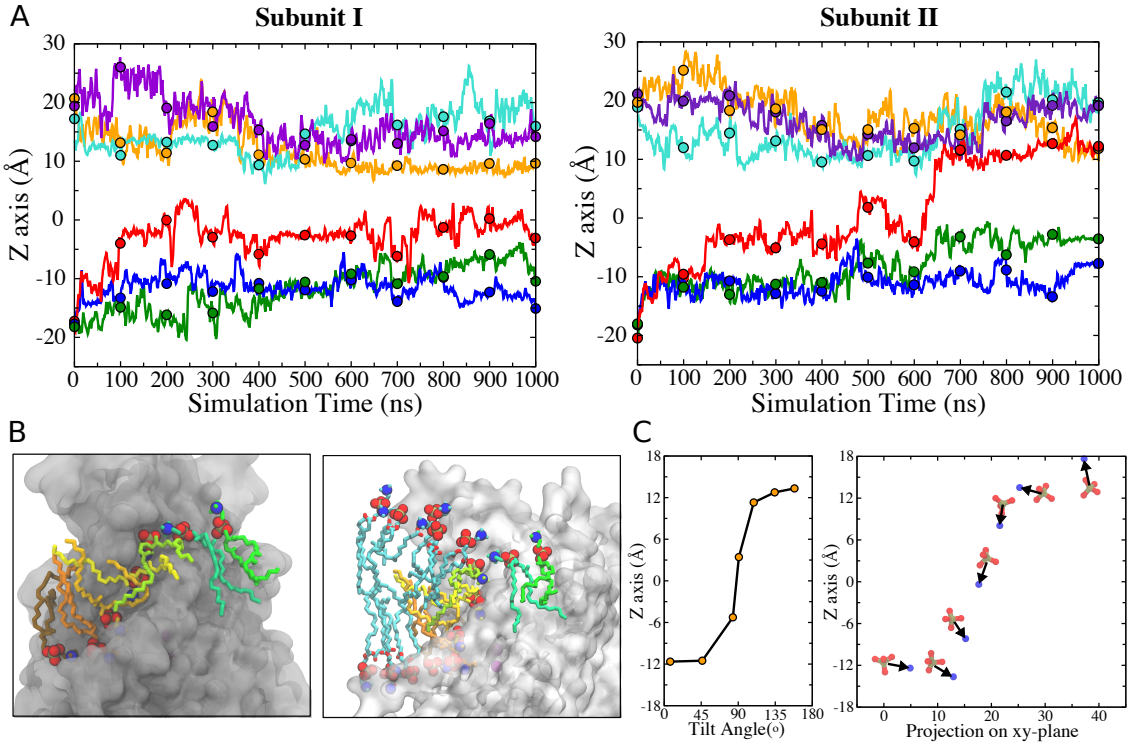

Figure 6.3: Lipid permeation under equilibrium condition. **(A)** Translocation of lipid along the aqueduct, measured as the positions of the phosphorus atoms in the aqueduct (along the z axis) versus time, with every 100-ns timepoint highlighted as a dot for 6 phospholipids that entered the aqueduct for subunit I (left) and subunit II (right). Complete flipping of a lipid from the inner leaflet to the outer leaflet is captured in subunit II (red trace). **(B)** Front (left) and side (right) views of the aqueduct showing the representative conformations of the lipids that occupy the aqueduct. Hydrocarbon chains of phospholipids inside the aqueduct are colored individually for clarity, phosphate groups and nitrogen atom of the choline/amino groups are shown in van der Waals (oxygen atoms are colored red, phosphorus tan and nitrogen blue). In the right panel, phospholipids in close proximity to the aqueduct are also shown (colored in cyan). The headgroups of these lipids are organized in a curve with the lipids closest to the aqueduct being located closer to z-axis = 0. **(C)** (left) Representative orientations of lipid tails along the aqueduct, with respect to the z axis; (right) corresponding P-N dipole orientations of the headgroups along the aqueduct.

While the phospholipid headgroup is wedged in the aqueduct, the flexible hydrocarbon tails extended into the membrane interior and remained in the hydrophobic phase of the membrane (Fig. 6.3(B)). Besides, hydrophobic interactions between the lipid tails and the lining helices (TM4 and TM6) are also frequently observed owing to the amphipathic nature of the two transmembrane

helices. In particular, the hydrophilic residues of TM4/6 mainly face toward the inside of the aqueduct, while the hydrophobic residues are exposed to the membrane interior. This structural arrangement allows lipid tails to splay out and make contacts with the lining helices, while the headgroup is wedged in the aqueduct (Fig. 6.3(B) left panel). Lipids that penetrate deep into the membrane are also commonly observed to have one alkyl tail attach to the hydrophobic surface of the lining helices, and the other tail extend into the hydrophobic core of the membrane as they climbing up along the aqueduct (Fig. 6.3(B) left panel), depending on their position inside the aqueduct and the surrounding environment. Notably, the lipid tails underwent roughly 360 degrees rotation as the headgroups move from one leaflet to the other along the aqueduct (Fig. 6.3(C)). The binding properties of lipid tails to the aqueduct emphasize the importance of hydrophobic interactions between the lipid and the protein.

6.3.3 Pinpointing the Residues Controlling Scrambling

To determine the residues that contribute to the binding of the phosphate groups at the most visited sites in the aqueduct, the contact number between phosphate groups and protein heavy atoms was calculated (Fig. 6.4(A)). S_{int} is located horizontally with respect to the bilayer at a similar level to the lower bound Ca^{2+} ion. Phosphate group at S_{int} is in direct contact with R505 from TM7 and Q374/N378 from TM5. Notably, R505 sits right between two negatively charge residues E506 and D503, which are highly conserved and contribute to coordinating the bound Ca^{2+} ions. S_{cen} is located about one third deep into the membrane thickness from the intracellular side, and is coordinated mainly by N378/T381/S382 from TM5, partially by T340 from TM4 and Y513 from TM7. S_{ext} is located near the extracellular entrance of the track, surrounded by several hydrophilic residues, including E313/N317 from TM3, G329/T333 from TM4, and R432/N435/Y439 from TM6.

To test whether amino acids that interact with the lipid headgroups in the simulation are crucial in phospholipid scrambling, mutations were introduced into the lipid-coordinating residues whose physicochemical properties were conserved between the scramblases nhTMEM16 and TMEM16F but were different in the Cl^- channel TMEM16A. We focused on TM4 and TM5 because we have previously shown that amino acids in this region in TMEM16F are essential for phospholipid

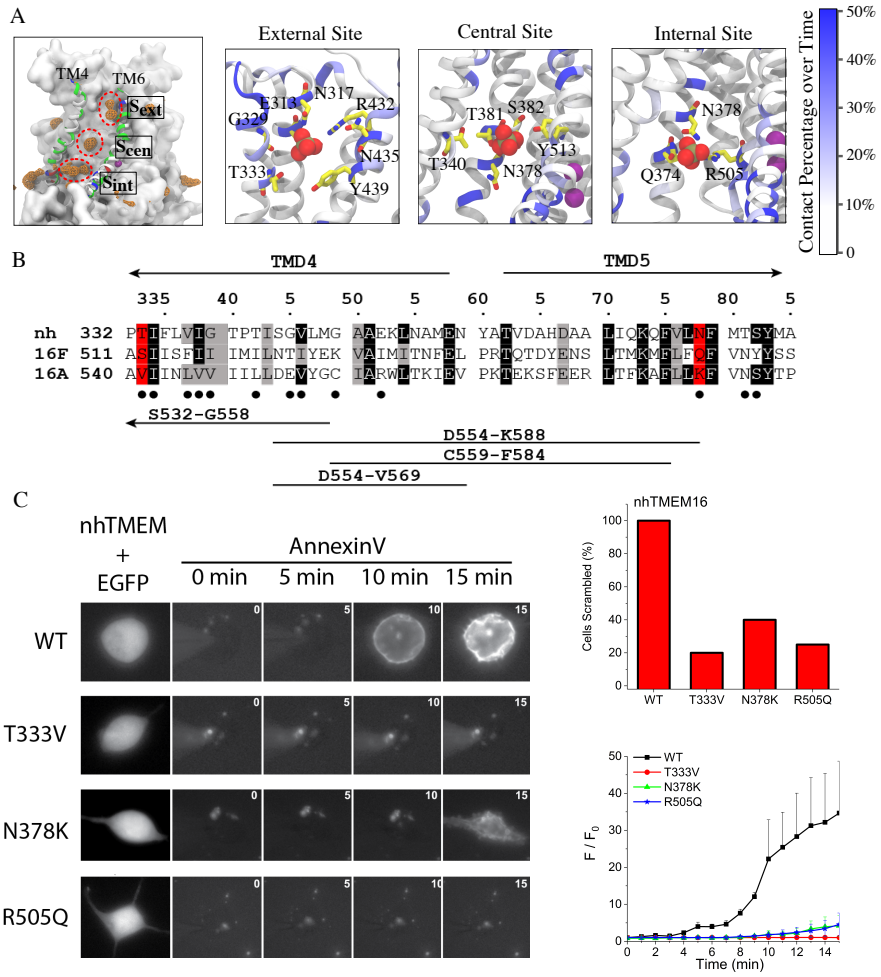

Figure 6.4: Lipid binding sites and effects of mutations in nhTMEM16. **(A)** Volumetric map of PO_4 occupancy extracted from the Ca^{2+}-activated simulation is shown as orange wireframe contoured at isovalue 0.15, overlaid on the protein structure. Three major binding sites of PO_4 within the aqueduct are circled and labeled, and individually illustrated in the panels to the right. Coordinating residues in each binding site are labeled. The protein is colored based on the frequency of each residue forming close contact (<3 Å) with phosphate groups during the simulation. The darkest blue color represents the residues with at least 50% contact percentage over time. **(B)** Alignments of TM4 and TM5 of nhTMEM16 (nh), mouse TMEM16F (16F), and mouse TMEM16A (16A). Structure-based alignments were performed using PROMALS3D. Amino acid backgrounds are colored to indicate identity (black) or similarity (grey). nhTMEM16 amino acids that interact intensively (cutoff 25%) with lipid headgroups during the simulation are indicated with a filled circle. Amino acids that interact intensively with lipid headgroups and are conserved between nhTMEM16 and TMEM16F but different in TMEM16A are highlighted in red. Consensus amino acid numbering in the top line refers to nhTMEM16. The number of the first residue shown for TMEM16F and TMEM16A precedes the sequence. At the bottom, the four lines indicate TMEM16A sequences that were replaced with TMEM16F sequences to convert TMEM16A into a phospholipid scramblase [255]. **(C)** (left) Effects of mutations in nhTMEM16 on phospholipid scrambling. Cells were co-transfected with plasmids encoding nhTMEM16 (WT or mutant) and EGFP. Transfected cells were identified by green fluorescence (left panel). Phospholipid scrambling was measured by binding of Annexin-V-AlexaFluor-568 at 0, 5, 10, and 15 min after establishing whole-cell recording with an internal solution containing 200 μM free Ca^{2+} (right panels). (right) Top: percentage of cells binding Annexin-V above background within 15 min after establishing whole cell recording with a high Ca^{2+} internal solution. Each bar represents 4 to 5 cells. Bottom: time course of phospholipid scrambling by WT and mutant nhTMEM16.

scrambling [255]. From the eight amino acids (filled circles under the alignment in Fig. 4(B)) in TM4-TM5 that are involved in lipid headgroup coordination, two amino acids (consensus positions 333 and 378, highlighted in red) were targeted for mutagenesis, since they are similar in nhTMEM16 and TMEM16F but distinctly different in TMEM16A. Two mutants were generated by mutating the two residues T333 and N378 to the amino acids corresponding to mouse TMEM16A (T333V and N378K). Intracellular Ca^{2+} was elevated by whole-cell patch clamping with an intracellular solution containing 200 M free [Ca^{2+}]. Phospholipid scrambling was assessed by imaging the accumulation of the PtdSer probe Annexin-V-AlexaFluor-568 on the cell surface. While most cells expressing WT nhTMEM16 had scrambled by 14 min after establishing whole cell recording, in the same time period little scrambling was observed in the cells expressing mutant nhTMEM16s (Fig. 6.4(C)). Since TMEM16A does not support phospholipid scrambling, the significant reduction of lipid scrambling in the nhTMEM16 T333V and N378K mutants indicated that residues T333 and N378 are important in the scrambling mechanism.

6.3.4 Ionic Currents Associated With Lipid Scrambling

To investigate the relationship between ion conduction and lipid scrambling by nhTMEM16, ionic currents were also measured simultaneously in HEK cells transiently transfected with WT or mutant nhTMEM16 in response to voltage steps from -100 mV to +100 mV in 20 mV increments. In an attempt to improve nhTMEM16 expression, a codon-optimized nhTMEM16 cDNA was synthesized. Although nhTMEM16 tagged on the C-terminus with EGFP did not traffic to the plasma membrane (as previously reported30), nhTMEM16 tagged on the N-terminus with 3X-FLAG or untagged nhTMEM16 did traffic to the plasma membrane (Fig. 6.5(A)) and elicited phospholipid scrambling and ionic currents when intracellular Ca^{2+} was elevated (Fig. 6.5(B)). Elevation of cytosolic Ca^{2+} by establishing whole-cell recording with high Ca^{2+} in the patch pipet resulted in exposure of PtdSer over 5-10 min that was accompanied by a large ionic current. The development of the ionic current slightly preceded Annexin-V binding, but as we have discussed previously [255], we believe that this lag is explained by limitations in detecting Annexin-V accumulation on the membrane and that the current and phospholipid scrambling occur simultaneously.

WT nhTMEM16 ionic current activated by 200 μM free Ca^{2+} exhibited a linear current-voltage

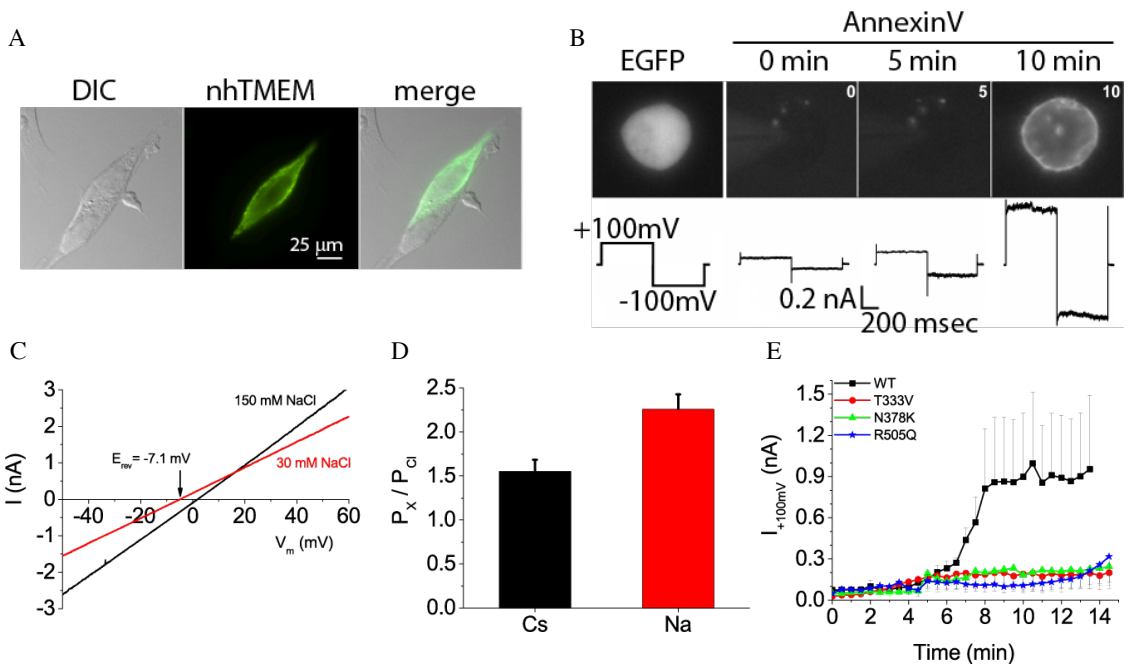

Figure 6.5: Phospholipid scrambling and ionic currents in nhTMEM16. **(A)** 3X-FLAG-nhTMEM16 is trafficked to the plasma membrane of HEK-293 cells. Cells were transiently transfected with a synthetic codon-optimized nhTMEM16 tagged on the N-terminus with 3X-FLAG. Cells were fixed and stained with anti-FLAG antibody followed by a fluorescent secondary antibody and imaged with a wide-field microscope. Left: differential interference contrast image. Middle: immunofluorescence. Right: merged image. Two attached cells are shown. One cell was transfected with nhTMEM16 and one was not transfected. **(B)** Phospholipid scrambling and ionic currents are stimulated in HEK cells transfected with nhTMEM16 and co-transfected with a plasmid encoding EGFP. Transfected cells were identified by green fluorescence (left panel). Phospholipid scrambling was measured by binding of Annexin-V-AlexaFluor-568 at 0, 5, 10, and 15 min after establishing whole-cell recording with an internal solution containing 200 μM free Ca^{2+}. Ionic currents recorded by a voltage protocol from a holding potential of 0 mV to +100 mV followed by a step to -100 mV are shown below each Annexin-V fluorescent image. Untransfected HEK cells do not scramble in the 15 min time frame as previously shown [255]. **(C)** Ionic selectivity of WT nhTMEM16 currents. Current-voltage relationships were measured using voltage ramps 1-sec duration from -100 mV to +100 mV. Ionic selectivity was determined by the change in reversal potential measured in response to switching between extracellular solutions containing 150 mM NaCl (black curves) and 30 mM NaCl (red curves). **(D)** Relative permeability of Na^+ and Cs^+ to Cl^- (PNa:PCl and PCs:PCl) calculated from the Goldman-Hodgkin-Katz equation. **(E)** Time course of development of ionic currents at +100 mV by WT and mutant TMEM16.

relationship that reversed around zero mV under symmetrical ionic conditions. To determine ionic selectivity, we measured the change in reversal potential (E_{rev}) in response to reducing extracellular NaCl (or CsCl)) from 150 mM to 15 mM. Upon 10-fold reduction in NaCl, E_{rev} shifted -7 mV (Fig. 6.5(C)), which corresponds to PNa:PCl = 2.3 ± 0.2 as calculated by the Goldman, Hodgkin, Katz equation (Fig. 6.5(D)). PCs:PCl was 1.5 ± 0.1. The development of ionic currents was greatly reduced in cells expressing mutant nhTMEM16, which suggests that ionic currents are linked to

phospholipid scrambling (Fig. 6.5(E)).

6.3.5 Testing the Model on Mammalian TMEM16F

To further validate the importance of the pinpointed amino acids T333 and N378 in phospholipid scrambling, we mutated these amino acids in the mammalian TMEM16 scramblase TMEM16F, and measured phospholipid scrambling and ionic currents (Fig. 6.6(A) and (C)). As previously reported, $>80\%$ of HEK cells expressing WT TMEM16F exhibited Annexin-V binding within 15 min of establishing whole-cell recording with a high Ca^{2+} intracellular solution (Fig. 6.6(C)). The WT TMEM16F-expressing cells also exhibited robust non-selective currents that developed roughly in parallel with Annexin-V binding. When TMEM16F Q559 was mutated to the corresponding TMEM16A residue (K), scrambling was greatly reduced (Fig. 6.6(C)) as were ionic currents. Replacing TMEM16F Q559 with the corresponding amino acid from nhTMEM16 (Q559N) did not abrogate scrambling by TMEM16F (Fig. 6.6(C)). These data confirm that the residue in TMEM16F homologous to nhTMEM16 N378 is important in phospholipid scrambling. Mutating S514 in TMEM16F to the corresponding nhTMEM16 amino acid (T) had no effect on scrambling, as expected. However, while we expected that replacing TMEM16F S514 with V from TMEM16A would abrogate scrambling, this mutation had little effect on scrambling.

6.3.6 Point Mutations Confer Scramblase Activity on TMEM16A

Previously we reported that replacing short TMEM16A sequences in TM4-TM5 with corresponding TMEM16F sequences caused TMEM16A to scramble phospholipids robustly, while the WT TMEM16A exhibited no measureable scramblase activity [255]. In contrast, chimeras involving other regions, including TMs 2, 3, 6, 7, 9, and 10 did not convert TMEM16A into a scramblase. We therefore asked whether TMEM16A could be converted to a phospholipid scramblase by mutating V543 to the homologous scramblase amino acids (T in nhTMEM16 or S in TMEM16F). As a control, less than 20% of the WT TMEM16A-expressing cells exhibited scramblase activity within 15 min of cytosolic Ca^{2+} elevation (Fig. 6.6(B) and (D)). Surprisingly, transfected cells expressing either V543T or V543S point mutations in TMEM16A exhibited robust phospholipid scrambling in

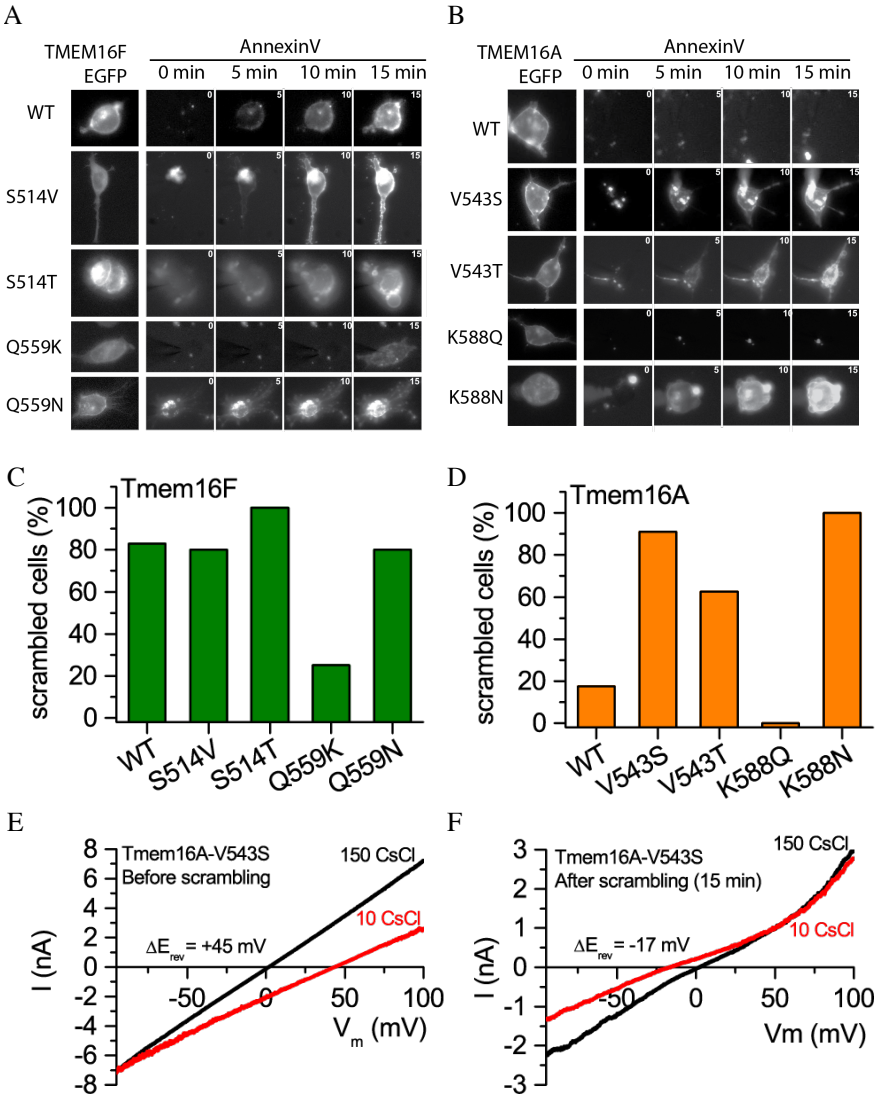

Figure 6.6: Effects of swapping amino acids between TMEM16A, TMEM16F, and nhTMEM16. **(A)** and **(B)** Images of cells during phospholipid scrambling. Single cells were patch clamped and intracellular Ca^{2+} controlled by 200 μM Ca^{2+} in the pipet. The first image in each row is EGFP fluorescence of the tagged TMEM16 protein. The next images are Annexin-V fluorescence taken 0, 5, 10, and 15 min after raising Ca^{2+} by initiating whole cell recording. **(A)** TMEM16F WT and mutations. **(B)** TMEM16A WT and mutations. **(C)** and **(D)** Percentage of cells binding Annexin-V within 15 min after establishing whole cell recording with a high Ca^{2+} internal solution. Each bar represents between 5 and 29 cells. **(C)** TMEM16F wild type (WT) and mutants. **(D)** TMEM16A wild type (WT) and mutants. **(E)** and **(F)** The V543S mutation in TMEM16A alters ionic selectivity. Current-voltage relationships were measured using voltage ramps of 1-sec duration from -100 mV to +100 mV. Ionic selectivity was determined by the change in reversal potential measured in response to switching between extracellular solutions containing 150 mM CsCl (black curves) and 10 mM CsCl (red curves). **(E)** Switching between 150 mM and 10 mM CsCl immediately after establishing whole-cell recording shifted E_{rev} +45 mV, corresponding to a PCl:PCs = 9.7, whereas **(F)** switching after Annexin-V binding had reached a plateau, E_{rev} shifted -17 mV in the opposite direction, corresponding to PCl:PCs = 0.45.

the same time period (Fig. 6.6(D)), consistent with the hypothesis that this amino acid plays a key role in conducting lipids across the bilayer. Replacing TMEM16A K588 with the corresponding nhTMEM16 amino acid N (K588N) also induced robust phospholipid scrambling (Fig. 6.6(D)). However, replacing K588 with the corresponding TMEM16F amino acid Q did not induce scrambling. One possible explanation is that the sidechain of N is considerably shorter (3.7 Å) than Q (4.9 Å) or K (6.2 Å). This raises the possibility that both charge and size of the sidechain may be important in determining whether scrambling is supported by the amino acid at this position. The ability to convert TMEM16A into a phospholipid scramblase by point mutations in each of two major amino acids identified as interacting with translocating lipids in the MD simulation strongly supports the validity of the MD model. Furthermore, this experimental result provides additional support for the idea that the TMEM16 Cl^- channels and scramblases are structurally very similar.

In addition to conferring scramblase activity on TMEM16A, the V543S mutation also changes the ionic selectivity of TMEM16A (Fig. 6.1(E) and (F)). Immediately after initiating whole-cell recording, TMEM16A V543S currents were strongly Cl^- selective, because switching from extracellular 150 mM CsCl to 10 mM CsCl caused a 45 mV positive shift of the reversal potential (E_{rev}) corresponding to PCl/PCs = 9.7 (Fig. 6.1(E)). However, after phospholipid scrambling had developed, the ionic current became weakly cation-selective as evidenced by a -17 mV negative shift in E_{rev} corresponding to a 21-fold decrease in anion selectivity (PCl/PCs = 0.45) (Fig. 6.1(F)). Thus, the V543S mutant of TMEM16A appears to function as a Cl^- channel until phospholipid scrambling is activated when the current becomes significantly less anion selective. Similar results were obtained with the V543T and K588N mutations, while K588Q was Cl^- selective.

6.3.7 Ionic Conductance Occurs Through the Same Structural Pathway

To further explore the relationship between the ionic currents and phospholipid scrambling, we applied three levels of transmembrane electric potentials (150 mV, 250 mV, and 500 mV) in MD simulations to gain insights on the pathway and mechanism of ion permeation. Under the transmembrane potentials, the phosphate groups inside the aqueduct became slightly denser compared to their distribution under equilibrium condition. Notably, Na^+ permeation from the extracellular side to the intracellular side of the membrane was captured in all three simulations through the

same aqueduct which serves as the pathway for lipid movement. With small, physiological potentials 150 mV and 250 mV, Na^+ permeation event occurs in subunit I and II, respectively, during the 700 ns simulations. The permeant Na^+ ions both are well coordinated while moving along the aqueduct (Fig. 6.7(A) and (B)). The average coordination number during the course of translocation is 5.65 ± 0.52 and 5.73 ± 0.51 for each case, contributed by oxygen atoms from water molecules (79%/85%), as well as protein (11%/10%) and lipids (9%/5%) (Fig. 6.7(A) and (B) left panels). Two major ion binding sites are revealed while the permeant Na^+ transverse the membrane, where the ions dwell for an extended time (Fig. 6.7(A) and (B) middle panels). The ion binding sites are strongly associated with the phosphate binding sites revealed in the equilibrium simulation. One ion binding site is located around the S_{ext} site (Fig. 6.4(A)) for lipid phosphate groups, and is coordinated by the oxygen atoms from Asn310, Glu313, Gly329, Thr333, Gln436, and Tyr439. The other site is near the S_{cen} site (Fig. 6.4(A)), which involves coordination from residues Thr381, Ser382, Asn448, and Tyr513. Gln374 from S_{int} and two glutamate residues (Glu496 and 497) near the intracellular entrance of the aqueduct also interact transiently with the ions as they diffuse away the aqueduct. Intriguingly, Thr333, which is the residue that interacts most intensively with the permeant ions, is also identified as the key residue that can switch on and off the lipid scrambling.

The consistent coordination of the permeant Na^+ ions from water molecules as well as protein and lipids indicates the formation of a "proteolipidic" pore along the hydrophilic aqueduct, where lipids play a structural role by lining the hydrophilic ion conduction pathway with their headgroups (Fig. 6.7(A) and (B) right panels). With 500 mV potential applied, increased probability of Na^+ permeation through the aqueous pore formed between the protein and the lipid headgroups was observed in both subunit I (14 occurrences) and II (10 occurrences) over the 700 ns simulation (Fig. 6.7(C)). Importantly, breathing motion of the pathway lining helices TM4 and 6 took place during the simulation, leading to a conductive state of the ion permeation pathway which allows for rapid and frequently ion conduction over a short period of time (10s of ns). Except for an outlier ion permeation, which took place when the pathway was not in its fully conductive state, all the permeation events lasted less than 20 ns, with one third of the them took place within 5 ns (Fig. 6.7(D)).

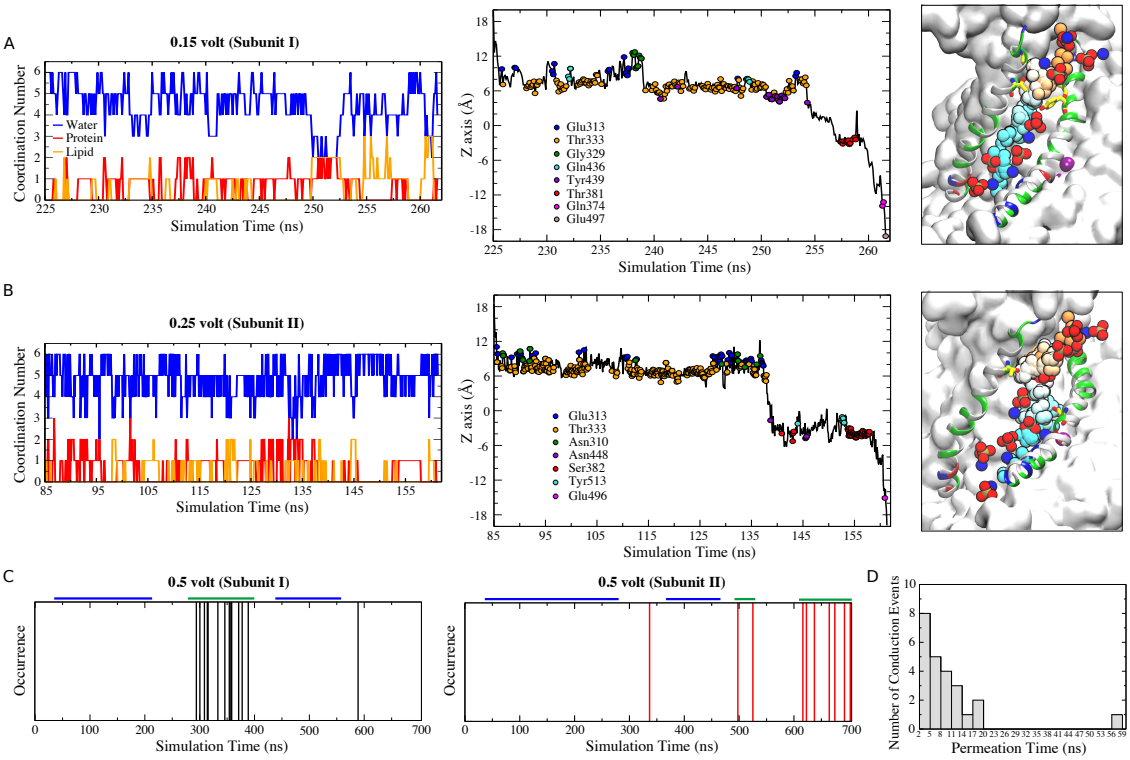

Figure 6.7: Ion permeation through the same structural pathway of lipid scrambling. **(A)** Full permeation of one Na^+ ion from the extracellular side to the intracellular side of the membrane was observed in subunit I of a 700 ns simulation with 150 mV transmembrane potential. Left panel: Coordination number of the permeant Na^+ ion as a function of time. Oxygen atoms from protein (red) and lipid headgroups (orange) both contribute to the ion coordination throughout its permeation (∼36.7 ns duration). The coordination number for water oxygen atoms are colored blue. Middle panel: Translocation of the permeant Na^+ through the aqueduct, measured as its z coordinate versus permeation time. The coordinating residues during ion permeation are shown as dots color-coded to the amino acid residues in the inset. Right panel: Time series snapshots representing translocation of the Na^+ ion (time is represented in pseudocolor from orange (start) to cyan (end). **(B)** One Na^+ permeation event (∼76.4 ns duration) occurs in subunit II of a 700 ns simulation with 250 mV transmembrane potential. The coloring schemes are the same as (A). **(C)** Multiple ion permeation events occur in both subunits with 500 mV membrane potential during the 700 ns simulation. The segments marked by the blue and green bars were used for measuring the center of mass distances between the aqueduct lining helices TM4 and TM6 as shown in Suppl. Fig.x. **(D)** Distribution of the ion permeation time for the 24 permeation events follows an exponential distribution, one third of the events took place within 5 ns.

6.3.8 POPS Externalizing and Lipid Selectivity

To analyze lipid scrambling under external electric field, a combined simulation trajectory with a total aggregate time of 1700 ns (1000 ns simulation without transmembrane potential, followed by 700 ns simulation with 500 mV potential) was used. In addition to the 3 half-flopping (2 POPC and 1 POPS, from inner leaflet to the membrane midplane) and 1 half-flipping (1 POPC, from

outer leaflet to the membrane midplane) in subunit I, collectively, 5 full lipid permeation from the inner leaflet to the outer leaflet were captured in subunit I (1 POPS) and II (1 POPS and 3 POPC) (Fig. 6.8(A)). For both fully scrambled POPS lipids, the headgroups are well coordinated by oxygen and nitrogen atoms from the protein as they move along the aqueduct (Fig. 6.8(B)). In both cases, the headgroups interact most intensively with Arg505 (79.52% and 59.01% of the scrambling time, respectively); Glu496 and Asn378 also contribute significantly ($> 10\%$ of the scrambling time) to the coordination. Compared to POPS, in general, the fully scrambled POPC lipids interact much less intensively with the protein (Fig. 6.8(C)). In each of the three POPC scrambling events, two residues are found to interact significantly with the headgroup (POPC I: Arg505 and Arg432, POPC II: Lys459 and Arg505, POPC III: THR381 and TYR439), however, none of them interact over 15% of the scrambling time. The major difference between the scrambling of POPS and POPC through the aqueduct is the intensity of headgroup coordination from the protein during the scrambling process (Fig. 6.8(B) and (C) lower panels, Fig. 6.8(D)). The scrambled POPS headgroup is coordinated by at least two oxygen/nitrogen atoms from the protein for 42.72% (POPS I) or 55.83% (POPS II) of the scrambling time; while for POPC, the probability of having at least two coordination during the scrambling is reduced to 11.80% (POPC I), 0.80% (POPC II), and 2.32% (POPC III) (Fig. 6.8(D)).

To gain insight on lipid selectivity, we look into the residues that strongly coordinate (coordination ratio > 0.2) the lipid headgroups during the 1700 ns simulation. In addition to the three residues (Arg505, Glu496, and Arg548) (Fig. 6.8(E) and (F)) that are located inside the aqueduct and interact almost exclusively with POPS, several residues that are located near and beside the intracellular entrance of the aqueduct are identified to favor the binding of POPS over POPC. Intriguingly, we also spot residues that are located near the dimer interface that interact extensively and specifically with POPS headgroup. Except for Lys470, Lys353, Lys286 and Lys459, all the rest 26 residues in Fig. 6.8(E) interact at least 75% stronger with POPS than POPC, and 14 of them interact at least 10 times stronger with POPS, even though the concentration of POPC is two times of POPS in the inner leaflet.

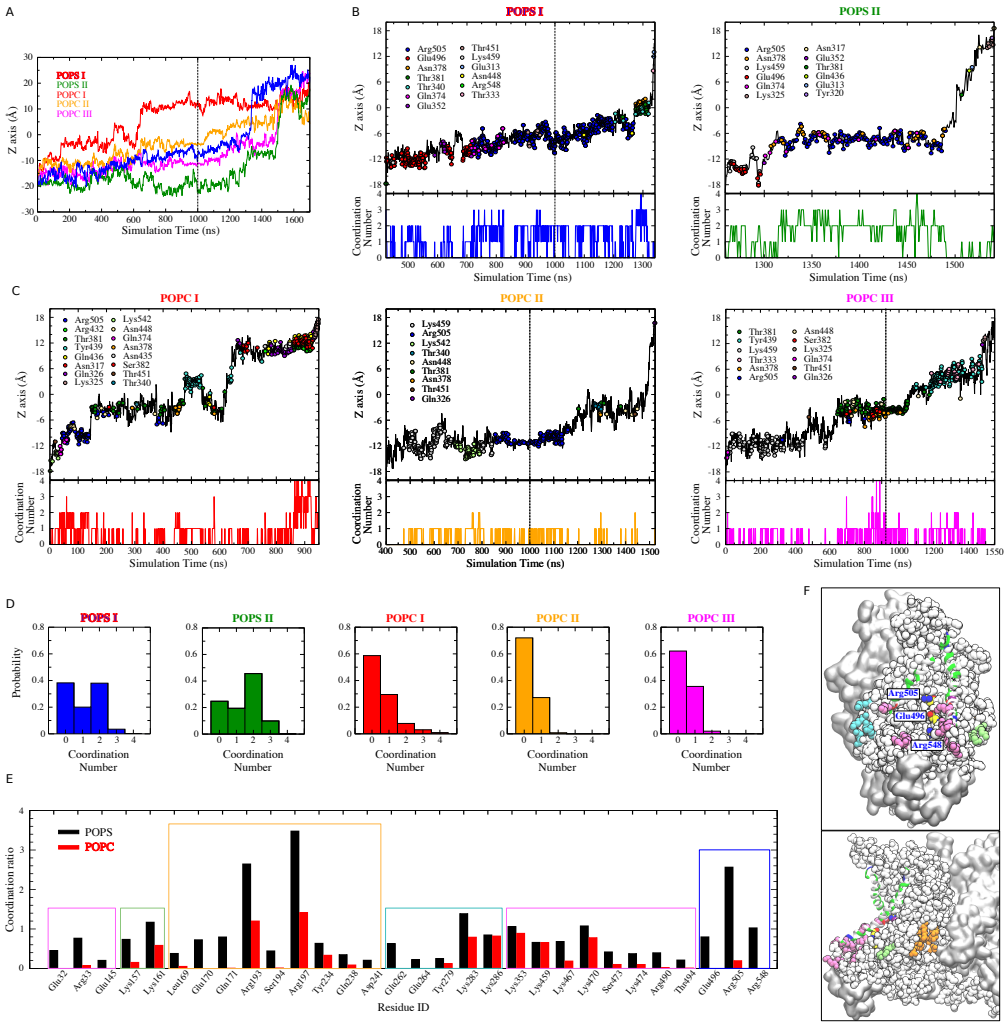

Figure 6.8: POPS are better coordinated than POPC during flopping. **(A)** Multiple lipid scrambling (POPS and POPC) from the inner leaflet to the outer leaflet were captured in both subunits during the 1700 ns simulation (1000 ns equilibrium followed by 700 ns simulation with 500 mV transmembrane potential). The dashed line indicates the time point of adding external electric field. **(B)** Full permeation of POPS in subunit I (left) and II (right). Top panels: Translocation of the scrambled POPS through the aqueduct, measured as the position (z coordinate) of the phosphorus atom of the phosphate group versus the scrambling time. The headgroup coordinating residues during the lipid flopping are shown as dots color-coded to the amino acid residues in the inset. Lower panels: Headgroup coordination number of the scrambled POPS as a function of time. **(C)** Full permeation of POPC. POPC I (red) was fully scrambled under equilibrium condition, before the external electric field was applied. The coloring schemes are the same as (B). **(D)** Normalized probability histograms of the headgroup coordination number during the lipid scrambling for each scrambled lipid. POPC are less coordinated by the protein compared to POPS. **(E)** Comparison of POPS and POPC headgroups coordination from residues that frequently (ratio > 0.2) coordinate the POPS headgroups during the 1700 ns simulation. The residues are highlighted in (F) in the colors corresponding to the colored box in (E). **(F)** Residues located inside the aqueduct are individually labelled (Arg505, Glu496, and Arg548). Residues located near the intracellular entrance of the aqueduct are colored in mauve. Residues located outside the aqueduct are colored in cyan (on the left of the aqueduct), lime (on the right of the aqueduct), and orange (near the dimer interface).

6.3.9 Insights Into Ca^{2+} Activation

In contrast to the Ca^{2+}-activated simulation, full occupancy of phosphate groups along the aqueduct did not occur in either subunit of the Ca^{2+}-free simulation. Examination of the trajectory showed that in the absence of Ca^{2+}, phosphate groups mainly packed near the intracellular and extracellular entrances of the aqueduct, rather than penetrating into the membrane center, resulting in a 15-20 Å gap between the phosphate groups from the outer and inner leaflets. Thus, considerably less phosphate groups were observed in the aqueduct compared to the Ca^{2+}-activated simulation. The lack of headgroup penetration in the absence of Ca^{2+} ions strongly indicates that Ca^{2+} ions are vital for the scrambling activity, as has been demonstrated experimentally previously [253].

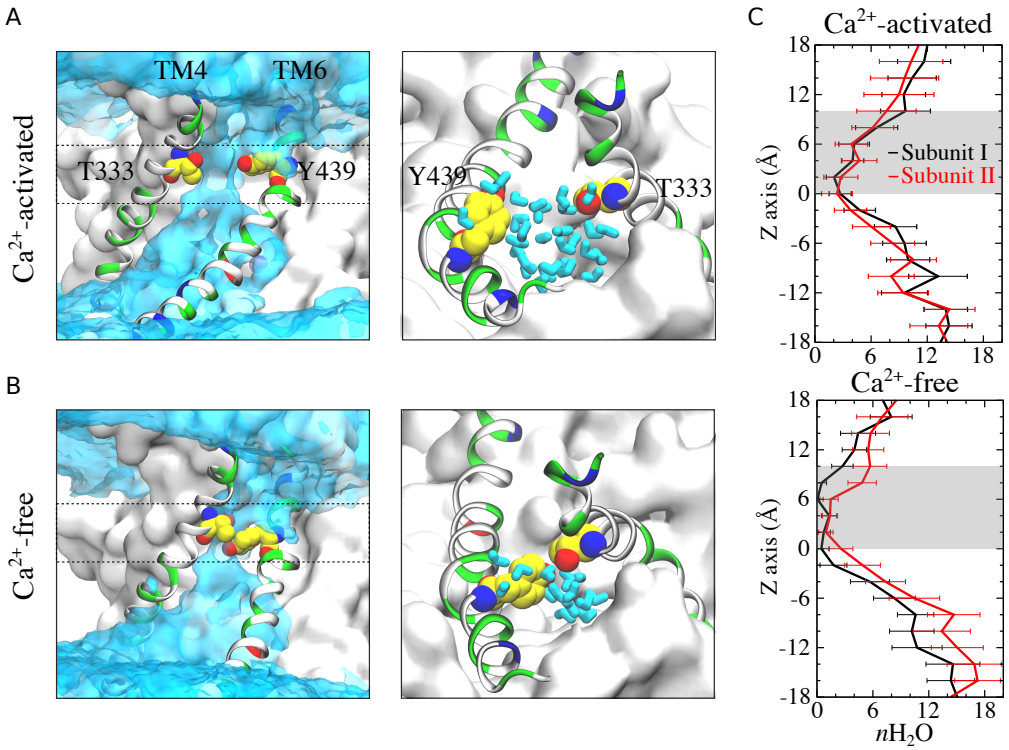

Figure 6.9: Hydration of the lipid aqueduct with and without Ca^{2+} ions. **(A)** and **(B)** Left panels: Average water density during the Ca^{2+}-activated and Ca^{2+}-free simulations is shown as transparent cyan surface contoured at 0.15 of bulk water density, overlaid on representative snapshots of the aqueduct for each system. Gating residues T333 and Y439 are shown as van der Waals spheres. The gating region of the track ($0 < z < 10$ Å, membrane center is set at $z = 0$) is highlighted by dashed lines. Left panels: Top views of the gating region of the track ($z > 10$ Å is removed for clarity). Water molecules in this region are colored in cyan. **(C)** Average number of water molecules in each aqueduct of the two systems during the last 150 ns of the 1000 ns simulations. The shaded grey area represents the gating region of the aqueduct.

To better understand the environment that affects lipid scrambling, we examined the behavior of water molecules within the aqueduct in the simulations with and without Ca^{2+}. Visualization of the averaged water density within the aqueduct revealed that the aqueducts in the Ca^{2+}-bound system are fully hydrated throughout the whole length, while the ones in the Ca^{2+}-free system display an apparent less hydrated region ($0 < z < 10\,\text{Å}$) compared to the Ca^{2+}-activated counterparts (Fig. 6.9). To determine whether the difference in hydration is a result of structural change of the aqueduct during the simulations, we examined the conformation of the aqueduct lining helices in both systems. In the Ca^{2+}-activated system, TM4 and TM6 maintained a similar conformation as seen in the crystal structure. While in the Ca^{2+}-free system, the aqueduct is pinched around the residue pair T333-Y439, resulting in a narrow gating region (region ($0 < z < 10\,\text{Å}$) of the aqueduct (Fig. 6.9(A)). In particular, the tight contact between T333 and Y439 as well as the neighboring residue pairs greatly narrowed the width of the aqueduct and confined the water molecules within in this region (Fig. 6.9(A)), such that fewer water molecules were accommodated in the gating region compared to the aqueducts in the Ca^{2+}- activated system (Fig. 6.9). Even though the aqueducts in the absence of Ca^{2+} ions are not completely dehydrated, the contact between T333 and Y439 sterically separates the lipid headgroups from outer and inner leaflets, and prevents them from penetrating deep into the aqueduct. Thus, Ca^{2+} ions are essential for the protein to maintain a stable and functional conformation, especially at the catalytic site - the lipid aqueduct - which not only affects the hydration of the aqueduct, but also determines the activity of the protein.

6.4 Summary and Perspective

The mechanism by which scramblase catalyzes rapid exchange of lipids between the two leaflets of a bilayer has been a long sought-after question. The molecular basis of the scrambling activity has been poorly understood, mainly due to the complexity of the cargo and the lack of knowledge on the machinery that catalyze the activity. The amphiphilic nature of lipids distinguishes scramblases from the commonly known transport proteins that facilitate the movement of substrate molecules by providing enclosed proteinaceous pores that are energetically favorable. In order to translocate lipids across the membrane, scramblases must provide a conduction pathway that is competent to accommodate the hydrophilic headgroups and the hydrophobic tails at the same time. One of the

most critical issues that motivated this study is to identify the pathway that could be taken by a polar headgroup moving from one leaflet to the other.

Earlier researchers had proposed several possible mechanisms for the transbilayer movement of the amphipathic cargo even before a lipid scramblase was identified. One model proposes that dynamics of the transmembrane proteins may interrupt the normal bilayer structure and, thereby enhance the chance for a lipid to transverse the membrane. This idea was initially proposed by Kol and colleagues [256, 257] based on the investigation of lipid flip rate facilitated by the artificially constructed alpha helical peptides. However, this idea only favors small membrane-spanning proteins, and works best with the single helices, because they are more dynamic and prone to cause transient defects in the lipid-helix interface. Some other models suggest that the rapid rearrangement of lipids across the membrane could be facilitated by the amphiphilic transmembrane helices which may provide a hydrophilic surface for the passage of lipid polar headgroups. Pomorski and Menon [258] suggested a further variation on these ideas by proposing that just like swiping a card through a card reader, the lipid headgroup is sequestered from the unfavorable hydrophobic environment by passing through a groove of transmembrane proteins as it transits the membrane interior, during which the lipid tails remain in the hydrophobic phase of the membrane. This mechanism is extremely appealing as the crystallization of the nhTMEM16 scramblase revealed a $\sim$10 Å wide partially hydrophilic aqueduct, exposed to the membrane interior such that may serve as a potential site of catalysis [134]. However, recent experiments revealed that increasing the headgroup size up to diameters of $\sim$40 Å does not alter the scrambling in the presence of Ca^{2+}, thus raised a major question involving this "card swiping" mechanism as how the aqueduct accommodates headgroups several folds larger than its width. Validation of these models requires an thorough understanding of the structural and functional properties of the scramblases.

Our simulations of the nhTMEM16 scramblase within a lipid membrane environment provided valuable input to elucidate a clear picture of the lipid scrambling process by the TMEM16 scramblase. The Ca^{2+}-activated simulation showed that the presence of nhTMEM16 has the potential to induce local deformation of membrane structure in its proximity, during which the bilayer structure near the aqueduct was staggered and thus uniquely thinned the membrane near the groove. The advantage of using lipids from both leaflets to significantly reduce the membrane thickness is that it

shortens the distance a lipid needs to transverse the membrane without large confomational change of the protein structure. Intriguingly, our analysis demonstrated that, as the simualtion extended, adjacent lipids underwent significant reorientation from a simple bilayer to form a hairpin-like structure. This nonbilayer arrangement of lipids allows headgroups to diffuse laterally between leaflets, which could greatly increase the rate of lipid exchange across the membrane. This observation thus brings detailed insights into the precise conformations and interactions of lipids surround the scramblase, and provides the first direct evidence for the long-standing speculation of lateral diffusion of lipids mediated by scramblase [259].

More importantly, our analysis revealed a lipid transport pathway lined by transmembrane helices TM4 and TM6, which maintained an open conformation and was sufficiently hydrated in the presence of Ca^{2+} ions throughout the simulation, permitting the spontaneous penetration and diffusion of polar headgroups. By providing the direct demonstration of lipid translocation across the membrane by way of the hydrated lipid aqueduct, our work enabled us to unveil several critical aspects involved in the scrambling process. In addition to the location of the lipid pathway, we have been able to pinpoint the major headgroup interacting sites along the track, and identify key residues involved in lipid-protein interactions. The lipid track was occupied mostly by POPC lipid headgroups, due to the dominant proportion of POPC in the bilayer (100% POPC in the outer leaflet and 67% POPC in the inner leaflet), however, POPS was also observed to be funneled into the track from the inner leaflet and bind around the S_{int} site throughout the simulation. The stable binding of POPS headgroup at S_{int} owes to the strong interaction between the negatively charged headgroup and the positively charge residue R505 of S_{int}, which might serve as a potential site for lipid selectivity at the intracellular entrance of the track. It is possible that the presence of different types of lipids might influence the biophysical properties of lipid headgroup conduction, as well as more global conformational changes of the membrane structure near the protein. Future simulations and experiments with more physiological lipid headgroup compositions and mixed lipid tail lengths are clearly needed to fully understand the behaviour of nhTMEM16 in complex bilayers.

With the lipid pathway as the focus for the rapid exchange of lipids across the membrane, the most important physiological question is how Ca^{2+} binding regulates the activity of the scramblase. Even though the large proteinaceous structure of nhTMEM16 suggests that Kol's model [256, 257]

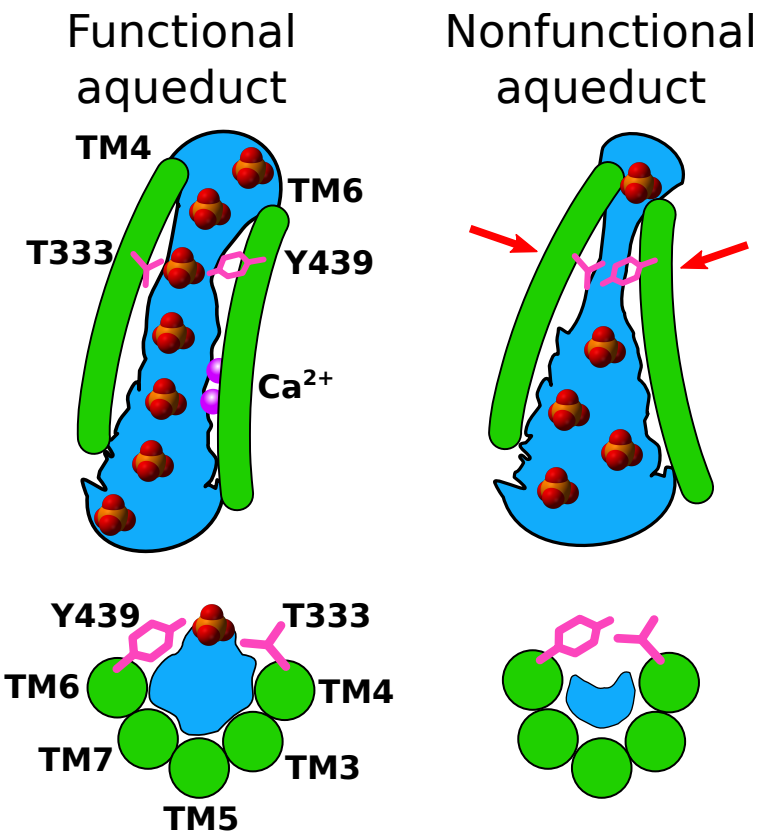

Figure 6.10: A model for Ca^{2+}-activated lipid scrambling. (top panels) (left) Hydration (blue) in the Ca^{2+}-activated functional aqueduct (Ca^{2+} ions are shown as purple spheres) provides a smooth pathway for lipid headgroups to pass through. (right) Tight contact between gating residues T333 and Y439 narrows the aqueduct, resulting in poor hydration in the gating region and prevents headgroups from passing through the aqueduct. (bottom panels) top views of the aqueducts showing the gating region and the hydration within this region.

which requires large motions of the helix bundles is not applicable, our analysis indicates that the structural dynamics in the aqueduct-lining helices TM4 and TM6 directly affect the aqueduct conformation, and consequently influence the function of the protein. To be specific, the functional open conformation in the presence of Ca^{2+} ensures a full hydration of the aqueduct during the simulation, thus that smooth lateral diffusion of headgroups along the aqueduct could happen spontaneously (Fig. 6.10 left panels). In particular, water molecules in the gating region fill up the most narrow and deep part of the aqueduct and provide a water pathway for lipid headgroups to glide on. This finding provides atomistic insight into why lipids with headgroups considerably larger than the aqueduct radius could be successfully scrambled. The absence of Ca^{2+}, on the other hand, markedly altered the structure of the aqueduct-lining helices, results in a nonfunctional

aqueduct that is sterically occluded by the gating residues T333-Y439 located near the center of the membrane (Fig. 6.10 right panels). The penetration of lipid headgroups is blocked in the nonfunctional aqueduct not only because of the closed gate, but also due to the poor hydration around the gating region.

In addition to characterizing the lipid transport pathway and its Ca^{2+} dependence, our simulations also provided the first glimpse into the ion channel properties of TMEM16 proteins. Since the crystal structure of nhTMEM16 does not reveal an obvious alternative pathway for ion permeation through the bilayer other than the path taken by phospholipids, the formation of the "proteolipidic" pore along the hydrophilic aqueduct provides important information on ion transport that is mediated by the same structure. In this flexible pore structure, lipids play a structural role by lining the hydrophilic ion conduction pathway with their headgroups. Ion permeation events through the aqueous pore formed between the protein and the lipid headgroups were captured frequently. The permeant Ions are well coordiated by residues lining the aqueduct as well as lipid headgroups occupying the aqueduct as they transverse the membrane. Moreover, externalization of the anionic phospholipid POPS along the pore was observed as water penetrates into the bilayer and extends across the membrane. This novel view of flexible pore structure explains a number of unusual features of the TMEM16 ionic currents, especially the highly variable ionic selectivity and the ability to permeate large ions.

The findings outlined above provide the first detailed picture of the scrambling process mediated by nhTMEM16, which serves as helpful input for developing a viable function model for the general mechanism. In summary, successful lipid translocation by the scramblase requires the presence of Ca^{2+} ions to maintain a functional aqueduct that is apparently open and fully hydrated, which allows deep penetration of lipid headgroups into the membrane interior and lateral diffusion of headgroups along the track. More importantly, the fully occupied aqueduct can also serve as the path for ion permeation, which is crucial for the functional dichotomy in TMEM16s. These results elucidate the atomic details of the lipid scrambling and ion permeation pathway and uncover the molecular basis of Ca^{2+}-dependence of nhTMEM16, thus extend our knowledge of the microscopic mechanism underlying the function of TMEM16 proteins. Taken together, our computational work sheds light on several most critical aspects of the substrate transport process by nhTMEM16,

including lipid scrambling and ion permeation, which have important implications for our understanding of other membrane transport systems, especially those control the translocation of the lipophilic molecules.

References

[1] G. Enkavi, J. Li, P. Wen, S. Thangapandian, M. Moradi, T. Jiang, W. Han, and E. Tajkhorshid. A microscopic view of the mechanisms of active transport across the cellular membrane. In *Annual Reports in Computational Chemistry*, volume 10, chapter 4, pages 77–125. Elsevier, 2014.

[2] J. V. Vermaas, N. Trebesch, C. Mayne, S. Thangapandian, M. Shekhar, P. Mahinthichaichan, J. L. Baylon, T. Jiang, Y. Wang, M. P. Muller, E. Shinn, Z. Zhao, P. Wen, and E. Tajkhorshid. Microscopic characterization of membrane transporter function by in silico modeling and simulation. In G. A. Voth, editor, *Computational Approaches for Studying Enzyme Mechanism Part B*, volume 578, chapter 16, pages 373–428. Academic Press, 2016.

[3] T. Jiang, W. Han, M. Maduke, and E. Tajkhorshid. Molecular basis for differential anion binding and proton coupling in the Cl^-/H^+ exchanger ClC-ec1. *J. Am. Chem. Soc.*, 138:3066–3075, 2016.

[4] C. M. Khantwal, S. J. Abraham, W. Han, T. Jiang, T. S. Chavan, R. C. Cheng, S. M. Elvington, C. W. Liu, I. I. Mathews, R. A. Stein, H. S. Mchaourab, E. Tajkhorshid, and M. Maduke. Revealing an outward-facing open conformational state in a CLC Cl^-/H^+ exchange transporter. *eLife*, 5:e11189, 2016.

[5] D. L. Nelson and M. M. Cox. *Lehninger Principles of Biochemistry.* Worth Publishers, 3rd edition, 2000.

[6] O. Jardetzky. Simple allosteric model for membrane pumps. *Nature*, 211(5052):969–970, 1966.

[7] H. Krishnamurthy, C. L. Piscitelli, and E. Gouaux. Unlocking the molecular secrets of sodium-coupled transporters. *Nature*, 459:347–355, 2009.

[8] K. P. Locher. Structure and mechanism of ATP-binding cassette transporters. *Phil. Trans. R. Soc. Lond. B*, 364(1514):239–245, 2009.

[9] O. Boudker and G. Verdon. Structural perspectives on secondary active transporters. *Trends Pharmacol. Sci.*, 31:418–426, 2010.

[10] L. R. Forrest, R. Krämer, and C. Ziegler. The structural basis of secondary active transport mechanisms. *Biochim. Biophys. Acta – Bioener.*, 1807(2):167–188, 2011.

[11] D. L. Kroetz, S. W. Yee, and K. M. Giacomini. The pharmacogenomics of membrane transporters project: Research at the interface of genomics and transporter pharmacology. *Clin. Pharmacol. Ther.*, 87:109–116, 2010.

[12] K. Vandivort, J. C. Phillips, E. Villa, P. L. Freddolino, J. Gumbart, L. G. Trabuco, D. E. Chandler, J. Hsin, C. B. Harrison, L. Kale, and K. Schulten. Long time and large size molecular dynamics simulations made feasible through new TeraGrid hardware and software. *Proceedings of the 2008 TeraGrid Conference*, 2008.

[13] R. O. Dror, M. O. Jensen, D. W. Borhani, and D. E. Shaw. Exploring atomic resolution physiology on a femtosecond to millisecond timescale using molecular dynamics simulations. *J. Gen. Physiol.*, 135:555–562, 2010.

[14] T. Schlick, R. Collepardo-Guevara, L. A. Halvorsen, S. Jung, and X. Xiao. Biomolecular modeling and simulation: a field coming of age. *Quart. Rev. Biophys.*, 44:191–228, 2011.

[15] J. B. Klauda, R. M. Venable, J. A. Freites, J. W. O'Connor, D. J. Tobias, C. Mondragon-Ramirez, I. Vorobyov, A. D. MacKerell Jr., and R. W. Pastor. Update of the CHARMM all-atom additive force field for lipids: Validation on six lipid types. *J. Phys. Chem. B*, 114(23):7830–7843, 2010.

[16] L. Shi, M. Quick, Y. Zhao, H. Weinstein, and J. A. Javitch. The mechanism of a neurotransmitter:sodium symporter–inward release of Na^+ and substrate is triggered by substrate in a second binding site. *Mol. Cell*, 30(6):667–677, 2008.

[17] S. Y. Noskov and B. Roux. Control of ion selectivity in LeuT: two Na^+ binding sites with two different mechanisms. *J. Mol. Biol.*, 377:804–818, 2008.

[18] I. H. Shrivastava, J. Jiang, S. G. Amara, and I. Bahar. Time-resolved mechanism of extracellular gate opening and substrate binding in a glutamate transporter. *J. Biol. Chem.*, 283:28680–28690, 2008.

[19] R. S. G. D'rozario and M. S. P. Sansom. Helix dynamics in a membrane transport protein: comparative simulations of the glycerol-3-phosphate transporter and its constituent helices. *Mol. Membr. Biol.*, 25:571–573, 2008.

[20] Y. Wang, Y. Z. Ohkubo, and E. Tajkhorshid. Gas conduction of lipid bilayers and membrane channels. In S. Feller, editor, *Current Topics in Membranes: Computational Modeling of Membrane Bilayers*, volume 60, chapter 12, pages 343–367. Elsevier, 2008.

[21] P.-C. Wen and E. Tajkhorshid. Dimer opening of the nucleotide binding domains of ABC transporters after ATP hydrolysis. *Biophys. J.*, 95(11):5100–5110, 2008.

[22] L. Celik, B. Schiott, and E. Tajkhorshid. Substrate binding and formation of an occluded state in the leucine transporter. *Biophys. J.*, 94:1600–1612, 2008.

[23] Z. Huang and E. Tajkhorshid. Dynamics of the extracellular gate and ion-substrate coupling in the glutamate transporter. *Biophys. J.*, 95:2292–2300, 2008.

[24] C. J. Law, G. Enkavi, D.-N. Wang, and E. Tajkhorshid. Structural basis of substrate selectivity in the glycerol-3-phosphate:phosphate antiporter GlpT. *Biophys. J.*, 97:1346–1353, 2009.

[25] J. Gumbart, M. C. Wiener, and E. Tajkhorshid. Coupling of calcium and substrate binding through loop alignment in the outer membrane transporter BtuB. *J. Mol. Biol.*, 393:1129–1142, 2009.

[26] J. Li and E. Tajkhorshid. Ion-releasing state of a secondary membrane transporter. *Biophys. J.*, 97:L29–L31, 2009.

[27] E. Zomot and I. Bahar. The sodium/galactose symporter crystal structure is a dynamic, not so occluded state. *Mol. BioSys.*, 6:1040–1046, 2010.

[28] A. Watanabe, S. Choe, V. Chaptal, J. M. Rosenberg, E. M. Wright, M. Grabe, and J. Abramson. The mechanism of sodium and substrate release from the binding pocket of vSGLT. *Nature*, 468:988–991, 2010.

[29] J. Aittoniemi, H. de Wet, F. M. Ashcroft, and M. S. P. Sansom. Asymmetric switching in a homodimeric ABC transporter: A simulation study. *PLoS Comput. Biol.*, 6(4):e1000762, 2010.

[30] Z. Huang and E. Tajkhorshid. Identification of the third Na^+ site and the sequence of extracellular binding events in the glutamate transporter. *Biophys. J.*, 99:1416–1425, 2010.

[31] G. Enkavi and E. Tajkhorshid. Simulation of spontaneous substrate binding revealing the binding pathway and mechanism and initial conformational response of GlpT. *Biochemistry*, 49:1105–1114, 2010.

[32] S. A. Shaikh and E. Tajkhorshid. Modeling and dynamics of the inward-facing state of a Na^+/Cl^- dependent neurotransmitter transporter homologue. *PLoS Comput. Biol.*, 6(8):e1000905, 2010.

[33] P.-C. Wen and E. Tajkhorshid. Conformational coupling of the nucleotide-binding and the transmembrane domains in the maltose ABC transporter. *Biophys. J.*, 101(3):680–690, 2011.

[34] J. Li and E. Tajkhorshid. A gate-free pathway for substrate release from the inward-facing state of the Na^+-galactose transporter. *Biochim. Biophys. Acta Biomembr.*, 1818:263–271, 2012.

[35] C. Zhao and S. Noskov. The role of local hydration and hydrogen-bonding dynamics in ion and solute release from ion-coupled secondary transporters. *Biochemistry*, 50:1848–1856, 2011.

[36] J. Dechancie, I. H. Shrivastava, and I. Bahar. The mechanism of substrate release by the aspartate transporter Glt_{Ph}: Insights from simulations. *Mol. BioSys.*, 7:832–842, 2011.

[37] G. Gyimesi, S. Ramachandran, P. Kota, N. V. Dokholyan, B. Sarkadi, and T. Hegedüs. ATP hydrolysis at one of the two sites in ABC transporters initiates transport related conformational transitions. *Biochim. Biophys. Acta*, 1808(12):2954–2964, 2011.

[38] E. Zomot and I. Bahar. Protonation of glutamate 208 induces the release of agmatine in an outward-facing conformation of an arginine/agmatine antiporter. *J. Biol. Chem.*, 286:19693–19701, 2011.

[39] E. Zomot and I. Bahar. A conformational switch in a partially unwound helix selectively determines the pathway for substrate release from the carnitine/γ-butyrobetaine antiporter CaiT. *J. Biol. Chem.*, 287:31823–31832, 2012.

[40] P.-C. Wen, Z. Huang, G. Enkavi, Y. Wang, J. Gumbart, and E. Tajkhorshid. *Molecular mechanisms of active transport across the cellular membrane*, chapter 10, pages 248–286. Royal Society of Chemistry, 2010.

[41] J. M. Johnston and M. Filizola. Showcasing modern molecular dynamics simulations of membrane proteins through g protein-coupled receptors. *Curr. Opin. Struct. Biol.*, 21:552–558, 2011.

[42] M. Musgaard, L. Thøgersen, B. Schiøtt, and E. Tajkhorshid. Tracing cytoplasmic Ca^{2+} ion and water access points in the Ca^{2+}-ATPase. *Biophys. J.*, 102(2):268–277, 2012.

[43] S. A. Shaikh and E. Tajkhorshid. Potential cation and H^+ binding sites in acid sensing ion channel-1. *Biophys. J.*, 95:5153–5164, 2008.

[44] F. Khalili-Araghi, J. Gumbart, P.-C. Wen, M. Sotomayor, E. Tajkhorshid, and K. Schulten. Molecular dynamics simulations of membrane channels and transporters. *Curr. Opin. Struct. Biol.*, 19:128–137, 2009.

[45] Y. Wang, S. A. Shaikh, and E. Tajkhorshid. Exploring transmembrane diffusion pathways with molecular dynamics. *Physiology*, 25:142–154, 2010.

[46] S. A. Shaikh, P.-C. Wen, G. Enkavi, Z. Huang, and E. Tajkhorshid. Capturing functional motions of membrane channels and transporters with molecular dynamics simulation. *J. Comput. Theor. Nanosci.*, 7:2481–2500, 2010.

[47] Z. J. Huang, S. A. Shaikh, P.-C. Wen, G. Enkavi, J. Li, and E. Tajkhorshid. *Membrane Transporters - Molecular Machines Coupling Cellular Energy to Vectorial Transport Across the Membrane*. World Scientific, 2011.

[48] T. J. Jentsch. CLC chloride channels and transporters: from genes to protein structure, pathology and physiology. *Crit. Rev. Biochem. Mole. Biol.*, 43(1):3–36, 2008.

[49] T. Stauber, S. Weinert, and T. J. Jentsch. Cell biology and physiology of CLC chloride channels and transporters. *Compr. Physiol.*, 2(3):1701–1744, 2012.

[50] G. Y. Rychkov, M. Pusch, M. L. Roberts, T. J. Jentsch, and A. H. Bretag. Permeation and block of the skeletal muscle chloride channel, ClC-1, by foreign anions. *J. Gen. Physiol.*, 111:653–665, 1998.

[51] C. Fahlke, C. Dürr, and A. L. George, Jr. Mechanism of ion permeation in skeletal muscle chloride channels. *J. Gen. Physiol.*, 110:551–564, 1997.

[52] C. Fahlke, H. Yu, C. L. Beck, T. R. Rhodes, and A. L. George, Jr. Pore-forming segments in voltage-gated chloride channels. *Nature*, 390:529–532, 1997.

[53] U. Ludewig, T. J. Jentsch, and M. Pusch. Analysis of a protein region involved in permeation and gating of the voltage-gated torpedo chloride channel ClC-0. *J. Physiol.*, 498(3):691–702, 1997.

[54] S. Hebeisen, H. Heidtmann, D. Cosmelli, C. Gonzalez, B. Poser, R. Latorre, O. Alvarez, and C. Fahlke. Anion permeation in human ClC-4 channels. *Biophys. J.*, 84(4):2306–2318, 2003.

[55] W. Nguitragool and C. Miller. Uncoupling of a CLC Cl^-/H^+ exchange transporter by polyatomic anions. *J. Mol. Biol.*, 362:682–690, 2006.

[56] T. Jenntsch, V. Stein, F. Weinreich, and A. Zdebik. Molecular structure and physiological function of chloride channels. *Physiol. Rev.*, 82:503–568, 2002.

[57] A. Picollo and M. Pusch. Chloride/proton antiporter activity of mammalian CLC proteins ClC-4 and ClC-5. *Nature*, 436(7049):420–423, 2005.

[58] A. Accardi and C. Miller. Secondary active transport mediated by a prokaryotic homologue of CLC Cl^- channels. *Nature*, 427:803–807, 2004.

[59] O. Scheel, A. A. Zdebik, S. Lourdel, and T. J. Jentsch. Voltage-dependent electrogenic chloride/proton exchange by endosomal CLC proteins. *Nature*, 436(7049):424–427, 2005.

[60] W. Han, R. C. Cheng, M. C. Maduke, and E. Tajkhorshid. Water access points and hydration pathways in CLC H^+/Cl^- transporters. *Proc. Natl. Acad. Sci. USA*, 111(5):1819–1824, 2014.

[61] R. Dutzler, E. B. Campbell, M. Cadene, B. T. Chait, and R. MacKinnon. X-ray structure of a CLC chloride channel at 3.0 Å reveals the molecular basis of anion selectivity. *Nature*, 415:287–294, 2002.

[62] R. Dutzler, E. B. Campbell, and R. MacKinnon. Gating the selectivity filter in CLC chloride channels. *Science*, 300:108–112, 2003.

[63] A. Accardi, S. Lobet, C. Williams, C. Miller, and R. Dutzler. Synergism between halide binding and proton transport in a CLC-type exchanger. *J. Mol. Biol.*, 362:691–699, 2006.

[64] C. Miller. CLC chloride channels viewed through a transporter lens. *Nature*, 440(7083):484–489, 2006.

[65] C. Miller and W. Nguitragool. A provisional transport mechanism for a chloride channel-type Cl^-/H^+ exchanger. *Proc. R. Soc. Lond. B. (Biol. Sci.)*, 364:175–180, 2009.

[66] J. Lisal and M. Maduke. Proton-coupled gating in chloride channels. *Proc. R. Soc. Lond. B. (Biol. Sci.)*, 364:181–187, 2009.

[67] J. A. Mindell. The Tao of chloride transporter structure. *Science*, 330:601–602, 2010.

[68] A. Accardi and C. Miller. Secondary active transport mediated by a prokaryotic homologue of CLC Cl^- channels. *Nature*, 427:803–807, 2004.

[69] A. Accardi, M. Walden, W. Nguitragool, H. Jayaram, C. Williams, and C. Miller. Separate ion pathways in a Cl^-/H^+ exchanger. *J. Gen. Physiol.*, 126:563–570, 2005.

[70] H.-H. Lim and C. Miller. Intracellular proton-transfer mutants in a CLC Cl^-/H^+ exchanger. *J. Gen. Physiol.*, 133:131–138, 2009.

[71] P. Henderson. Proton-linked sugar transport systems in bacteria. *J. Bioenerg. Biomembr.*, 22:525–569, 1990.

[72] D. R. Bush. Proton-coupled sugar and amino-acid transporters in plants. *Annu. Rev. Plant Physiol. Plant Mol. Biol.*, 44:513–542, 1993.

[73] M. A. Hediger. Structure, function and evolution of solute transporters in prokaryotes and eukaryotes. *J. Exp. Biol.*, 196:15–49, 1994.

[74] D. Wipf, U. Ludewig, M. Tegeder, D. Rentsch, W. Koch, and W. B. Frommer. Conservation of amino acid transporters in fungi, plants and animals. *Trends Biochem. Sci.*, 27:139–147, 2002.

[75] J. K. Pittman, C. Edmond, P. A. Sunderland, and C. M. Bray. A cation-regulated and proton gradient-dependent cation transporter from *Chlamydomonas reinhardtii* has a role in calcium and sodium homeostasis. *J. Biol. Chem.*, 284:525–533, 2009.

[76] D. T. Thwaites and C. M. Anderson. H^+-coupled nutrient, micronutrient and drug transporters in the mammalian small intestine. *Exp. Physiol.*, 92:603–619, 2007.

[77] D. T. Thwaites and C. M. Anderson. The slc36 family of proton-coupled amino acid transporters and their potential role in drug transport. *Br. J. Pharmacol.*, 164:1802–1816, 2011.

[78] D. Marx. Proton transfer 200 years after von Grotthuss: Insights from ab initio simulations. *ChemPhysChem*, 7(9):1848–1870, 2006.

[79] A. Warshel and R. M. Weiss. An empirical valence bond approach for comparing reactions in solution and in enzymes. *J. Am. Chem. Soc.*, 102:6218, 1980.

[80] T. J. F. Day, A. V. Soudackov, M. Cuma, U. W. Schmitt, and G. A. Voth. A second generation multistate empirical valence bond model for proton transport in aqueous systems. *J. Chem. Phys.*, 117(12):5839, 2002.

[81] S. Lammers, S. Lutz, and M. Meuwly. Reactive force fields for proton transfer dynamics. *J. Comp. Chem.*, 29(7):1048–1063, May 2008.

[82] O. S. Smart, J. M. Goodfellow, and B. A. Wallace. The pore dimensions of Gramicidin A. *Biophys. J.*, 65(6):2455–2460, 1993.

[83] F. Garczarek, L. S. Brown, J. K. Lanyi, and K. Gerwert. Proton binding within a membrane protein by a protonated water cluster. *Proc. Natl. Acad. Sci. USA*, 102(10):3633–3638, 2005.

[84] J. Xu and G. A. Voth. Computer simulation of explicit proton translocation in cytochrome c oxidase: The D-pathway. *Proc. Natl. Acad. Sci. USA*, 102(19):6795–6800, 2005.

[85] J. Xu, M. A. Sharpe, L. Qin, S. Ferguson-Miller, and G. A. Voth. Storage of an excess proton in the hydrogen-bonded network of the D-pathway of cytochrome c oxidase: Identification of a protonated water cluster. *J. Am. Chem. Soc.*, 129(10):2910–2913, 2007.

[86] Z. Kuang, U. Mahankali, and T. L. Beck. Proton pathways and H^+/Cl^- stoichiometry in bacterial chloride transporters. *Proteins: Struct., Func., Bioinf.*, 68:26–33, 2007.

[87] D. Wang and G. A. Voth. Proton transport pathway in the CLC Cl^-/H^+ antiporter. *Biophys. J.*, 97:121–131, 2009.

[88] E. Freier, S. Wolf, and K. Gerwert. Proton transfer via a transient linear water-molecule chain in a membrane protein. *Proc. Natl. Acad. Sci. USA*, 108(28):11435–11439, 2011.

[89] P. Goyal, H.-J. Qian, S. Irle, X. Lu, D. Roston, T. Mori, M. Elstner, and Q. Cui. Molecular simulation of water and hydration effects in different environments: challenges and developments for DFTB based models. *J. Phys. Chem. B*, 118:11007–11027, 2013.

[90] M. Gaus, H. Jin, D. Demapan, A. S. Christensen, P. Goyal, M. Elstner, and Q. Cui. DFTB3 parametrization for copper: the importance of orbital angular momentum dependence of hubbard parameters. *J. Chem. Theory Comput.*, 11(9):4205–4219, 2015.

[91] C. A. Wraight. Chance and design – proton transfer in water, channels and bioenergetic proteins. *Biochim. Biophys. Acta – Bioener.*, 1757:886–912, 2006.

[92] L. M. Espinoza-Fonseca and G. L. Ramírez-Salinas. Microsecond molecular simulations reveal a transient proton pathway in the calcium pump. *J. Am. Chem. Soc.*, 137(22):7055–7058, 2015.

[93] Y. J. Ko and W. H. Jo. Secondary water pore formation for proton transport in a CLC exchanger revealed by an atomistic molecular-dynamics simulation. *Biophys. J.*, 98:2163–2169, 2010.

[94] M. H. Cheng and R. D. Coalson. Molecular dynamics investigation of Cl^- and water transport through a eukaryotic ClC transporter. *Biophys. J.*, 102:1363–1371, 2012.

[95] L. Feng, E. B. Campbell, Y. Hsiung, and R. MacKinnon. Structure of a eukaryotic CLC transporter defines an intermediate state in the transport cycle. *Science*, 330(6004):635–641, 2010.

[96] J. Feng, Y. Zhou, S. L. Campbell, T. Le, E. Li, J. D. Sweatt, A. J. Silva, and G. Fan. Dnmt1 and Dnmt3a maintain DNA methylation and regulate synapic function in adult forebrain neurons. *Nat. Neurosci.*, 13:423–430, 2010.

[97] S. B. Hansen, X. Tao, and R. MacKinnon. Structural basis of PIP2 activation of the classical inward rectifier K^+ channel Kir2.2. *Nature*, 477(7365):495–498, 2011.

[98] S. B. Hansen. Lipid agonism: The PIP2 paradigm of ligand-gated ion channels. *BBA-Mol. Cell Biol. L.*, 1851(5):620–628, 2015.

[99] M. R. Whorton and R. MacKinnon. Crystal structure of the mammalian GIRK2 K^+ channel and gating regulation by G proteins, PIP2, and sodium. *Cell*, 147(1):199–208, 2011.

[100] M. A. Zaydman and J. Cui. PIP2 regulation of KCNQ channels: biophysical and molecular mechanisms for lipid modulation of voltage-dependent gating. *Front. Physiol.*, 5:195, 2014.

[101] D. Manna, N. Bhardwaj, M. S. Vora, R. V. Stahelin, H. Lu, and W. Cho. Differential roles of phosphatidylserine, PtdIns(4,5)P_2, and PtdIns(3,4,5)P_3 in plasma membrane targeting of C2 domains. *J. Biol. Chem.*, 283:26047–26058, 2008.

[102] T. Yeung, G. Gilbert, J. Shi, J. Silvius, A. Kapus, and S. Grinstein. Membrane phosphatidylserine regulates surface charge and protein localization. *Science*, 319:210–213, 2008.

[103] P. A. Leventis and S. Grinstein. The distribution and function of phosphatidylserine in cellular membranes. *Annu. Rev. Biophys.*, 39:407–427, 2010.

[104] H. T. McMahon and E. Boucrot. Membrane curvature at a glance. *J. Cell Sci.*, 128:1065–1070, 2015.

[105] N. Fuller and R. P. Rand. The influence of lysolipids on the spontaneous curvature and bending elasticity of phospholipid membranes. *Biophys. J.*, 81:243–254, 2001.

[106] H. T. McMahon and J. L. Gallop. Membrane curvature and mechanisms of dynamic cell membrane remodeling. *Nature*, 438:590–596, 2005.

[107] I. R. Cooke and M. Deserno. Coupling between lipid shape and membrane curvature. *Biophys. J.*, 91:487–495, 2006.

[108] T. Baumgart, B. R. Capraro, C. Zhu, and S. L. Das. Thermodynamics and mechanics of membrane curvature generation and sensing by proteins and lipids. *Annu. Rev. Phys. Chem.*, 62:483–506, January 2011.

[109] R. Panatala, H. Hennrich, and J. C. M. Holthuis. Inner workings and biological impact of phospholipid flippases. *J. Cell Sci.*, 128(11):2021–2032, 2015.

[110] E. J. Tarling, T. Q. de Aguiar Vallim, and P. A. Edwards. Role of abc transporters in lipid transport and human disease. *Trends Endocr. Metab.*, 24(7):342–50, July 2013.

[111] Z. E. Sauna and S. V. Ambudkar. About a switch: how p-glycoprotein (abcb1) harnesses the energy of atp binding and hydrolysis to do mechanical work. *Mol. Cancer Ther.*, 6(1):13–23, 2007.

[112] P. D. W. Eckford and F. J. Sharom. The reconstituted P-glycoprotein multidrug transporter is a flippase for glucosylceramide and other simple glycosphingolipids. *Biochem. J.*, 389(2):517–526, 2005.

[113] H. Nakao, K. Ikeda, M. Iwamoto, H. Shimizu, S. Oiki, Y. Ishihama, and M. Nakano. pH-dependent promotion of phospholipid flip-flop by the KcsA potassium channel. *Biochim. Biophys. Acta Biomembr.*, 1848(1):145–150, 2015.

[114] G. van Meer, D. Halter, H. Sprong, P. Somerharju, and M. R. Egmond. Abc lipid transporters: Extruders, flippases, or flopless activators? *FEBS Lett.*, 580(4):1171 – 1177, 2006.

[115] E. M. Bevers and P. L. Williamson. Phospholipid scramblase: An update. *February*, 584(13):2724 – 2730, 2010.

[116] S. K. Sahu, S. N. Gummadi, N. Manoj, and G. K. Aradhyam. Phospholipid scramblases: An overview. *Arch. Biochem. Biophys.*, 462(1):103 – 114, 2007.

[117] J. Suzuki, T. Fujii, T. Imao, K. Ishihara, H. Kuba, and S. Nagata. Calcium-dependent phospholipid scramblase activity of TMEM16 protein family members. *J. Biol. Chem.*, 288:13305–13316, 2013.

[118] V. A. Fadok, D. R. Voelker, P. A. Campbell, J. J. Cohen, D. L. Bratton, and P. M. Henson. Exposure of phosphatidylserine on the surface of apoptotic lymphocytes triggers specific recognition and removal by macrophages. *J. Immunol.*, 148:2207–2216, 1992.

[119] D. L. Bratton and P. M. Henson. Apoptotic cell recognition: Will the real phosphatidylserine receptor(s) please stand up? *Curr. Biol.*, 18:R76–R79, 2010.

[120] R. H. DeKruyff, X. Bu, A. Ballesteros, C. Santiago, Y.-L. E. Chim, H.-H. Lee, P. Karisola, M. Pichavant, G. G. Kaplan, D. T. Umetsu, G. J. Freeman, and J. M. Casasnovas. T cell/transmembrane, Ig, and mucin-3 allelic variants differentially recognize phosphatidylserine and mediate phagocytosis of apoptotic cells. *J. Immunol.*, 184:1918–1930, 2010.

[121] S. Sanyal and A. K. Menon. Flipping lipids: Why an' what's the reason for? *ACS Chem. Biol.*, 4:895–909, 2009.

[122] J. Suzuki, M. Umeda, P. J. Sims, and S. Nagata. Calcium-dependent phospholipid scrambling by TMEM16F. *Nature*, 468:834–838, 2010.

[123] T. Mohammadi, V. van Dam, R. Sijbrandi, T. Vernet, A. Zapun, A. Bouhss, M. Diepeveen-de Bruin, M. Nguyen-Distéche, B. de Kruijff, and E. Breukink. Identification of ftsw as a transporter of lipid-linked cell wall precursors across the membrane. *EMBO J.*, 30:1425–1432, 2011.

[124] H. Yang, A. Kim, T. David, D. Palmer, T. Jin, J. Tien, F. Huang, T. Cheng, S. R. Coughlin, Y. N. Jan, and L. Y. Jan. TMEM16F forms a Ca^{2+}-activated cation channel required for lipid scrambling in platelets during blood coagulation. *Cell*, 151:111–122, 2012.

[125] N. Pedemonte and L. J. V. Galietta. Structure and function of TMEM16 proteins (anoctamins). *Physiol. Rev.*, 94:419–459, 2014.

[126] Y. D. Yang, H. Cho, J. Y. Koo, M. H. Tak, Y. Cho, W.-S. Shim, S. P. Park, J. Lee, B. Lee, B.-M. Kim, R. Raouf, Y. K. Shin, and U. Oh. TMEM16A confers receptor-activated calcium-dependent chloride conductance. *Nature*, 455:1210–1215, 2008.

[127] B. C. Schroeder, T. Cheng, Y. N. Jan, and L. Y. Jan. Expression cloning of TMEM16A as a calcium-activated chloride channel subunit. *Cell*, 134:1019–1029, 2008.

[128] S. Pifferi, V. Cenedese, and A. Menini. Anoctamin 2/TMEM16B: a calcium-activated chloride channel in olfactory transduction. *Exp. Physiol.*, 97:193–199, 2012.

[129] H. C. Hartzell, I. Putzier, and J. Arreola. Calcium-activated chloride channels. *Annu. Rev. Physiol.*, 67:719–758, 2005.

[130] H. C. Hartzell, K. Yu, Q. Xiao, L.-T. Chien, and Z. Qu. Anoctamin/TMEM16 family members are Ca^{2+}-activated Cl^{-} channels. *J. Physiol.*, 587:2127–2139, 2009.

[131] G. Fallah, T. Römer, S. Detro-Dassen, U. Braam, F. Markwardt, and G. Schmalzing. TMEM16A(a)/anoctamin-1 shares a homodimeric architecture with CLC chloride channels. *Mol. Cell Proteomics*, 10(2), 2011.

[132] J. T. Sheridan, E. N. Worthington, K. Yu, S. E. Gabriel, H. C. Hartzell, and R. Tarran. Characterization of the oligomeric structure of the ca^{2+}-activated cl^{-} channel ano1/TMEM16A. *J. Biol. Chem.*, 286(2):1381–1388, 2011.

[133] J. Tien, H. Y. Lee, D. L. Minor, Y. N. Jan, and L. Y. Jan. Identification of a dimerization domain in the TMEM16A calcium-activated chloride channel (cacc). *Proc. Natl. Acad. Sci. USA*, 110(16):6352–6357, 2013.

[134] J. D. Brunner, N. K. Lim, S. Schenck, A. Duerst, and R. Dutzler. X-ray structure of a calcium-activated TMEM16 lipid scramblase. *Nature*, 516:207–212, 2014.

[135] B.-C. Lee, A. K. Menon, and A. Accardi. The nhtmem16 scramblase is also a nonselective ion channel. *Biophys. J.*, 111(9):1919–1924, 2016.

[136] S. Hug. Classical molecular dynamics in a nutshell. In L. Monticelli and E. Salonen, editors, *Biomolecular Simulations: Methods and Protocols*, pages 127–152. Humana Press, Totowa, NJ, 2013.

[137] J. R. Perilla, B. C. Goh, C. K. Cassidy, B. Liu, R. C. Bernardi, T. Rudack, H. Yu, Z. Wu, and K. Schulten. Molecular dynamics simulations of large macromolecular complexes. *Curr. Opin. Struct. Biol.*, 31:64–74, 2015.

[138] T. R. M. Barends, L. Foucar, S. Botha, R. B. Doak, R. L. Shoeman, K. Nass, J. E. Koglin, G. J. Williams, S. Boutet, M. Messerschmidt, and I. Schlichting. De novo protein crystal structure determination from X-ray free-electron laser data. *Nature*, 505(7482):244–247, 2014.

[139] R. Y.-R. Wang, M. Kudryashev, X. Li, E. H. Egelman, M. Basler, Y. Cheng, D. Baker, and F. DiMaio. De novo protein structure determination from near-atomic-resolution cryo-em maps. *Nat. Methods*, 12(4):335–338, 2015.

[140] R. N. Jackson, A. J. McCoy, T. C. Terwilliger, R. J. Read, and B. Wiedenheft. X-ray structure determination using low-resolution electron microscopy maps for molecular replacement. *Nat. Protocols*, 10(9):1275–1284, jul 2015.

[141] R. O. Dror, R. M. Dirks, J. Grossman, H. Xu, and D. E. Shaw. Biomolecular simulation: A computational microscope for molecular biology. *Annu. Rev. Biophys.*, 41(1):429–452, jun 2012.

[142] E. H. Lee, J. Hsin, M. Sotomayor, G. Comellas, and K. Schulten. Discovery through the computational microscope. *Structure*, 17:1295–1306, 2009.

[143] K. Oxenoid and J. J. Chou. The present and future of solution NMR in investigating the structure and dynamics of channels and transporters. *Curr. Opin. Struct. Biol.*, 23(4):547–554, aug 2013.

[144] D. T. Murray, N. Das, and T. A. Cross. Solid state NMR strategy for characterizing native membrane protein structures. *Acc. Chem. Res.*, 46(9):2172–2181, sep 2013.

[145] H. S. McHaourab, P. R. Steed, and K. Kazmier. Toward the fourth dimension of membrane protein structure: Insight into dynamics from spin-labeling EPR spectroscopy. *Structure*, 19(11):1549–1561, 2011.

[146] H. Vitrac, D. M. MacLean, V. Jayaraman, M. Bogdanov, and W. Dowhan. Dynamic membrane protein topological switching upon changes in phospholipid environment. *Proc. Natl. Acad. Sci. USA*, 112(45):13874–13879, nov 2015.

[147] M. Karplus and J. A. McCammon. Molecular dynamics simulations of biomolecules. *Nat. Struct. Biol.*, 265:654–652, 2002.

[148] E. Papaleo. Integrating atomistic molecular dynamics simulations, experiments, and network analysis to study protein dynamics: strength in unity. *Front. Mol. Biosci.*, 2, may 2015.

[149] M. P. Allen and D. J. Tildesley. *Computer Simulation of Liquids*. Oxford University Press, New York, 1987.

[150] D. Frenkel and B. Smit. *Understanding Molecular Simulation From Algorithms to Applications*. Academic Press, California, 2002.

[151] D. E. Shaw, R. O. Dror, J. K. Salmon, J. P. Grossman, K. M. Mackenzie, J. A. Bank, C. Young, M. M. Deneroff, B. Batson, K. J. Bowers, E. Chow, M. P. Eastwood, D. J. Ierardi, J. L. Klepeis, J. S. Kuskin, R. H. Larson, K. Lindorff-Larsen, P. Maragakis, M. A. Moraes, S. Piana, Y. Shan, and B. Towles. Millisecond-scale molecular dynamics simulations on anton. In *Proceedings of the Conference on High Performance Computing Networking, Storage and Analysis*, SC '09, pages 39:1–39:11, New York, NY, USA, 2009. ACM.

[152] E. Lindahl and M. S. P. Sansom. Membrane proteins: molecular dynamics simulations. *Curr. Opin. Struct. Biol.*, 18:425–431, 2008.

[153] J. L. Klepeis, K. Lindorff-Larsen, R. O. Dror, and D. E. Shaw. Long-timescale molecular dynamics simulations of protein structure and function. *Curr. Opin. Struct. Biol.*, 19:120–127, 2009.

[154] G. R. Bowman, V. A. Voelz, and V. S. Pande. Atomistic folding simulations of the five-helix bundle protein λ_{6-85}. *J. Am. Chem. Soc.*, 133:664–667, 2011.

[155] K. Lindorff-Larsen, S. Piana, R. O. Dror, and D. E. Shaw. How fast-folding proteins fold. *Science*, 334:517–520, 2011.

[156] M. Ø. Jensen, V. Jogini, D. W. Borhani, A. E. Leffler, R. O. Dror, and D. E. Shaw. Mechanism of voltage gating in potassium channels. *Science*, 336:229–233, 2012.

[157] F. C. Bernstein, T. F. Koetzle, G. J. Williams, E. F. Meyer, M. D. Brice, J. R. Rogers, O. Kennard, T. Shimanouchi, and M. Tasumi. The Protein Data Bank: A computer-based archival file for macromolecular structures. *J. Mol. Biol.*, 112(3):535–542, 1977.

[158] H. M. Berman, J. Westbrook, Z. Feng, G. Gilliland, T. N. Bhat, H. Weissig, I. N. Shindyalov, and P. E. Bourne. The protein data bank. *Nucleic Acids Res.*, 28:235–242, 2000.

[159] H. Berman, K. Henrick, and H. Nakamura. Announcing the worldwide Protein Data Bank. *Nat. Struct. Biol.*, 10(12):980, 2003.

[160] P. W. Hildebrand, A. Goede, R. A. Bauer, B. Gruening, J. Ismer, E. Michalsky, and R. Preissner. SuperLooper–a prediction server for the modeling of loops in globular and membrane proteins. *Nucleic Acids Res.*, 37(Web Server):W571–W574, jul 2009.

[161] W. Humphrey, A. Dalke, and K. Schulten. VMD – Visual Molecular Dynamics. *J. Mol. Graphics*, 14(1):33–38, 1996.

[162] C. R. Søndergaard, M. H. Olsson, M. Rostkowski, and J. H. Jensen. Improved treatment of ligands and coupling effects in empirical calculation and rationalization of pKa values. *J. Chem. Theory Comput.*, 7(7):2284–2295, 2011.

[163] M. H. Olsson, C. R. Søndergaard, M. Rostkowski, and J. H. Jensen. Propka3: consistent treatment of internal and surface residues in empirical pKa predictions. *J. Chem. Theory Comput.*, 7:525–537, 2011.

[164] T. J. Dolinsky, P. Czodrowski, H. Li, J. E. Nielsen, J. H. Jensen, G. Klebe, and N. A. Baker. PDB2PQR: expanding and upgrading automated preparation of biomolecular structures for molecular simulations. *Nucleic Acids Res.*, 35(Web Server):W522–W525, May 2007.

[165] G. van Meer, D. R. Voelker, and G. W. Feigenson. Membrane lipids: where they are and how they behave. *Nat. Rev. Mol. Cell Biol.*, 9(2):112–124, 2008.

[166] W. Dowhan. Molecular basis for membrane phospholipid diversity:why are there so many lipids? *Annu. Rev. Biochem.*, 66(1):199–232, jun 1997.

[167] G. Paradies, V. Paradies, V. D. Benedictis, F. M. Ruggiero, and G. Petrosillo. Functional role of cardiolipin in mitochondrial bioenergetics. *Biochim. Biophys. Acta – Bioener.*, 1837:408–417, 2014.

[168] E. Wu, X. Cheng, S. Jo, H. Rui, K. Song, E. Dávila-Contreras, Y. Qi, J. Lee, V. Monje-Galvan, R. Venable, J. Klauda, and W. Im. CHARMM-GUI Membrane Builder toward realistic biological membrane simulations. *J. Comp. Chem.*, 35(27):1997–2004, 2014.

[169] Y. Qi, X. Cheng, J. Lee, J. V. Vermaas, T. V. Pogorelov, E. Tajkhorshid, S. Park, J. B. Klauda, and W. Im. CHARMM-GUI HMMM builder for membrane simulations with the highly mobile membrane-mimetic model. *Biophys. J.*, 109:2012–2022, 2015.

[170] M. A. Lomize, A. L. Lomize, L. D. Pogozheva, and H. I. Mosberg. Opm: Orientations of proteins in membranes database. *Bioinformatics*, 22:623–625, 2006.

[171] A. L. Lomize, I. D. Pogozheva, M. A. Lomize, and H. I. Mosberg. Positioning of proteins in membranes: A computational approach. *Prot. Sci.*, 15:1318–1333, 2006.

[172] A. L. Lomize, I. D. Pogozheva, M. A. Lomize, and H. I. Mosberg. The role of hydrophobic interactions in positioning of peripheral proteins in membranes. *BMC Structural Biology*, 7:44, 2007.

[173] A. L. Lomize, I. D. Pogozheva, and H. I. Mosberg. Anisotropic solvent model of the lipid bilayer. 2. energetics of insertion of small molecules, peptides, and proteins in membranes. *J. Chem. Inf. Model.*, 51:930–946, 2011. http://opm.phar.umich.edu/.

[174] S. Jo, T. Kim, and W. Im. Automated builder and database of protein/membrane complexes for molecular dynamics simulations. *PLoS One*, 2:e880, 2007.

[175] S. Jo, T. Kim, V. G. Iyer, and W. Im. CHARMM-GUI: A web-based graphical user interface for CHARMM. *J. Comp. Chem.*, 29:1859–1865, 2008.

[176] W. L. Jorgensen, J. Chandrasekhar, J. D. Madura, R. W. Impey, and M. L. Klein. Comparison of simple potential functions for simulating liquid water. *J. Chem. Phys.*, 79(2):926–935, 1983.

[177] A. D. MacKerell, Jr., M. Feig, and C. L. Brooks, III. Extending the treatment of backbone energetics in protein force fields: Limitations of gas-phase quantum mechanics in reproducing protein conformational distributions in molecular dynamics simulations. *J. Comp. Chem.*, 25(11):1400–1415, 2004.

[178] C. G. Mayne, J. Saam, K. Schulten, E. Tajkhorshid, and J. C. Gumbart. Rapid parameterization of small molecules using the force field toolkit. *J. Comp. Chem.*, online, 2013.

[179] J. C. Phillips, R. Braun, W. Wang, J. Gumbart, E. Tajkhorshid, E. Villa, C. Chipot, R. D. Skeel, L. Kale, and K. Schulten. Scalable molecular dynamics with NAMD. *J. Comp. Chem.*, 26:1781–1802, 2005.

[180] A. D. MacKerell, Jr., D. Bashford, M. Bellott, R. L. Dunbrack, Jr., J. D. Evanseck, M. J. Field, S. Fischer, J. Gao, H. Guo, S. Ha, D. Joseph, L. Kuchnir, K. Kuczera, F. T. K. Lau, C. Mattos, S. Michnick, T. Ngo, D. T. Nguyen, B. Prodhom, I. W. E. Reiher, B. Roux, M. Schlenkrich, J. Smith, R. Stote, J. Straub, M. Watanabe, J. Wiorkiewicz-Kuczera, D. Yin, and M. Karplus. All-atom empirical potential for molecular modeling and dynamics studies of proteins. *J. Phys. Chem. B*, 102:3586–3616, 1998.

[181] R. B. Best, X. Zhu, J. Shim, P. E. M. Lopes, J. Mittal, M. Feig, and A. D. MacKerell. Optimization of the additive charmm all-atom protein force field targeting improved sampling of the backbone ϕ, ψ and side-chain χ_1 and χ_2 dihedral angles. *J. Chem. Theory Comput.*, 8(9):3257–3273, 2012.

[182] T. Darden, D. York, and L. Pedersen. Particle mesh Ewald: An $N{\cdot}\log(N)$ method for Ewald sums in large systems. *J. Chem. Phys.*, 98:10089–10092, 1993.

[183] G. J. Martyna, D. J. Tobias, and M. L. Klein. Constant pressure molecular dynamics algorithms. *J. Chem. Phys.*, 101(5):4177–4189, 1994.

[184] S. Nosé. A unified formulation of the constant temperature molecular dynamics methods. *J. Chem. Phys.*, 81(1):511–519, 1984.

[185] W. G. Hoover. Canonical dynamics: Equilibrium phase-space distributions. *Phys. Rev. A*, 31:1695–1697, 1985.

[186] S. E. Feller, Y. Zhang, R. W. Pastor, and B. R. Brooks. Constant pressure molecular dynamics simulation: The Langevin piston method. *J. Chem. Phys.*, 103(11):4613–4621, 1995.

[187] B. Roux. The calculation of the potential of mean force using computer simulations. *Comput. Phys. Commun.*, 91:275–282, 1995.

[188] A. Barducci, G. Bussi, and M. Parrinello. Well-tempered metadynamics: A smoothly converging and tunable free-energy method. *Phys. Rev. Lett.*, 100:020603, 2008.

[189] B. Isralewitz, M. Gao, and K. Schulten. Steered molecular dynamics and mechanical functions of proteins. *Curr. Opin. Struct. Biol.*, 11:224–230, 2001.

[190] J. Schlitter, M. Engels, P. Krüger, E. Jacoby, and A. Wollmer. Targeted molecular dynamics simulation of conformational change — application to the T $\leftrightarrow$ R transition in insulin. *Mol. Sim.*, 10(2–6):291–308, 1993.

[191] J. Hénin and C. Chipot. Overcoming free energy barriers using unconstrained molecular dynamics simulations. *J. Chem. Phys.*, 121(7):2904–2914, 2004.

[192] Y. Wang, C. B. Harrison, K. Schulten, and J. A. McCammon. Implementation of accelerated molecular dynamics in NAMD. *Comput. Sci. Discov.*, 4:015002, 2011. (11 pages).

[193] M. Moradi and E. Tajkhorshid. Mechanistic picture for conformational transition of a membrane transporter at atomic resolution. *Proc. Natl. Acad. Sci. USA*, 110(47):18916–18921, 2013.

[194] M. Moradi and E. Tajkhorshid. Driven metadynamics: Reconstructing equilibrium free energies from driven adaptive-bias simulations. *J. Phys. Chem. Lett.*, 4(11):1882–1887, 2013.

[195] S. De Stefano, M. Pusch, and G. Zifarelli. Extracellular determinants of anion discrimination of the Cl^-/H^+ antiporter protein CLC-5. *J. Biol. Chem.*, 286(51):44134–44144, 2011.

[196] A. A. Zdebik, G. Zifarelli, E.-Y. Bergsdorf, P. Soliani, O. Scheel, T. J. Jentsch, and M. Pusch. Determinants of anion-proton coupling in mammalian endosomal CLC proteins. *J. Biol. Chem.*, 283(7):4219–4227, 2008.

[197] A. K. Alekov and C. Fahlke. Channel-like slippage modes in the human anion/proton exchanger ClC-4. *J. Gen. Physiol.*, 133(5):485–496, 2009.

[198] H. Jayaram, J. L. Robertson, F. Wu, C. Williams, and C. Miller. Structure of a slow CLC Cl^-/H^+ antiporter from a cyanobacterium. *Biochemistry*, 50(5):788–794, 2011.

[199] L. Leisle, C. F. Ludwig, F. A. Wagner, T. J. Jentsch, and T. Stauber. ClC-7 is a slowly voltage-gated $2Cl^-/1H^+$-exchanger and requires ostm1 for transport activity. *EMBO J.*, 30(11):2140–2152, 2011.

[200] G. Orhan, C. Fahlke, and A. K. Alekov. Anion- and proton-dependent gating of ClC-4 anion/proton transporter under uncoupling condition. *Biophys. J.*, 100(5):1233–1241, 2011.

[201] M. Maduke, D. J. Pheasant, and C. Miller. High-level expression, functional reconstitution, and quaternary structure of a prokaryotic ClC-type chloride channel. *J. Gen. Physiol.*, 114(5):713–722, 1999.

[202] C. Fahlke. Ion permeation and selectivity in ClC-type chloride channels. *Am. J. Physiol. – Ren. Physiol.*, 280:F748–F757, 2001.

[203] H.-H. Lim, R. B. Stockbridge, and C. Miller. Fluoride-dependent interruption of the transport cycle of a CLC Cl^-/H^+ antiporter. *Nature Chem Biol*, 9(11):721–725, 2013.

[204] A. E. Brammer, R. B. Stockbridge, and C. Miller. F^-/H^+ selectivity in CLC^F-type F^-/H^+ antiporters. *J. Gen. Physiol.*, 144(2):129–136, 2014.

[205] J. L. Baker, N. Sudarsan, Z. Weinberg, A. Roth, R. B. Stockbridge, and R. R. Breaker. Widespread genetic switches and toxicity resistance proteins for fluoride. *Science*, 335(6065):233–235, 2012.

[206] R. B. Stockbridge, H.-H. Lim, R. Otten, C. Williams, T. Shane, Z. Weinberg, and C. Miller. Fluoride resistance and transport by riboswitch-controlled CLC antiporters. *Proc. Natl. Acad. Sci. USA*, 109(38):15289–15294, 2012.

[207] M. Walden, A. Accardi, F. Wu, C. Xu, C. Williams, and C. Miller. Uncoupling and turnover in a Cl^-/H^+ exchange transporter. *J. Gen. Physiol.*, 129:317–329, 2007.

[208] A. Picollo, M. Malvezzi, J. Houtman, and A. Accardi. Basis of substrate binding and conservation of selectivity in the CLC famility of channels and transporters. *Nat. Struct. Mol. Biol.*, 16:1294–1301, 2009.

[209] A. Picollo, Y. Xu, N. Johner, S. Berneche, and A. Accardi. Synergistic substrate binding determines the stoichiometry of transport of a prokaryotic H^+/Cl^- exchanger. *Nat. Struct. Mol. Biol.*, 19:525–531, 2012.

[210] L. Zhang and J. Hermans. Hydrophobicity of cavities in proteins. *Proteins: Struct., Func., Gen.*, 24:433–438, 1996.

[211] J. Cohen and K. Schulten. Mechanism of anionic conduction across CLC. *Biophys. J.*, 86:836–845, 2004.

[212] D. L. Bostick and M. L. Berkowitz. Exterior site occupancy infers chloride-induced proton gating in a prokaryotic homolog of the CLC chloride channel. *Biophys. J.*, 87:1686–1696, 2004.

[213] J. D. Faraldo-Gómez and B. Roux. Electrostatics of ion stabilization in a CLC chloride channel homologue from *Escherichia coli*. *J. Mol. Biol.*, 339:981–1000, 2004.

[214] W. Jorgensen, J. Chandrasekhar, J. D. Maudura, R. W. Impey, and M. L. Klein. Comparison of simple potential functions for simulating liquid water. *J. Chem. Phys.*, 79:926–935, 1983.

[215] O. S. Smart, J. G. Neduvelil, X. Wang, B. A. Wallace, and M. S. P. Sansom. HOLE: A program for the analysis of the pore dimensions of ion channel structural models. *J. Mol. Graphics*, 14:354–360, 1996.

[216] J. L. Robertson, L. Kolmakova-Partensky, and C. Miller. Design, function and structure of a monomeric CLC transporter. *Nature*, 468:844–846, 2010.

[217] Y. Iwadate, K. Kawamura, K. Igarashi, and J. Mochinaga. Effective ionic radii of nitrite and thiocyanate estimated in terms of the boettcher equation and the lorentz-lorenz equation. *J. Phys. Chem.*, 86(26):5205–5208, 1982.

[218] Y. J. Ko and W. H. Jo. Chloride ion conduction without water coordination in the pore of ClC protein. *J. Comp. Chem.*, 31(3):603–611, 2010.

[219] F. L. Gervasio, M. Parrinello, M. Ceccarelli, and M. Klein. Exploring the gating mechanism in the ClC chloride channel via metadynamics. *J. Mol. Biol.*, 361:390–398, 2006.

[220] B. Tansel, J. Sager, T. Rector, J. Garland, R. F. Strayer, L. Levine, M. Roberts, M. Hummerick, and J. Bauer. Significance of hydrated radius and hydration shells on ionic permeability during nanofiltration in dead end and cross flow modes. *Separation and Purification Technolog*, 51(1):40–47, 2006.

[221] L. A. Richards, A. I. Schäfer, B. S. Richards, and B. Corry. The importance of dehydration in determining ion transport in narrow pores. *Small*, 8(11):1701–1709, 2012.

[222] A. De Angeli, D. Monachello, G. Ephritikhine, J. M. Frachisse, S. Thomine, F. Gambale, and H. Barbier-Brygoo. The nitrate/proton antiporter atclca mediates nitrate accumulation in plant vacuoles. *Nature*, 442(7105):939–942, 2006.

[223] G. Zifarelli and M. Pusch. Conversion of the 2 $Cl^-/1$ H^+ antiporter ClC-5 in a NO_3^-/H^+ antiporter by a single point mutation. *EMBO J.*, 28(3):175–182, 2009.

[224] E.-Y. Bergsdorf, A. A. Zdebik, and T. J. Jentsch. Residues important for nitrate/proton coupling in plant and mammalian CLC transporters. *J. Biol. Chem.*, 284(17):11184–11193, 2009.

[225] C. M. Khantwal, S. J. Abraham, W. Han, T. Jiang, T. S. Chavan, R. C. Cheng, S. M. Elvington, C. W. Liu, I. I. Mathews, R. A. Stein, H. S. Mchaourab, E. Tajkhorshid, and M. Maduke. Revealing an outward-facing open conformational state in a CLC Cl/H exchange transporter. *eLife*, page e11189, 2016.

[226] C. J. Law, J. Almqvist, A. Bernstein, R. M. Goetz, Y. Huang, C. Soudant, A. Laaksonen, S. Hovmöller, and D.-N. Wang. Salt-bridge dynamics control substrate-induced conformational change in the membrane transporter GlpT. *J. Mol. Biol.*, 378:828–839, 2008.

[227] Y. Yin, M. Ø. Jensen, E. Tajkhorshid, and K. Schulten. Sugar binding and protein conformational changes in lactose permease. *Biophys. J.*, 91:3972–3985, 2006.

[228] M. Ø. Jensen, Y. Yin, E. Tajkhorshid, and K. Schulten. Sugar transport across lactose permease probed by steered molecular dynamics. *Biophys. J.*, 93:92–102, 2007.

[229] M. Maduke, D. J. Pheasant, and C. Miller. High-level expression, functional reconstitution, and quaternary structure of a prokaryotic ClC-type chloride channel. *J. Gen. Physiol.*, 114:713–722, 1999.

[230] A. Accardi, L. Kolmakova-Partensky, C. Williams, and C. Miller. Ionic currents mediated by a prokaryotic homologue of CLC Cl- channels. *J. Gen. Physiol.*, 123(2):109–119, 2004.

[231] S. Wege, M. Jossier, S. Filleur, S. Thomine, H. Barbier-Brygoo, F. Gambale, and A. De Angeli. The proline 160 in the selectivity filter of the arabidopsis no3-/h+ exchanger atclca is essential for nitrate accumulation in planta. *The Plant Journal*, 63(5):861–869, 2010.

[232] A. D. MacKerell, Jr., D. Bashford, M. Bellott, J. R. L. Dunbrack, J. Evanseck, M. J. Field, S. Fischer, J. Gao, H. Guo, S. Ha, D. Joseph, L. Kuchnir, K. Kuczera, F. T. K. Lau, C. Mattos, S. Michnick, T. Ngo, D. T. Nguyen, B. Prodhom, B. Roux, M. Schlenkrich, J. Smith, R. Stote, J. Straub, M. Watanabe, J. Wiorkiewicz-Kuczera, D. Yin, and M. Karplus. Self-consistent parameterization of biomolecules for molecular modeling and condensed phase simulations. *FASEB J.*, 6(1):A143–A143, 1992.

[233] R. Dutzler, E. B. Campbell, M. Cadene, B. T. Chait, and R. MacKinnon. X-ray structure of a CLC chloride channel at 3.0 Å reveals the molecular basis of anion selectivity. *Nature*, 415:287–294, 2002.

[234] R. Dutzler, E. B. Campbell, and R. MacKinnon. Gating the selectivity filter in CLC chloride channels. *Science*, 300:108–112, 2003.

[235] S. Scheuring, D. Lévy, and J.-L. Rigaud. Watching the components of photosynthetic bacterial membranes and their *in situ* organisation by atomic force microscopy. *Biochim. Biophys. Acta*, 1712:109–127, 2005.

[236] Y. Shi. Common folds and transport mechanisms of secondary active transporters. *Annu. Rev. Biophys.*, 42:51–72, 2013.

[237] L. Feng, E. B. Campbell, and R. MacKinnon. Molecular Mechanism of Proton Transport in CLC Cl^-/H^+ Exchanger Transporters. *Proc. Natl. Acad. Sci. USA*, 109:11699–11704, 2012.

[238] G. V. Miloshevsky, A. Hassanein, and P. C. Jordan. Antiport mechanism for Cl^-/H^+ in ClC-ec1 from normal-mode analysis. *Biophys. J.*, 98:999–1008, 2010.

[239] T. Krivobokva, R. Briones, J. S. Hub, A. Munk, and B. L. de Groot. Partial least-square functional mode analysis: application to the membrane proteins AQP1, Aqy1, and CLC-ec1. *Biophys. J.*, 103:786–796, 2012.

[240] H. Jayaram, A. Accardi, F. Wu, C. Williams, and C. Miller. Ion permeation through a Cl-selective channel designed from a CLC Cl^-/H^+ exchanger. *Proc. Natl. Acad. Sci. USA*, 105:11194–11199, 2008.

[241] S. M. Elvington, C. W. Liu, and M. C. Maduke. Substrate-driven conformational changes in ClC-ec1 observed by fluorine NMR. *EMBO J.*, 28:3090–3102, 2009.

[242] B. Isin, K. Schulten, E. Tajkhorshid, and I. Bahar. Mechanism of signal propagation upon retinal isomerization: Insights from molecular dynamics simulations of rhodopsin restrained by normal modes. *Biophys. J.*, 95:789–803, 2008.

[243] D. C. Rapaport. Self-assembly of polyhedral shells: A molecular dynamics study. *Phys. Rev. E*, 70:051905–1–051905–13, 2004.

[244] H. B. Mann and D. R. Whitney. On a test of whether one of two random variables is stochastically larger than the other. *The Annals of Mathematical Statistics*, 18(1):50–60, 1947.

[245] Y. Wang, Y. Huang, J. Wang, C. Cheng, W. Huang, P. Lu, Y.-N. Xu, P. Wang, N. Yan, and Y. Shi. Structure of the formate transporter FocA reveals a pentameric aquaporin-like channel. *Nature*, 462:467–472, 2009.

[246] Y. Chen, E. R. Cruz-Chu, J. Woodard, M. R. Gartia, K. Schulten, and L. Liu. Electrically induced conformational change of peptides on metallic nano-surfaces. *ACS Nano*, 6:8847–8856, 2012.

[247] H.-H. Lim, T. Shane, and C. Miller. Intracellular proton access in a Cl^-/H^+ antiporter. *PLoS Biol.*, 10(12):e1001441, 2012.

[248] I. Bahar, T. R. Lezon, L. W. Yang, and E. Eyal. Global Dynamics of Proteins: Bridging Between Structure and Function. *Annual Review of Biophysics*, 39(1):23–42, June 2010.

[249] M. Gur, E. Zomot, and I. Bahar. Global motions exhibited by proteins in micro- to milliseconds simulations concur with anisotropic network model predictions. *J. Chem. Phys.*, 139(12):121912, 2013.

[250] A. Accardi and A. Picollo. CLC channels and transporters: proteins with borderline personalities. *Biochim. Biophys. Acta*, 1798:1457–1464, 2010.

[251] D. Basilio, K. Noack, A. Picollo, and A. Accardi. Conformational changes required for Cl^-/H^+ exchange mediated by a CLC transporter. *Nat. Struct. Mol. Biol.*, 21(5):456–463, 2014.

[252] E. M. Bevers and P. L. Williamson. Getting to the outer leaflet: Physiology of phosphatidylserine exposure at the plasma membrane. *Physiol. Rev.*, 96(2):605–645, 2016.

[253] J. D. Brunner, S. Schenck, and R. Dutzler. Structural basis for phospholipid scrambling in the TMEM16 family. *Curr. Opin. Struct. Biol.*, 39:61–70, 2016.

[254] M. Rostkowski, M. Olsson, C. Sondergaard, and J. Jensen. Graphical analysis of ph-dependent properties of proteins predicted using propka. *BMC Structural Biology*, 11(1):6, 2011.

[255] K. Yu, J. M. Whitlock, K. Lee, E. A. Ortlund, Y. Yuan Cui, and H. C. Hartzell. Identification of a lipid scrambling domain in ano6/tmem16f. *eLife*, 4:e06901, 2015.

[256] M. A. Kol, A. N. C. van Laak, D. T. S. Rijkers, J. A. Killian, A. I. P. M. de Kroon, and B. de Kruijff. Phospholipid flop induced by transmembrane peptides in model membranes is modulated by lipid composition. *Biochemistry*, 42(1):231–237, 2003.

[257] M. A. Kol, A. I. P. M. de Kroon, J. A. Killian, and B. de Kruijff. Transbilayer movement of phospholipids in biogenic membranes. *Biochemistry*, 43(10):2673–2681, 2004.

[258] T. Pomorski and A. K. Menon. Lipid flippases and their biological functions. *Cell. Mol. Life Sci.*, 63(24):2908–2921, 2006.

[259] K. E. Langley and E. P. Kennedy. Energetics of rapid transmembrane movement and of compositional asymmetry of phosphatidylethanolamine in membranes of bacillus megaterium. *Proc. Natl. Acad. Sci. USA*, 76(12):6245–6249, 1979.